# Double Volumetric Navigators for Real-time Simultaneous Shim and Motion Measurement and Correction in Glycogen Chemical Exchange Saturation Transfer (GlycoCEST) MRI


By

**Gizeaddis Lamesgin Simegn**

Thesis presented for the degree of

**Doctor of Philosophy**

In Biomedical Engineering

Medical Imaging Research Unit

Division of Biomedical Engineering

Department of Human Biology

**University of Cape Town**

March 2019

# Declaration

I, **Gizeaddis Lamesgin Simegn**, hereby declare that the work on which this dissertation is based is my original work, both in concept and excution (except where acknowledgements indicate otherwise) and that neither the whole work nor any part of it has been, is being, or is to be submitted for another degree in this or any other university.

I empower the university to reproduce for the purpose of research either the whole or any portion of the contents in any manner whatsoever.

Gizeaddis L. Simegn

Signed by candidate

Cape Town

March 2019

I confirm that I have been granted permission by the University of Cape Town's Doctoral Degrees Board to include the following publication(s) in my PhD thesis, and where co-authorships are involved, my co-authors have agreed that I may include the publication(s):

- **Gizeaddis L. Simegn**, Andre J.W. van der Kouwe, Frances C. Robertson, Ernesta M. Meintjes, and Ali Alhamud. Real-time simultaneous shim and motion measurement and correction in glycoCEST MRI using Double Volumetric Navigators (DvNavs). Magnetic Resonance in Medicine, 2018; 00:1-14. https://doi.org/10.1002/mrm.27597.

Signature Signed by candidate

Date: **March 2019**

Student Name: **Gizeaddis Lamesgin Simegn**

Student Number: **SMGGIZ001**

Dedicated to

*My beloved wife 'ma' (ማማም) and precious son 'Amen' (አሜን ጉልቁ)*

# Acknowledgements

Working with many people during this PhD study has been truly a life-changing experience for me and it would not have been possible to do without the guidance and support of several people. First, I would like to express my sincere gratitude to my supervisor Dr. Frances Robertson for her valuable guidance, research inputs and consistent support I received throughout the research work. Her ability to look in detail critically taught me a lot. Many thanks to Dr. Ali Alhamud who first accepted me as his PhD student, who made it possible for me to study CEST MRI and provided me funding for my study travel to Boston. Without his continuous support and constant feedback this PhD would not have been achievable. I am also grateful to my co-supervisor Assoc Prof. Andre van der Kouwe for all the support and guidance he gave me, during the few months I spent undertaking my research in Athinoula A. Marthinos Center for Biomedical Imaging and for his continuous support throughout my study. Many thanks to Prof. Ernesta Meintjes, SARChI Chair in Brain Imaging and Director of CUBIC-UCT, for her continuous guidance, support and for letting me work in the lab. I would also like to thank Prof. Thomas Franz, Head of Division of Biomedical Engineering, for all his support during my stay at UCT.

I would like to acknowledge the funding received for my study from Netherlands Initiative for Capacity development in Higher Education-NICHE/ETH/247 project through CINOP global. I am especially grateful to Mr. Rene Lenssen, who is the most positive and kind person I have ever known, who has been very responsive for all my financial inquires. Special thanks to Jimma institute of Technology, School of Biomedical Engineering collogues and to Prof. Esayas Alemayehu for the support I received.

I am grateful to my wife Mulu, who has been by my side all the time, living every single minute of it, took the courage to raise our son alone, for always believing in me and pushing me to follow my dreams. I would not have had the courage to embark on this journey in the first place. I am also grateful to my mom, brothers Aragaw and Zewudu and my sisters who have been inspirational, and friends (Worksha, Wond, Baye in mind) who have supported me along the way.

And finally, to everyone in the Medical Imaging Research unit (MRI lab) and CUBIC-UCT staff. It was great sharing ideas with all of you during last few years.

# Abstract

Glycogen is the primary glucose storage mechanism in in living systems and plays a central role in systemic glucose homeostasis. The study of muscle glycogen concentrations *in vivo* still largely relies on tissue sampling methods via needle biopsy. However, muscle biopsies are invasive and limit the frequency of measurements and the number of sites that can be assessed. Non-invasive methods for quantifying glycogen *in vivo* are therefore desirable in order to understand the pathophysiology of common diseases with dysregulated glycogen metabolism such as obesity, insulin resistance, and diabetes, as well as glycogen metabolism in sports physiology.

Chemical Exchange Saturation Transfer (CEST) MRI has emerged as a non-invasive contrast enhancement technique that enables detection of molecules, like glycogen, whose concentrations are too low to impact the contrast of standard MR imaging. CEST imaging is performed by selectively saturating hydrogen nuclei of the metabolites that are in chemical exchange with those of water molecules and detecting a reduction in MRI signal in the water pool resulting from continuous chemical exchange. However, CEST signal can easily be compromised by artifacts. Since CEST is based on chemical shift, it is very sensitive to field inhomogeneity which may arise from poor initial shimming, subject respiration, heating of shim iron, mechanical vibrations or subject motion. This is a particular problem for molecules that resonate close to water, such as -OH protons in glycogen, where small variations in chemical shift cause misinterpretation of CEST data.

The purpose of this thesis was to optimize the CEST MRI sequence for glycogen detection and implement a real-time simultaneous motion and shim correction and measurement method. First, analytical solution of the Bloch-McConnell equations was used to find optimal continuous wave RF pulse parameters for glycogen detection, and results were validated on a phantom with varying glycogen concentrations and *in vivo* on human calf muscle. Next, the CEST sequence was modified with double volumetric navigators (DvNavs) to measure pose changes and update field of view and zero- and first-order shim parameters. Finally, the impact of $B_0$ field fluctuations on the scan-rescan reproducibility of CEST was evaluated *in vivo* in 9 volunteers across 10 different scans.

Simulation results showed an optimal RF saturation power of 1.5μT and duration of 1s for glycoCEST. These parameters were validated experimentally *in vivo* and the ability to detect varying glycogen concentrations was demonstrated in a phantom. Phantom data showed that the DvNav-CEST sequence accurately estimates system frequency and linear shim gradient changes due to motion and corrects resulting image distortions. In addition, DvNav-CEST was shown to yield improved CEST quantification *in vivo* in the presence of motion and motion-induced field inhomogeneity. $B_0$ field fluctuations were found to lower the reproducibility of CEST measures: the mean coefficient of variation (CoV) for repeated scans was 83.70 ± 70.79 % without shim correction. However, the DvNav-CEST sequence was able to measure and correct $B_0$ variations, reducing the CoV to 2.6 ± 1.37 %. The study confirms the possibility of detecting glycogen using CEST MRI at 3 T and shows the potential of the real-time shim and motion navigated CEST sequence for producing repeatable results *in vivo* by reducing the effect of $B_0$ field fluctuations.

# Table of Contents

# List of Figures

# List of Tables

# List of Acronyms

AREX – Relaxation Compensated Chemical Exchange Saturation Transfer

APT – Amide Proton Transfer

BM – Bloch-McConnell

$B_0$ – Static Magnetic Field

B1 – Radiofrequency Magnetic Field

CEST – Chemical Exchange Saturation Transfer

CoV – Coefficient of Variation

CW – Continuous Wave

DIACEST – Diamagnetic Chemical Exchange Saturation Transfer

DTI – Diffusion Tensor Imaging

DvNav – Double Volumetric Navigator

EPI – Echo Planar Imaging

FID – Free Induction Decay

FISP - Fast Imaging with Steady State Free Precession

FLEX – Frequency Labeled Exchange

FT – Fourier Transform

glycoCEST - Chemical Exchange Saturation Transfer for glycogen detection

GAGCEST – Glycosaminoglycan Chemical Exchange Saturation Transfer

GRE – Gradient Recalled Echo

MoCo – Motion Correction

MRS – Magnetic Resonance Spectroscopy

MT – Magnetization Transfer

MTC – Magnetization Transfer Contrast

$MTR_{asym}$ – Magnetization Transfer Ratio Asymmetry

MRI – Magnetic Resonance Imaging

Nav – Navigator

NMR – Nuclear Magnetic Resonance

NoCo – No Correction

NoMo – No Motion

NOE – Nuclear Overhauser Effect

PARACEST – Paramagnetic Chemical Exchange Saturation Transfer

PCC – Pearson Correlation Coefficient

PET – Positron Emission Tomography

PTR – Proton Transfer Ratio

PW – Pulsed Wave

RARE - Rapid Acquisition with Relaxation Enhancement

RF – Radio Frequency

ROI – Region of Interest

SAFARI - Saturation with Frequency Alternating Radio Frequency Irradiation

SE – Spin Echo

ShimCo – Shim Correction

SNR – Signal to Noise Ratio

Std – Standard Deviation

TE – Echo Time

TGSE - Turbo Gradient Spin Echo

TR – Repetition Time

vNav – volumetric Navigator

# Chapter 1

# Introduction

MRI is a non-ionizing radiation imaging method that makes use of the magnetic properties of certain atomic nuclei. Different elements in the human body can be used as the source of the MRI signal such as Hydrogen[1], Carbon[13], Sodium[23], Phosphorus[31] and others. However, due to the abundance of hydrogen in water in human, hydrogen is the most commonly used element in MRI. Hydrogen[1] is not only bound in water, but also in other metabolites such as N-acetylaspartate (NAA), creatine, lactate, glycogen etc. MR spectroscopy (MRS) is the method of choice to quantify many metabolites. However, in-vivo measurement of certain endogenous metabolites, such as glycogen remains challenging due to their small concentration in the human body. For example, the maximal attainable glycogen concentration in human muscle is about 4 g per 100 g wet muscle (Hansen et al., 1999). This means that $^{1}$H MRI and MRS are unable to image glycogen. Moreover, the glycogen resonance overlaps with signal from other metabolites which makes its detection even more difficult. Although several techniques have been introduced for molecular imaging of glycogen *in vivo*, few have found their way into clinical settings. Briefly, positron emission tomography (PET), although highly sensitive (Herrero et al., 2007, Witney et al., 2014) involves the use of radioactive tracers, which are invasive. Furthermore, its spatial resolution is poor.Carbon[13] nuclear magnetic resonance spectroscopy ($^{13}$C MRS) can provide a direct, noninvasive nonionizing measurement of glycogen concentration in various organs (Casey et al., 2000, Lei et al., 2007, Tomiyasu et al., 2010), however it requires costly hardware upgrades and $^{13}$C isotopes, not routinely available on clinical MRI scanners.

During the early 2000, a new MRI contrast method based on chemical exchange of protons with water was proposed. This method provides molecular information about tissue but is based on imaging rather than spectroscopy. This new technique, referred to as Chemical Exchange Saturation Transfer (CEST) MRI (Ward, K. M., Aletras & Balaban, 2000) indirectly detects molecules with exchangeable protons by exploiting the chemical exchange that occurs between dilute protons, such as glycogen and free water protons when the magnetization of the former is selectively saturated.

Glycogen CEST uses frequency selective saturation pulses to saturate the magnetization of hydrogen nuclei attached to the hydroxyl group (-OH). However, the rapid exchange of -OH protons (more than $10^3$ per second (Zijl. et al., 2007), small chemical shift difference from bulk water protons (0.5 – 1.5 ppm), MRI magnetic field inhomogeneity, and temperature and pH dependence (Sun, van Zijl & Zhou, 2005) complicate the detection of glycogen/hydroxyl proton groups using CEST MRI.

CEST acquisitions are typically repeated with saturation pulses with a broad range of chemical shifts to generate the CEST Spectrum (also known as z-spectrum), which is a map of the signal intensity as a function of the frequency of the presaturation pulses. Multiple spectral offsets are needed to sufficiently sample the z-spectrum, making the acquisition time long. This long scan time causes CEST MRI susceptible to subject motion and fluctuation in $B_0$ field inhomogeneity. To reduce the overall scanning time, rapid MRI acquisition techniques such as Rapid Acquisition with Relaxation Enhancement (RARE) (Liu et al., 2009), Echo Planar Imaging (Liepinsh & Otting, 1996, Sun et al., 2013), Gradient and Spin Echo (GRASE)(He Zhu, 2010), Variably-accelerated Sensitivity Encoding (vSENSE) (Zhang et al., 2017), keyhole (G., E. & E., 2012), optimized spiral-centric-reordered GRE approaches (Zaiss, Ehses & Scheffler, 2018), as well as True Fast Imaging with Steady State Free Precession (FISP) (Shah et al., 2011) have been adapted to provide CEST signal. These fast imaging techniques are susceptible, however, to high radiofrequency (Wolfsdorf & Weinstein, 2003) power absorption, magnetization transfer (MT) effects arising from multiple refocusing excitation pulses, or field inhomogeneities, effects that are exacerbated on high field MRI scanners.

This thesis focuses on optimization CEST sequence for glycogen detection. Continuous wave (CW) RF irradiation parameters that maximize the CEST signal for glycogen were selected and inserted in the 2D single-shot EPI sequence. The CEST EPI sequence was further optimized to include double volumetric navigators (DvNavs) for simultaneous real-time motion and shim measurement and correction in the detection of skeletal muscle glycogen. The technique was validated both *in vitro* and *in vivo* on a 3 T Siemens Skyra scanner. A scan-rescan reproducibility test was also performed to demonstrate the stability of the proposed technique.

## Thesis outline

This thesis presents a novel method to detect glycogen using optimized motion and shim navigated CEST MRI sequence to correct simultaneously for $B_0$ fluctuations and artefacts caused by subject motion. This was followed by validation of the scan-rescan stability of the technique for producing repeatable CEST results *in vivo*. The thesis includes three independent but related papers in chapters three, four and five. Each chapter contains various aspects of the methodology, research and findings. A comprehensive introduction provides the necessary background for the work. As a complete document it contains necessary repetition due to the fact that each core chapter is being presented as an independent article. **Chapter 2** presents the basic principles behind MRI and the relevant background of the CEST technique followed by a literature review of motion and shim correction in MRI.

**Chapter 3** describes optimization of CW RF irradiation parameters that maximize the CEST signal during glycogen measurement. The saturation power and duration used for application of glycogen detection are based on the findings of this chapter.

**Chapter 4** presents the implementation of 3D Double Volumetric Navigators to perform simultaneous real-time motion and shim measurement and correction in glycoCEST MRI. The performance of navigators in estimating changes in zero- and first-order shin, and application of DvNavs *in vivo* in the presence of motion is discussed in this chapter.

**Chapter 5** describes an investigation of the reproducibility of *in vivo* measurements in the presence and absence of field inhomogeneity using the motion and shim navigated CEST sequence.

Finally, **chapter 6** provides a comprehensive discussion, highlighting the most important findings of this thesis. The limitations are discussed, and recommendations are made for further studies using CEST MRI.

Chapter 4 is a journal article (Simegn et al., 2018) that has been peer reviewed and published in Magnetic Resonance in Medicine (MRM). Chapters 3 and 5 have been prepared as manuscripts to be submitted for publication. Part of chapter 3 has been presented at the 2017 postgraduate research day of the Department of Human Biology, Department of Integrative Biomedical Sciences, and Department of Pathology of University of Cape Town. Works from chapter 4 were accepted for

presentation at the International Society of Magnetic Resonance in Medicine (ISMRM) motion correction in MRI and MRS workshop in September 2017, Cape Town, South Africa and at the 26th Annual meeting of the ISMRM in June 2018, Paris, France. Part of chapter 5 has been presented at the 7th international workshop on Chemical Exchange Saturation Transfer Imaging, November 2018, Beijing, China.

I am the primary author of this thesis, but the papers were written with the assistance of 4 co-authors. Dr. Ali Alhamud identified the problem, conceptualized parts of chapter 4 and assisted with overall supervision. Assoc Prof. Andre van der Kouwe assisted technically in the modification and implementation of EPI navigators to the CEST sequence. He also supervised other parts of the work, helped in the preparation of glycogen phantoms used in the initial testing and provided a space to work at Athinoula A. Martinos Center for Biomedical Imaging. Dr. Frances Robertson supervised the whole work, guided, provided suggestions and helped me with editing and revisions. Professor Ernesta Meintjes followed up the whole work and provided valuable suggestions. I modified the sequences, performed the experiments and data analysis, wrote and formulated the articles and gave them to the co-authors for comment.

# Chapter 2

# Background

## 2.1. Principles of Magnetic Resonance Imaging

Magnetic Resonance Imaging (MRI) is a relatively new technology with its foundations beginning during the year of 1946. It was pioneered by Felix Bloch and Edward Purcell, who were awarded the Nobel Prize in 1952, for their independent discovery of the nuclear magnetic resonance (NMR) phenomenon. They discovered the phenomena of nuclear induction that enabled the development between 1950 and 1970 of many scientific techniques that exploited Nuclear Magnetic Resonance (Harris et al., 2002) for chemical and physical molecular analysis. In 1971 Raymond Damadian (Damadian & Raymond, 1971) showed that nuclear magnetic relaxation times of tissues and tumors differed motivating scientists to use MRI to study disease. Lauturbur (Lauterbur, 1973) and Mansfield subsequently developed magnetic resonance into an imaging technique. The introduction of computerized tomography (Proctor & Yu, 1950) by Hounsfield in 1973 (Hounsfield, 1973), echo-planar imaging (a rapid imaging technique) in 1977 by Mansfield (Mansfield, 1977), and the development of different contrast mechanisms to improve the visibility of internal body structures enabled MRI to become a powerful imaging modality, which is the preferred, and safest technique in many areas of medicine and scientific research.

MRI has revolutionized our ability to obtain images of the living human body, highlighting both anatomy and function. Compared to other imaging modalities, MRI offers a large range of contrast mechanisms that can improve the visualization of different tissue types and physiological events.

This chapter presents the fundamental principles of NMR and MRI signal acquisition, followed by the concept of chemical exchange saturation transfer MRI and MRI artifacts and reduction approaches already well known in MRI.

### 2.1.1. Source of MR signal

The basis of MRI is the interaction between the magnetization of certain nuclei (usually hydrogen nuclei of water) in the human body and different external magnetic fields that are generated by the MRI scanner. An MR system consists of different electromagnetic coils to generate the various magnetic fields including: 1) a coil to generate the static magnetic field (the B0 field), 2) a

radiofrequency (RF) coil to transmit (receive) a radio signal into (from) the body part being imaged, and 3) gradient coils to provide spatial localization of the MR signals.

Protons, electrons, and neutrons possess spin, which is an intrinsic form of quantum angular momentum carried by elementary particles, composite particles, and atomic nuclei. Spin comes in multiples of 1/2 and can be positive or negative. Individual unpaired electrons, protons, and neutrons each own a half spin. Two or more particles with opposite spins can pair up and eliminate the apparent manifestations of spin. In NMR, it is the unpaired nuclear spins that are of importance. Basic MR imaging arises from the physics of the element hydrogen, which is abundant in human tissue in the form of water and lipid (fat) molecules. The spinning hydrogen nucleus is a single proton and exhibits a magnetic moment vector, $\vec{\mu}$.

In the body, the direction of the magnetic moment of the hydrogen nuclei is randomized by thermal radiation (Figure 2.1a). In the classical mechanics, the net magnetization ***M***, which may vary as a function of time *t*, is defined as the overall sum of magnetic moments $\mu_j$ in a given volume and is equal to zero.

$$M(t) = \sum_j \vec{\mu}_j = 0 \quad \text{[2.1]}$$

### *Polarization*

In the presence of an external magnetic field (the $\boldsymbol{B_0}$ field), the magnetic moment of spins tends to align either in the direction of the $B_0$ field (the lower energy state) or the opposite direction (the higher energy state) with a small excess in the direction of the $\boldsymbol{B_0}$ field (Figure 2.1b).

In addition to this alignment, spins also precess at a frequency (called the Larmor frequency, $\boldsymbol{\omega_0}$) that depends on both the field strength ($\boldsymbol{B_0}$) and the gyromagnetic ratio ($\gamma$) for the particular atomic nucleus.

$$\omega_0 = \gamma B_0 \quad \text{[2.2]}$$

where for hydrogen, $\gamma$ = 42.58 MHz /T (or $267.513 \times 10^6$ rad/s/T).

The alignment of magnetic dipole moments parallel or antiparallel to $\boldsymbol{B_0}$ gives rise to a non-zero net magnetization vector, **M**, which has longitudinal ($\boldsymbol{Mz}$) and the transverse ($\boldsymbol{M_{xy}}$) components. Initially, **M** is aligned with the static magnetic field of the MRI scanner $\boldsymbol{B_0}$, which also defines the z-axis, therefore $\boldsymbol{M_z}=\boldsymbol{M_0}$ and $\boldsymbol{M_{xy}}=0$. However, $\boldsymbol{Mz}$ is too small to be measurable and energy needs

to be added perpendicular to the $B_0$ field to tip M into the transverse plane and generated an MR signal. This process is called excitation.

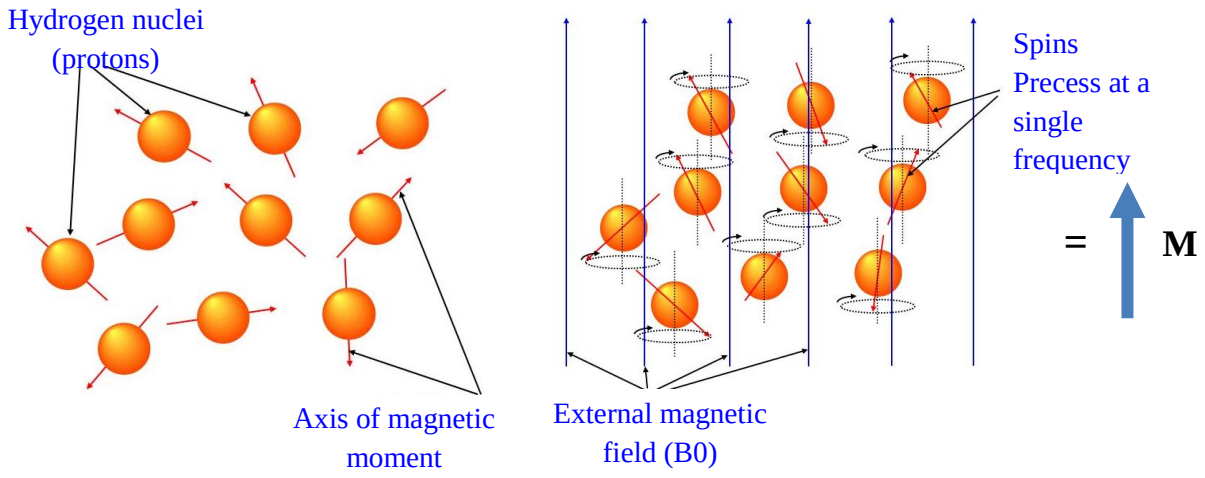


Figure 2.1**:** Demonstration of the precession of protons in the absence and presence of $B_0$ field. (a) in the absence of $B_0$ field, protons (spins) assume a random orientation of magnetic moments, producing a net magnetization of **M = 0**. (b) in the presence of external static magnetic field, $\mathbf{B_0}$, the individual magnetic moments can assume any of the two possible orientations, spin-up or spin-down, and precess about $\mathbf{B_0}$, producing a net magnetic moment of **M**.

### *Excitation*

While the net magnetization ***M*** is frozen in the absence of excitation, the application of an RF pulse at the Larmor precession frequency (on resonance) and perpendicular to the main magnetic field $\boldsymbol{B_0}$ causes ***M*** to precess around $\boldsymbol{B_0}$ at the Larmor frequency until the excitation radiofrequency pulse is turned off (Figure 2.2). The angle of precession (flip angle) for transverse magnetic field ($\boldsymbol{B_1}$), generated by applying an RF pulse with duration ***t*** to a coil, is $\boldsymbol{\alpha = 2\pi\, \gamma B_1 t}$. When the flip angle is $90^0$, the longitudinal component, ***Mz***, will be equal to zero while the transverse component $\boldsymbol{M_{xy} = M}$.

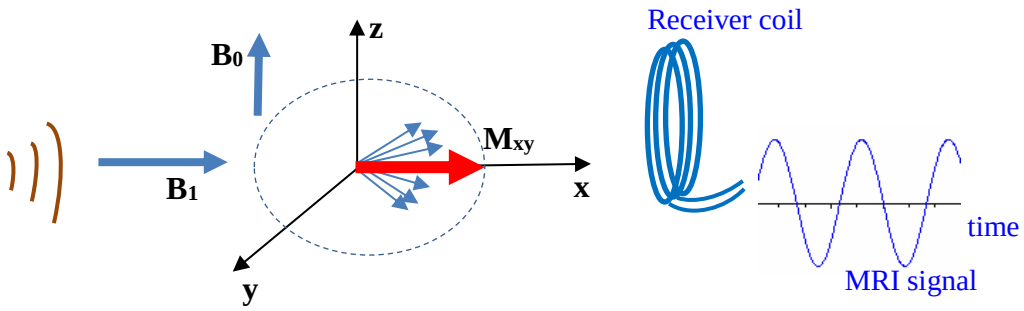


Figure 2.2**:** Illustration of MRI signal induction in the RF coil due to precessing of Magnetization

### *Signal acquisition and tissue contrast*

One of the main advantages of the RF excitation is bringing the spins into phase in the transverse plane. After the RF pulse is turned off, the magnetic properties of each nuclei change the local magnetic field causing some to precess faster and others slower. Gradually the nuclei lose their phase coherence and the net transverse magnetization becomes zero. The rate of dephasing is exponential, resulting in an exponentially decaying sinusoidal signal named the "Free Induction Decay (FID)". The rate of decay is determined by the magnetic interaction between the spins and is called the "spin-spin" relaxation or transverse relaxation characterized by relaxation time $T_2$. $T_2$ is defined as the time it takes for the transverse magnetization to decay to 37 % of its initial value (i.e. loses 63 % of its maximum signal).

Due to macroscopic differences in the static magnetic field (such as nearby iron or gas and their associated electromagnetic fields) even within uniform tissues, protons will precess at very slightly different rates and get out of phase with each other. The dephasing of protons due to these field inhomogeneities causes tissue magnetization to drop off more rapidly than expected from the $T_2$ constant. This dephasing of the transverse magnetization is a combination of two effects: the first related to intra- and inter-molecular magnetic field differences ($T_2$) and the second related to fixed macroscopic field differences due to the presence of different tissues (ΔB). The combination of these intrinsic and extrinsic effects is referred to as $T_2^*$ and can be expressed using the following formula.

$$\frac{1}{T_2^*} = \frac{1}{T_2} + \gamma \Delta B \quad \text{.....} \quad [2.3]$$

As the nuclei precess in the transverse plane they give up their energy to the molecules in the surrounding lattice. As they do so they return to the lower energy state and the longitudinal magnetization ($\boldsymbol{M_z}$) recovers exponentially. This is called "spin-lattice" or longitudinal relaxation. The rate at which this happens is determined by the time constant $\boldsymbol{T_1}$ which is the time it takes for $\boldsymbol{M}$ to recover to 63% of its maximum value (Figure 2.3).

What is measured in an MRI experiment is the magnetization in the transverse plane, as the spins precess around $B_0$. This causes a change in flux in a receiver coil, inducing current in the coil according to Faraday's law. This induced current is the MRI signal or FID. The equation of motion of the magnetization $\boldsymbol{M}$ that describes precession of the magnetization around $\boldsymbol{B_0}$, decay of transverse magnetization with time constant $\boldsymbol{T_2}$ and re-growth of the longitudinal magnetization with time constant $\boldsymbol{T_1}$ is generally given by the Bloch equation (Bloch, 1946):

$$\frac{dM}{dt} = \boldsymbol{M}\, x\, \gamma \boldsymbol{B} - \frac{(M_x i + M_y j)}{T_2} - \frac{(M_z - M_0)}{T_1} \quad \text{..... [2.4]}$$

In a reference frame rotating at the Larmor frequency, the solution to this set of differential equations is:

$$M_z(t) = M_0\left(1 - e^{-\frac{-t}{T_1}}\right) \text{ and } M_{xy}(t) = M_{xy}(0)e^{-\frac{-t}{T_2}} \quad \text{.....[2.5]}$$

Where $\boldsymbol{M_0}$ represents the equilibrium magnetization, $\boldsymbol{M_z}$ and $\boldsymbol{M_{xy}}$ are longitudinal and transverse magnetizations after excitation, and $\boldsymbol{T_1}$ and $\boldsymbol{T_2}$ are the spin-lattice and spin-spin relaxation time constants, respectively.

The MR image signal intensity is determined by mainly three basic parameters: 1) proton density, 2) $\boldsymbol{T_1}$ relaxation time, and 3) $\boldsymbol{T_2}$ relaxation time, which gives rise to Proton density-weather, $\mathbf{T_1}$-wighred and $\mathbf{T_2}$-weithed images, respectively. Proton density is the concentration of protons in the tissue in the form of water and macromolecules (e.g. proteins, fat, etc.) that resonate and give rise to the NMR signal. The contrast of MR image can be manipulated by two most important parameters: the repetition time (TR) and the echo time (TE). TR is the time between consecutive RF pulses whereas TE is the time between the initial RF pulse and the echo. $\boldsymbol{T_2}$ and $\boldsymbol{T_1}$ contrasts in the MR image can be manipulated by changing TE and TR (Figure 2.3). Short TE and short TR results in $T_1$-weighted images while long TE and long TR produces $T_2$-weighted images. $T_1$-weighted images portray anatomy, and, if contrast medium is used, may also show pathology.

However, $T_2$-weighted images provide the best portrayal of disease, because many tissues that are involved in pathologic processes have a higher  than normal water content, and the fluid causes the affected areas to appear bright on $T_2$-weighted images (Westbrook, 2016, Westbrook, Roth & Talbot, 2011).

By making TR large and TE small as compared to $T_1$ and $T_2$ of the tissue, respectively, the decay effects have little influence and the image is primarily proton density weighted. Table 2.1 shows the different relative time lengths of TR and TE for different types of contrast weighting.

Due to their varied water content and surroundings, different parts of the human body have different relaxation times (Table 2.2).

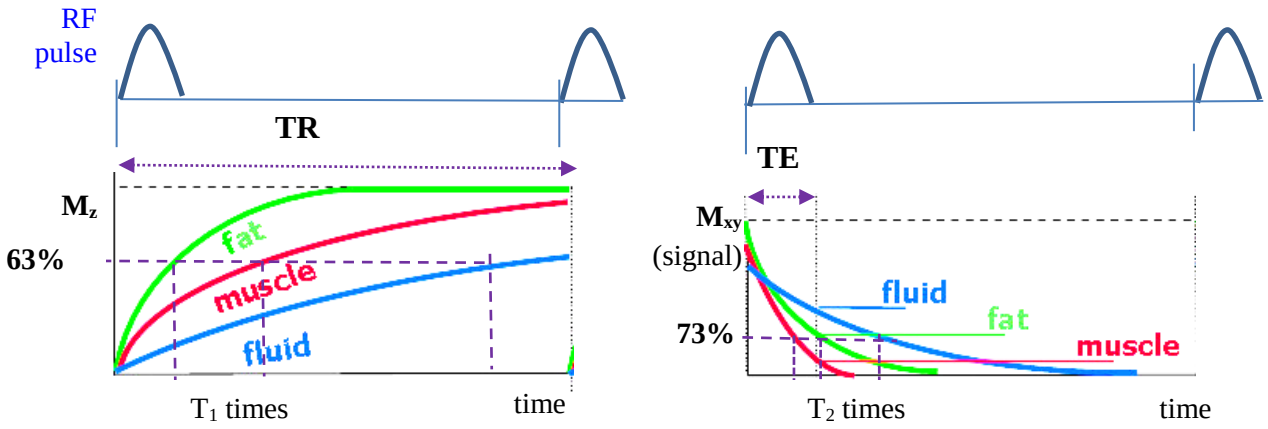


Figure 2.3**:** Illustration of the $T_1$ and $T_2$ relaxation times for different tissues as a function of TR and TE.

| | **Short TR** | **Long TR** |
|---|---|---|
| **Short TE** | $T_1$-weighted | Proton Density (PD) |
| **Long TE** | Not good for imaging (mixture of $T_1$ and $T_2$) | $T_2$-weighted |

Table 2.1**:** Influence of TR and TE on MR image contrast weighting

| Tissue | $T_2$ (ms) | $T_1$ (ms) |
|---|---|---|
| Liver | 42±3 | 812±64 |
| Skeletal muscle | 50±4 | 1412±13 |
| Heart | 47±11 | 1471±31 |
| Kidney | 56±4 | 1194±27 |
| White matter | 69±3 | 1084±45 |
| Gray matter | 99±7 | 1820±114 |
| Blood | 275±50 | 1932±85 |

Table 2.2: $T_1$ and $T_2$ relaxation times at 3 T measured at $37^0$C (Stanisz et al., 2005)

### *MR signal localization*

Spatial localization of MR signal is achieved by manipulating the precession frequency of the nuclei in a predictable way using current carrying gradient coils, which are designed to produce a desired spatially-varying magnetic field gradient. The secondary magnetic field created by these gradient coils alters the main magnetic field such that the resonance frequency of protons to varies as a function of position.

There are three sets of gradient coils, one for each direction: the *x*-, *y*-, and *z*-gradients. The signal received from a region of a sample at time *t* (E. Mark Haacke et al., 1999) can be written as:

$$S(t) \propto \iiint \boldsymbol{\rho}(\boldsymbol{r}) e^{i\phi(t)} dxdydz \quad \text{..... [2.6]}$$

where $\boldsymbol{\rho}(\boldsymbol{r})$ is the spin density and $\phi(t)$ is the phase that can be expressed as:

$$\phi(t) = \gamma(G(r).r)t \quad \text{..... [2.7]}$$

and the field gradient G(r) is:

$$G(r) = G_z i + G_y j + G_z k \quad \text{..... [2.8]}$$

The variation in the magnetic field allows for spatially-selective excitation in the slice direction, as well as further localization via phase encoding and frequency encoding of the received signal. By applying a called slice select gradient, $G_{SS}$ during excitation, only spins that match the resonance condition are excited (Figure 2.4a) enabling selection of the imaging slice. Similarly, by applying a

frequency encoding gradient, $G_{FE}$ during readout, the location of a signal with a specific frequency can be determined (Figure 2.4b). Localization along the third axis is done by manipulating the phase of the protons using a phase encoding gradient, $G_{PE}$ (Figure 2.4c). When this gradient is applied, the spin resonance frequencies are modified, inducing dephasing, When $G_{PE}$ is switched off protos precess at the same frequency, but have accumulated a phase that depends on their position along the direction of $G_{PE}$.

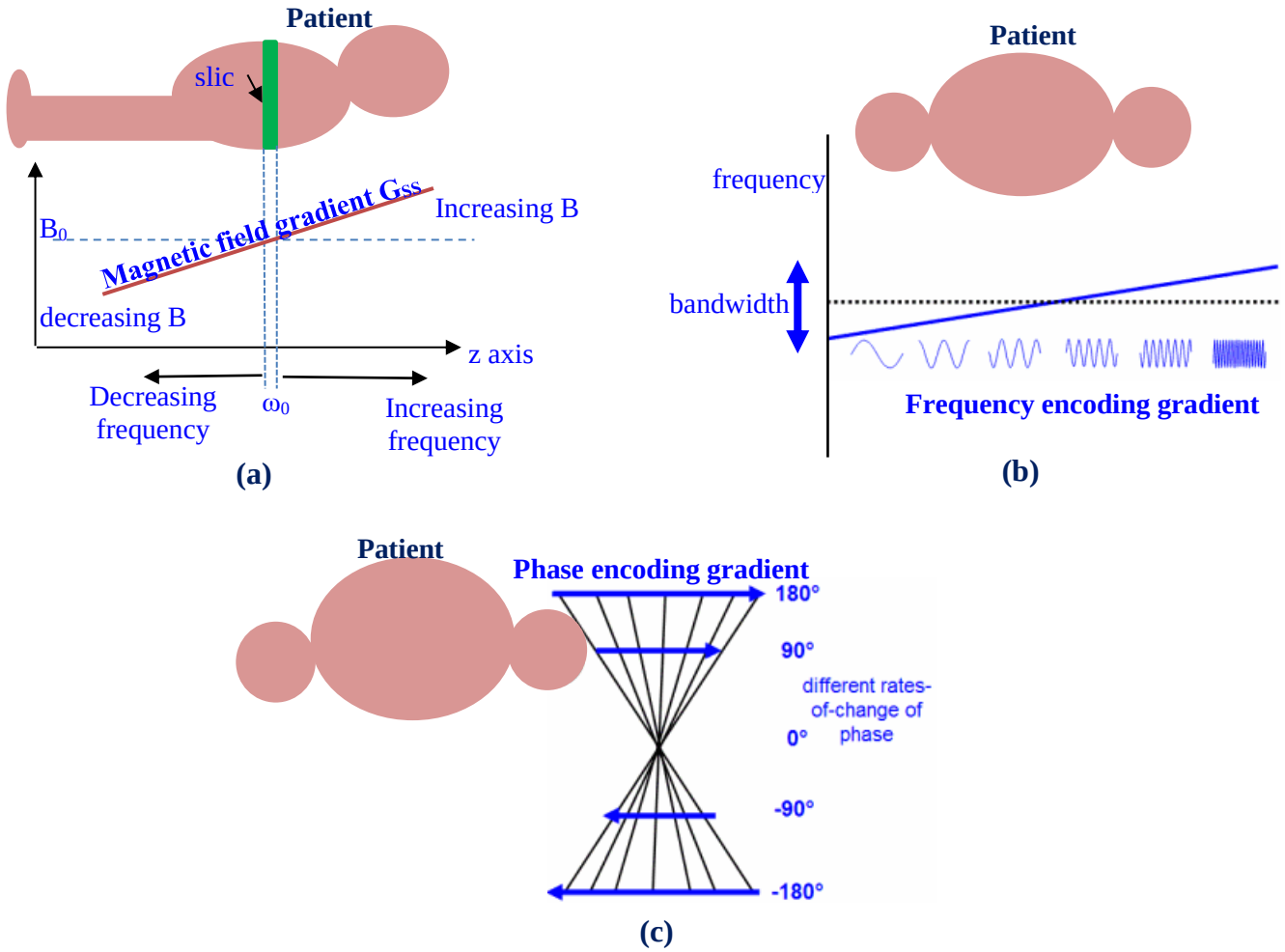


Figure 2.4: **(a) Slice select selection**. slice of tissue is selected by applying $G_{SS}$ at the same time point with the RF excitation pulse. The position along the gradient (z axis in this case) determines ω, resonance only occurs where this matches $\omega_0$, defining a plane of that tissue perpendicular to the z-axis. **(b) Frequency encoding**, $G_{FE}$ is applied in the plane of the selected slice during readout. $G_{FE}$ determines the Larmor frequency according to position along its direction. **(c) Phase encoding**. Phase encoding gradient, $G_{PE}$, is applied in a direction along the selected image plane causing a range of proton magnetic moment phase shifts dependent on their position along the magnetic field gradient, slope and duration of the gradient.

Since it is not possible to measure more than one phase per frequency, repeated acquisitions are needed for many different phase-encoding gradient strengths. Hence excitation should be repeated for each different phase-encoding gradient that needs to be measured.

The MR scanner samples and digitizes the frequency-encoded signals it obtains from each phase-encoding run and stores the data in the rows of a matrix, which is known as K-space matrix (Figure 2.5). A two-dimensional (2D) Fourier transformation (FT) of the matrix results in the reconstruction of the image. The number of pixels in the image along the phase encoding direction is determined by the number of phase encoding steps. The coordinates of the image are the spatial coordinates x and y. The distribution MR signal components in the image is determined by their frequency, along the frequency encoding direction (in this case x), and by their change in phase with each phase encoding step, along the phase encoding direction (in this case y). The program that controls the timings and order of the encodings is called a pulse sequence.

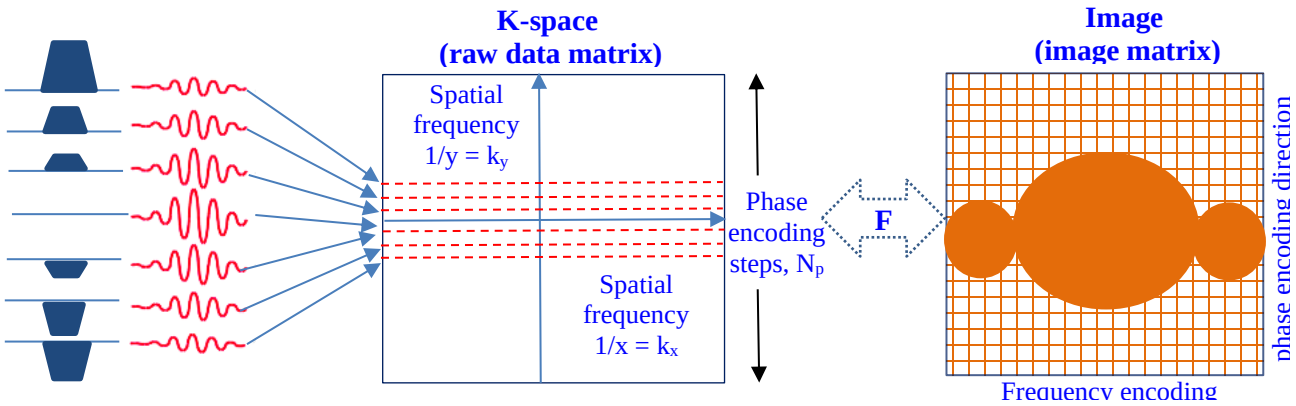


Figure 2.5: K-space acquisition and image reconstruction. The coordinates of k-space are the spatial frequencies ($\boldsymbol{k_x = 1/x}$ and $\boldsymbol{k_y = 1/y}$). The data points in k-space represent the spatial frequencies content of the image. The Fourier transform is used to reconstruct the image. In a Cartesian coordinate acquisition, the data points are stored line by line along the $k_x$ direction and each line corresponds to a separately sampled

### 2.1.2. MRI pulse sequences

An MRI pulse sequence is a set of radio frequency and gradient pulses (wave forms), usually applied repeatedly in MR image acquisition. The MR signal is controlled by the time interval between pulses, and the amplitude and shape of the gradient waveforms. These also affect the characteristics of the image. There are two fundamental types of MR pulse sequences: spin echo (SE) and gradient recalled echo (GRE). By tweaking and adding different parameters other MR sequences can be derived. MR pulse sequences can be either 2D, with one section (slice) excited

at a time, or 3D, with a volume of multiple sections excited and obtained in a single acquisition. Some of the widely used pulse sequences are discussed below.

### *Gradient Recalled Echo (GRE)*

The GRE sequence comprises a series of excitation pulses each separated by TR. An RF pulse is applied to partially flip the net magnetization vector into the transverse plane (Frahm, Haase & Matthaei, 1986). Gradients, are used to dephase (negative gradient) and rephase (positive gradients) transverse magnetization. Figure 2.6a show the different components of the GRE pulse sequence. The $G_{SS}$ is applied to select an imaging slice. Any dephasing of the spins across the slice that occurs due to this gradient is reversed by a rephasing $G_{SS}$ gradient with opposite polarity. Before the application of the readout gradient ($G_{FE}$), a negative dephasing gradient is applied, whose is half that area under the readout gradient, causing the spins to dephase. The spins get back into phase in the center of the readout period (at time TE). In the GRE sequence, TE is defined as the time between the mid-point of the excitation pulse and the mid-point of the data acquisition window. GRE sequences can generate 3 types of MRI contrasts: $\boldsymbol{T_1}$, $\boldsymbol{T_2^*}$ and proton density (PD). GRE is suitable for fast imaging due to low flip angles with ultrashort TR.

### *Spin echo (SE)*

The spin-echo pulse sequence is one of the earliest developed and is still widely used in different forms.

In this sequence, a 90° pulse is used to flip the net magnetization vector into the transverse plane (Hahn, 1950). As the spinning nuclei go through $\boldsymbol{T_1}$, $\boldsymbol{T_2}$, and $\boldsymbol{T_2^*}$ relaxation, the transverse magnetization is gradually dephased. To rephase the spinning nuclei, a 180° pulse is applied at a time equal to one-half of TE. When the nuclei are again in phase (at TE), an echo is produced and read (Figure 2.6b). The advantages of the SE sequence are high signal to noise ratio (SNR) and true T2 weighing. Most conventional SE sequences require long a TR for signal relaxation due to the 90-180-degree RF pair, increasing the acquisition time. Advances in MR imaging technology have enabled a reduction in acquisition time with the use of other fast SE derived sequences. However, the long TR is also essential for some applications to eliminate the effects of $\boldsymbol{T_1}$ of and generate $T_2$-weighted images.

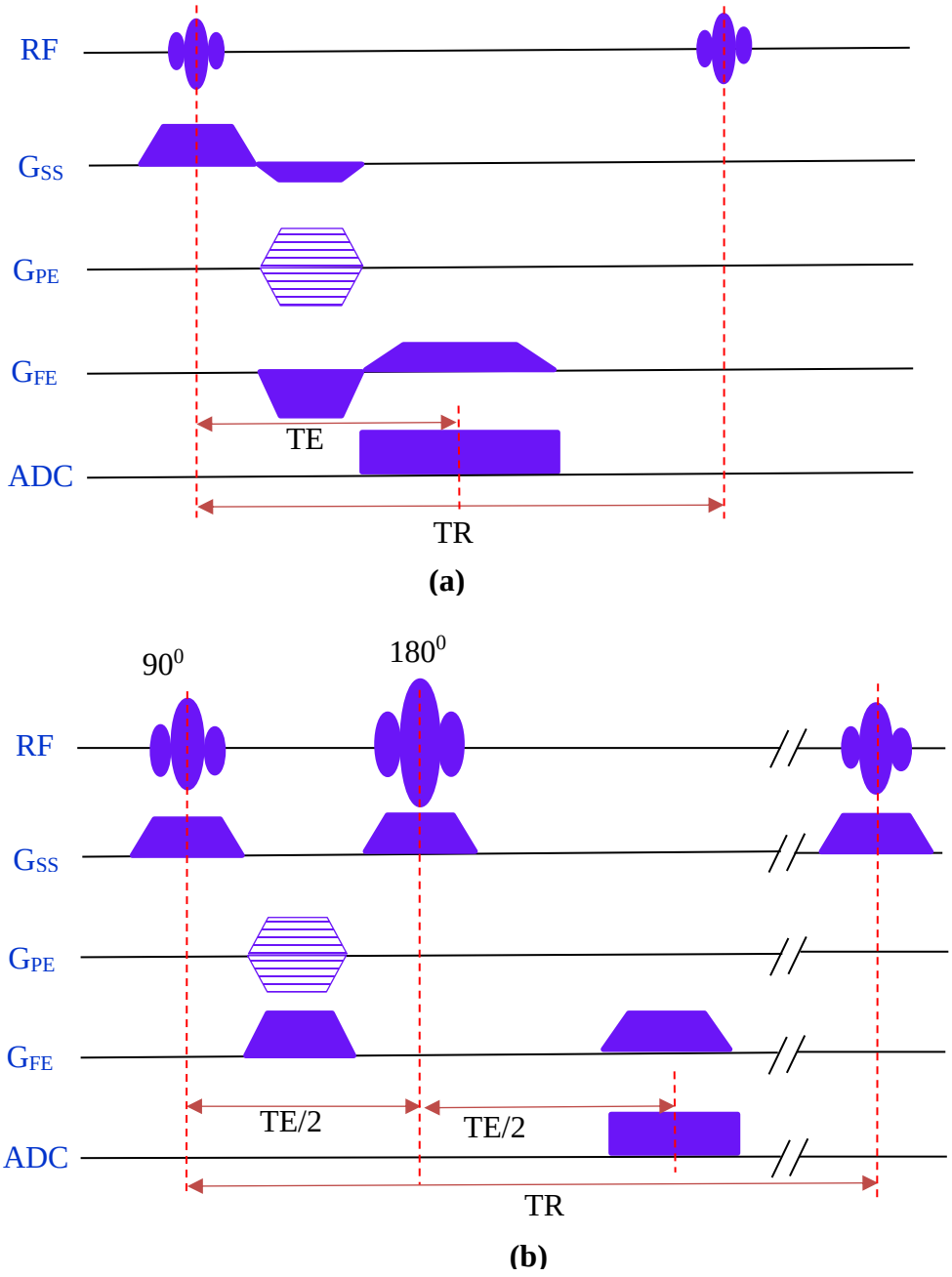


Figure 2.6: (a) simplified GRE pulse sequence diagram indicating the timing of gradients, including the reversal of GFE synchronized with RF excitation and data acquisition. (b) SE pulse sequence diagram with the RF refocused pulse. Spins initially in phase will be dephased at the end of the first TE/2, but recover their phase coherence after the refocusing pulse, producing a maximum signal (echo) at the end of second TE/2 period. Amplitude is shown vertically and time horizontally. RF is the excitation pulse, $G_{SS}$ is the slice select gradient, $G_{PE}$ is the phase encoding gradient, $G_{FE}$ is the frequency encoding gradient, ADC is the analog to digital conversion indicating the signal acquisition. After time interval TR the sequence is repeated for a different $G_{PE}$ strength (represented by parallel lines in the diagram)

### *Fast Spin Echo (FSE) or Multi-Echo Spin Echo (MESE)*

FSE sequence also known as Turbo Spin Echo (TSE) or MESE consists of a 90° RF pulse followed by a train of evenly-spaced 180° RF pulses applied alternately along the transverse plane to acquire several echoes per excitation (per TR). Each echo is encoded with a different phase encoding gradient. This is designed to reduce imaging time of SE sequence.

The spin echo occurs after dephased protons are re-phased by the $180^0$ pulse, thus reversing the fixed magnetic field inhomogeneities, while intrinsic $T_2$ dephasing continues unabated. After the protons become dephased at TE, they will continue to dephase and the 'echo' dies away but applying another 180-degree pulse will rephase them again. This can be repeated as many times as needed, each time generating an echo, reversing effects of fixed magnetic field inhomogeneities. As $T_2$ dephasing continues, at some point, the echo becomes too weak to be detected above the noise.

The total number of $180^0$ RF pulses and echoes is called the echo train length (ETL). In the FSE pulse sequence the acquisition time is greatly reduced with respect to a conventional SE sequence. Since many echoes are acquired each with a different TE, instead of just a single TE, there is an 'effective TE' ($TE_{eff}$) that reflects the ***T1***/***T2*** weighting of the sequence.

### *Echo Planar Imaging (EPI)*

The GRE sequence is inherently characterized by a short TR compared to the SE sequences. However, the conventional GRE still acquires a single line of k-space per excitation (per TR). Repeating a succession of phase encoding steps, to generate the whole MR image, increases the scanning time and renders the data susceptible to motion artefacts. Furthermore, many imaging technologies, such as CEST require repeating the acquisition multiple times. Fast techniques such as single-shot EPI (ss-EPI) (Mansfield, 1977, Rzedzian et al., 1983) were introduced in order to reduce acquisition times. The ss-EPI sequence utilizes rapidly switching gradients to acquire the entirety of k-space lines with a single excitation. By using varying gradient strengths, consecutive phase encoding steps can be obtained thereby completing the k-space matrix. Alternating the frequency encoding gradient enables sweeping back and forth across the frequency encoding direction with each phase encoding step. Each image can be acquired in less than 100 ms, with a

tradeoff in image quality. The EPI sequence can be either blipped or unblipped. In blipped-EPI, a small phase encoding gradient 'blip' is placed at each readout gradient reversal. This adds further phase encoding to the previous 'blip' making the acquisition easier and faster. However, in unblipped-EPI, a constant phase-encoding gradient is continuously used during an oscillating readout gradient. Figure 2.7 shows the timing diagram of a 'blipped' single shot Echo planar imaging (ss-EPI) pulse sequence timing diagram.

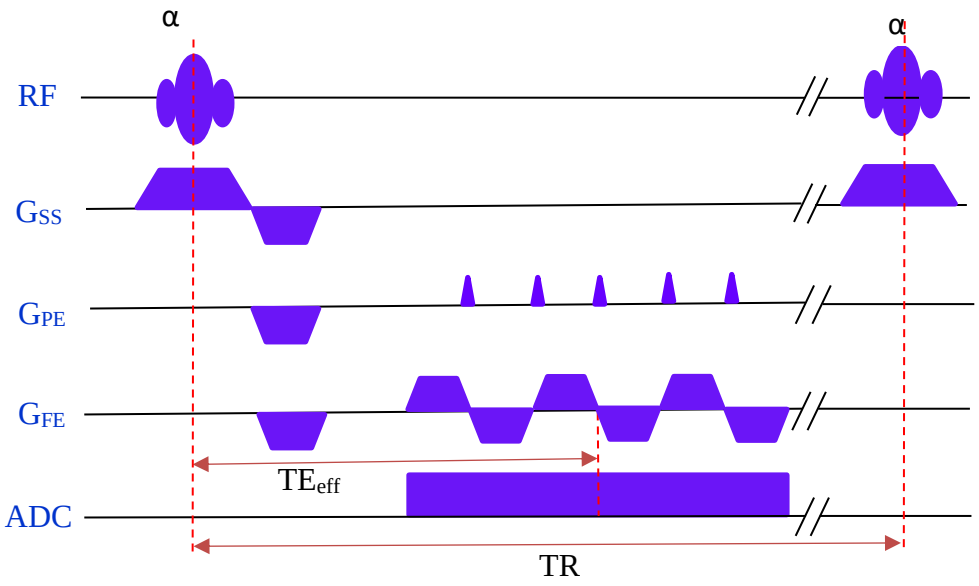


Figure 2.7**:** Blipped single-shot GRE-EPI pulse sequence timing diagram. A small phase-encoding gradient 'blip' is placed at each readout gradient reversal. $TE_{eff}$ is the effective echo time and α is the flip angle.

### *Artifacts in EPI Sequences*

EPI based sequences afford fast image acquisition times, but are more susceptible to various artifacts. Because of the successive application of gradients, EPI based sequences are very sensitive to magnetic field inhomogeneities. Furthermore, the successive application of gradients cause phase buildup across the sequence resulting in chemical shift displacement artefact. Chemical shift displacement or frequency difference between fat and water encoding can correspond spatially to as much as half of the image. Another EPI artefact is 'ghost" artefact. The polarity of the readout gradient in the EPI sequence is alternated. For image reconstruction, every alternate echo must be time-reversed before Fourier transformation. Small errors in gradient amplitudes and pulse sequence timings can cause a phase disparity between the odd and even

echoes and result in half-FOV ‘ghost’ artefacts (also known as Nyquist ghosts). Other factors including eddy-current effects, timing and amplitude errors related to the gradient hardware, and receiver anti-aliasing filter delays can be also the cause of ghost artifact (Sukumar, 1999). The influence of the above factors can be difficult to handle because they affect the odd and even echoes differently. Hence, effective fat suppression and phase correction are important in EPI based sequences.

### *Hybrid GRE-SE sequence (TGSE or GRASE)*

Turbo Gradient Spin Echo (TGSE) or Gradient and Spin Echo (GRASE) sequence is a mixture of FSE (using 180° rephasing pulses to create a spin echo train) and GRE (readout of several gradient echoes between each 180° pulse). During a single TR, several gradient echo trains can be recorded, with a signal weighting of the SE type. Each echo has a different phase encoding to fill the k-space more quickly. Using intermediary gradient echoes rather than spin echoes allows reduction of the number of 180° rephasing pulses, thereby reducing the quantity of RF energy deposited. This sequence is used primarily for T2-weighted imaging. Its advantages are shorter measurement time and reduced RF power deposition. Figure 2.8 shows the timing diagram of Hybrid Turbo Spin Echo/Gradient Echo pulse sequence.

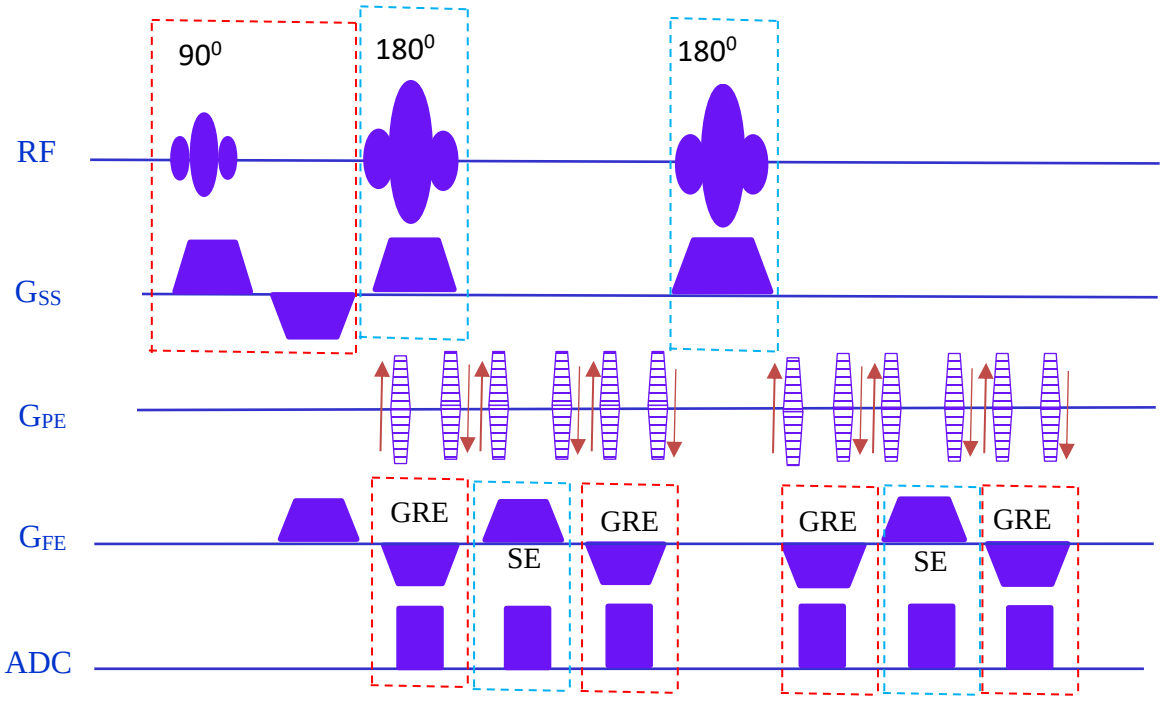


Figure 2.8**:** Illustration of TGSE sequence diagram with four gradient and two spin-echoes.

### 2.1.3. MRI scan parameters

During MRI acquisition, different parameters affect the resulting tissue contrast, image spatial characteristics, scan time and image noise characteristics. These can be classified into primary parameters (those that can be set directly) and secondary parameters (resulting from the primary parameters, which are used to describe the image) (Duerk, 1997). TR, TE, Flip Angle (FA), slice thickness, Field of View (FOV), Number of phase encoding steps ($N_{PE}$), Number of frequency encoding steps ($N_{FE}$), Bandwidth (BW) and Number of Excitations (NEX) are among the primary parameters. Signal to Noise Ratio (SNR), Scan time (TA), coverage, resolution and image contrast among secondary parameters that can be controlled by adjusting the primary parameters.

**BW** is a measure of frequency range involved in reception or transmission of a signal, the range between the highest and lowest frequency allowed in a signal. BW is apportioned to pixels along the frequency-encoding direction equally.

**FOV** is the dimension of the desired part of the object to be scanned. In a particular direction, the FOV is related to the bandwidth of the RF excitation pulse and the applied gradient strength G in that direction. For example, in the phase encoding direction:

$$FOV_{PE} = \frac{BW}{\gamma G_{PE}} \quad \text{[2.9]}$$

The FOV along with $N_{PE}$, $N_{FE}$ and slice thickness determines the spatial resolution (voxel size), which is the minimum distance that can be distinguished between two points. It is given by:

$$Voxel\ size = \frac{FOV_{PE}}{N_{PE}}\ X\ \frac{FOV_{FE}}{N_{FE}}\ X\ Slice\ thickness \quad \text{[2.10]}$$

**$N_{PE}$** and **$N_{FE}$** represent the number of pixels in the phase encoding direction and frequency encoding direction, respectively which are determined by the image matrix size.

**NEX** stands for the number of times the scan is repeated (number of signals averaged). It refers to how many times each line of k-space data is acquired during the scan.

**SNR** is the measure of the relative strengths of the signal with respect to the noise. Low SNR results in poor image quality. SNR depends on voxel size, BW, NEX, $N_{PE}$.

$$SNR \propto Voxel\ size\ x\ \frac{\sqrt{N_{PE} X\ NEX}}{\sqrt{BW}} \quad \text{[2.11]}$$

In 3D imaging, there is an additional phase-encoding step in the slice select direction ($N_z$) (partitions). Therefore, the SNR will be:

$$SNR_{3D} \propto Voxel\ size\ x\ \frac{\sqrt{N_{PE} X\ N_z X\ NEX}}{\sqrt{BW}} \quad \text{[2.12]}$$

Equation [2.9] shows that SNR in 3D imaging is higher than in 2D imaging. Specifically,

$$SNR_{3D} = \sqrt{N_z}\ x\ SNR_{2D} \quad \text{[2.13]}$$

Total scan time or Total acquisition time (TA) is dependent on TR, NPE and NEX (additionally on $N_z$ in 3D). It is given by:

$$\text{Scan time} = TR \times N_{PE} \times NEX \quad \text{[2.14]}$$

For fast spin-echo (FSE) imaging, NEX will be divided by the Echo train length (ETL). For 3D imaging, the above scan time will be multiplied by $N_z$.

Optimization of the above parameters may involve some trade-offs depending on the desired resolution, SNR and contrast and the allowable acquisition time.

## 2.2. Chemical Exchange Saturation Transfer (CEST) MRI

In MRI, image contrast is determined by properties of hydrogen nuclei embedded in water or fat ("free protons"). Hydrogen nuclei in molecules other than water and fat ("macromolecules" "bound protons" "solid pool protons") can also be the source of MRI signal. MRS allows direct detection of endogenous metabolites, containing hydrogen, including N-Acetylasparate (NAA), creating (Cr.), choline (Cho), myo-inositol (Ins), and glutamate (Glu) (Graaf, 01 November 2007). These metabolites can be robustly detected on a clinical MRI scanner with a field strength of 3 T, due to their adequate concentrations in the human body and their well separated chemical shifts in the MRS spectrum. However, in vivo measurement of certain molecules, such as glycogen, remains challenging due to their low concentration and resonance frequency that overlaps with other signals. As a result, they cannot be seen directly using conventional MRS technique. These types of molecules can be detected indirectly using off-resonance imaging, by means of magnetization transfer through proton exchange with the free water protons. This relatively new technique is called chemical exchange saturation transfer (CEST).

### 2.2.1. Chemical shift

Protons in different molecules experience a range of magnetic environments and shielding effects from the surrounding electrons. Thus, Larmor frequencies vary slightly from one type of molecule to another (Proctor & Yu, 1950). For example, if due to the circulation of electrons in a molecule a local magnetic field, $\mathbf{B}_e$ is created that opposes the static magnetic field, $\boldsymbol{B}_o$ ($\boldsymbol{B}_e$ is proportional to $\boldsymbol{B}_o$), the resulting magnetic field will be:

$$\mathbf{B} = \mathbf{B}_o - \mathbf{B}_e \quad \text{..... [2.15]}$$

Because the nucleus is partially shielded from the external magnetic field its Larmor frequency will be:

$$\boldsymbol{\omega = \gamma (B_o - B_e)} \quad \text{..... [2.16]}$$

The extent of shielding is influenced by structural features within the molecule. Chemical shift is defined as the relative difference in resonant frequency compared to a standard signal which is defined to be at 0 ppm.

$$\text{Chemical shift, } \delta = \frac{(frequency\ of\ signal - \ reference\ frequency)}{reference\ frequency} x\ 10^6 \quad \text{... [2.17]}$$

Conventionally tetramethylsilane (TMS) is used as a reference for $^1$H NMR (Harris et al., 2002). For most CEST experiments free water is used as a reference. The scale is expressed in parts per million (ppm) which is independent of the spectrometer frequency. Figure 2.9 shows the chemical shift scale in the conventional NMR spectrum.

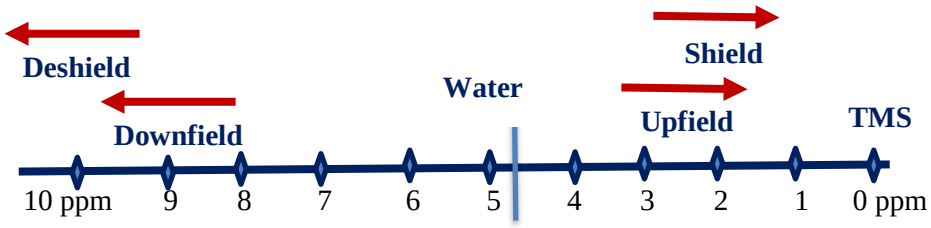


Figure 2.9: Chemical shift scale using Conventional NMR Spectrum

### 2.2.2. RF Saturation and Exchange

Saturation is a temporary state in which tissue shows approximately zero net magnetization (Wu, B. et al., 2016). Saturation is a form of suppression; suppression techniques include chemical (spectral) saturation, inversion recovery and spatial saturation in the field of view (Duerk, 1997).

The resonance frequency variation between different molecules allows the selective excitation of specific molecular protons without exciting others, through the delivery of an off-resonance radiofrequency pulse (Wolfsdorf & Weinstein, 2003). The subsequent interaction (chemical exchange) between these protons and water protons surrounding the molecules transfers the saturated magnetization to the water. As a result, the overall MR signal from water is lower than it would have been without the saturation transfer, giving an image contrast directly dependent on the concentration of the targeted molecule.

Protons in metabolites, small molecules, peptides and small mobile proteins have a different frequency distribution and exchange magnetization with water via mechanisms that are different from protons on large proteins, macromolecules and membranes (Zijl et al., 2003). Hence, off-resonance saturation transfer contrast can be classified in to two categories: magnetization transfer (MT) and CEST. MT is the physical process by which semi-solid macromolecules and their closely allied water molecules (the "bound" pool) cross-relax with protons in the free water pool.

On the other hand, CEST is the transfer of saturation from the solute (target molecule) pool to the water after exchangeable solute protons are selectively saturated using RF irradiation at their resonance frequency. The solute chemical species must have in its structure a $^{1}H$ proton that is exchangeable with those of water for this transfer to take place. The exchange of saturated protons from the solute pool with unsaturated protons from the bulk water pool then leads to a reduction in the water signal proportional to the concentration of solute pool (Figure 2.10).

In view of the low concentration of solute protons (μM to mM range), a single transfer of saturation is insufficient to show any discernable effect on water protons (Zijl. & Yadav, 2011). However, because the bulk water pool is much larger than the saturated metabolite proton pool, each exchanging saturated solute proton is replaced by a non-saturated water proton, which is in turn saturated via application of a long duration saturation pulse, progressively decreasing the water magnetization.

Concurrent, longitudinal relaxation returns the saturated proton spins to their thermal equilibrium state until the system reaches steady-state, or the saturation pulse is turned off. The reduction in the water signal can be imaged with any imaging readout scheme provided that the discrete chemical shift difference ($\Delta\omega$) between water and the exchangeable proton on the solute is

preserved, and the exchange rate, $k_b$, fulfils the slow to intermediate exchange condition on the NMR time scale defined as (Kogan, Hariharan & Reddy, 2013):

$$K_b \leq \Delta\omega \quad [2.18]$$

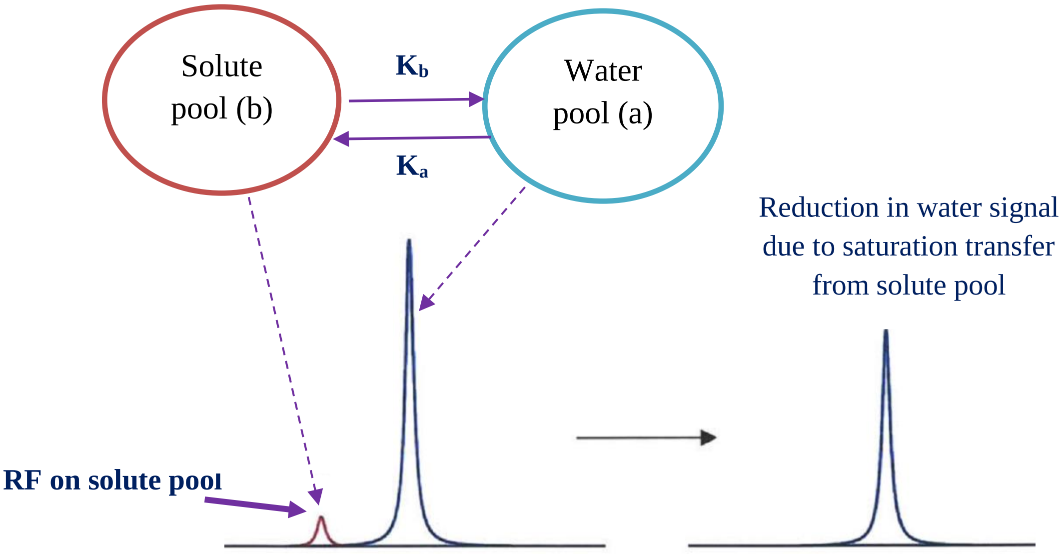

Figure 2.10: RF Saturation and exchange mechanism. When RF saturation pulse is applied to the exchangeable solute pool, the magnetization from the solute protons is nulled. The saturated protons then move to the larger water pool via chemical exchange with exchange rate $K_s$, while unsaturated protons from water move to the solute pool with exchange rate $K_w$, replenishing the magnetization.

### 2.2.3. CEST MRI contrast mechanism

CEST agents (molecules with exchangeable protons), can be categorized into two classes: paramagnetic CEST agents (PARACEST) and diamagnetic CEST agents (Kogan, Hariharan & Reddy, 2013, Zhou, Jinyuan & Zijl, 2006). Molecules with exchangeable protons capable of providing CEST signal combined with a paramagnetic metal ion (typically one of the lanthanides) are known as paramagnetic CEST (PARACEST) agents. PARACEST agents create larger chemical shifts between exchangeable protons, which allow for more selective irradiation and imaging of faster exchanging species. On the other hand, diamagnetic CEST (DIACEST) agents are endogenous molecules with exchangeable protons without paramagnetic ions (Wu, B. et al., 2016). Glycosaminoglycans, glycogen, myoinositol, glutamate, creatine are some examples of endogenous metabolites with exchangeable protons (Kogan, Hariharan & Reddy, 2013). Figure 2.11 demonstrates the DIACEST molecules relative chemical shift to that of water;

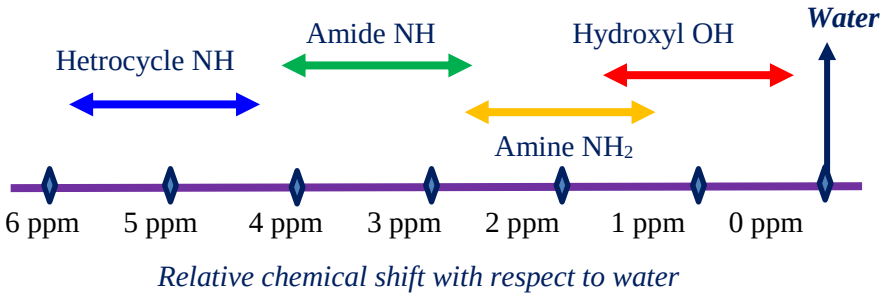


Figure 2.11**:** DIACEST molecules relative chemical shift with respect to water molecule

### 2.2.4. CEST exchange models

Many mathematical models are available to describe the CEST saturation transfer mechanism and guide optimization of the CEST signal. The simplest model is the two-pool model (Liu G, KWY. & MT., 2013), where the pools are the exchangeable proton pool (b) and bulk water proton pool (a) with proton chemical shift differences ($\Delta\omega$) and equilibrium exchange rate ($k_b$). The two-pool and three-pool models are shown in **Error! Reference source not found.**. The small pools represent exchangeable protons on small solute molecules and in the three-pool case, magnetization transfer from semi-solid macromolecules. The large pool represents bulk water protons. $T_1$ and $T_2$ are the longitudinal and transverse relaxation rates. M is the equilibrium magnetization, $\omega_b$, is the resonance frequency of the exchangeable proton of interest and $\omega_a$ is the resonance frequency of the water. $K_{ba}$ and $k_{ab}$, are the exchange rates of magnetization from pool *b* to pool a and vice versa.

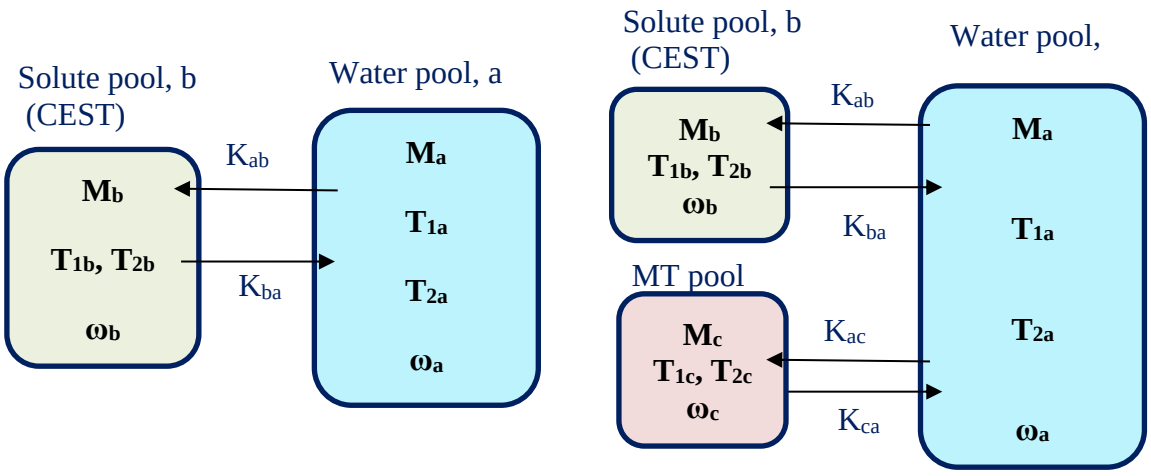


Figure 2.12**:** Two-pool (left) and three-pool (Woessner et al., 2005, Zhou, Jinyuan et al., 2004) exchange model for CEST modeling with solute pool and water pool, and MT pool.

Bloch-McConnell equations (McConnell, 1958), derived from the Bloch equation (Equation [2.5]) with the inclusion of magnetic effects between two or more pools of hydrogen atoms, are commonly used for quantitative description of the CEST process. The time-dependent Bloch-McConnell equations in the two-pool exchange model for CEST can be represented as (Zhou et al 2004):

$$\begin{bmatrix} \partial M_{ax}/\partial t \\ \partial M_{ay}/\partial t \\ \partial M_{az}/\partial t \\ \partial M_{bx}/\partial t \\ \partial M_{by}/\partial t \\ \partial M_{bz}/\partial t \end{bmatrix} = \begin{bmatrix} -k_{ab} & \Delta\omega_a & 0 & k_{ba} & 0 & 0 \\ \Delta\omega_a & -k_{ab} & -\omega_1 & 0 & k_{ba} & 0 \\ 0 & -\omega & -k_{ab} & 0 & 0 & k_{ba} \\ k_{ab} & 0 & 0 & -k_{ba} & \Delta\omega_b & 0 \\ 0 & k_{ab} & 0 & \Delta\omega_b & -k_{ba} & -\omega_1 \\ 0 & 0 & k_{ab} & 0 & -\omega_1 & -k_{ba} \end{bmatrix} \begin{bmatrix} M_{ax} \\ M_{ay} \\ M_{az} \\ M_{bx} \\ M_{by} \\ M_{bz} \end{bmatrix} - \begin{bmatrix} M_{ax}/T_{2a} \\ M_{ay}/T_{2a} \\ (M_{a0} - M_{az})/T_{1a} \\ . \\ . \\ . \\ M_{bx}/T_{2b} \\ M_{by}/T_{2b} \\ M_{b0} - M_{bz})/T_{1b} \end{bmatrix} \quad \text{..... [2.19]}$$

where $M_{ax,y,z}$ and $M_{bx,y,z}$ are the x, y and z magnetization components for bulk water and solute (labile) protons, respectively, and $T_{1,2a}$ and $T_{1,2b}$ are the longitudinal and transverse relaxation times. $\omega_1 = \gamma B_1$ is the RF saturation pulse amplitude, and $\Delta\omega_{a,b}$ is the difference between the saturation RF offset and the bulk water and labile proton chemical shifts, respectively.

More complicated mathematical models, including three-pool models (Woessner et al., 2005), that include magnetization transfer from semi-solid macromolecules through dipole-dipole interaction

(with a very short $T_2$), and four or higher pool models (Li, Alex X. et al., 2008), have also been reported, that include additional exchangeable proton and/or semi-solid proton pools.

The Bloch-McConnell equation can be extended to describe multi-pool (n-pool) CEST signal as follows (Sun, 2010b, Woessner et al., 2005, Zhou, Jinyuan et al., 2004):

$$\begin{bmatrix} \partial M_{ax}/\partial t \\ \partial M_{ay}/\partial t \\ \partial M_{az}/\partial t \\ . \\ . \\ . \\ \partial M_{b_{n-1}x}/\partial t \\ \partial M_{b_{n-1}y}/\partial t \\ \partial M_{b_{n-1}z}/\partial t \end{bmatrix} = \begin{bmatrix} -k_{ab_1} & \Delta\omega_a & 0 & . & 0 & 0 & k_{b_{n-1}a} & 0 & 0 \\ \Delta\omega_a & -k_{ab_1} & -\omega_1 & 0 & . & 0 & 0 & -k_{b_{n-1}a} & 0 \\ 0 & -\omega & -k_{ab_1} & 0 & 0 & . & 0 & 0 & k_{b_{n-1}a} \\ . & 0 & 0 & . & . & 0 & 0 & 0 & 0 \\ 0 & . & 0 & .. & . & -\omega_1 & 0 & 0 & 0 \\ 0 & 0 & . & 0 & -\omega_1 & . & 0 & 0 & 0 \\ -k_{ab_1} & 0 & 0 & 0 & 0 & 0 & -k_{b_{n-1}a} & \Delta\omega_{b_{n-1}} & 0 \\ 0 & -k_{ab_1} & 0 & 0 & 0 & 0 & \Delta\omega_{b_{n-1}} & -k_{b_{n-1}a} & -\omega_1 \\ 0 & 0 & -k_{ab_{n-1}} & 0 & 0 & 0 & 0 & 0 & -k_{b_{n-1}a} \end{bmatrix}$$

$$\begin{bmatrix} M_{ax} \\ M_{ay} \\ M_{az} \\ . \\ . \\ . \\ M_{b_{n-1}x} \\ M_{b_{n-1}y} \\ M_{b_{n-1}z} \end{bmatrix} - \begin{bmatrix} M_{ax}/T_{2a} \\ M_{ay}/T_{2a} \\ (M_{a0} - M_{az})/T_{1a} \\ . \\ . \\ . \\ M_{b_{n-1}x}/T_{2b_{n-1}} \\ M_{b_{n-1}y}/T_{2b_{n-1}} \\ (M_{b_{n-1}0} - M_{b_{n-1}0z})/T_{1b_{n-1}} \end{bmatrix} \quad \text{.....[2.20]}$$

While it is complicated and difficult to solve higher pool models, numerical (Murase & Tanki, 2011, Woessner et al., 2005) and analytic approaches (Bottomley et al., 1989, Zaiss et al., 2015) can be used to solve the Bloch-McConnell equations for models with a low umber of pools and investigate the effect of time varying saturation. This allows optimization of parameters to that increase the CEST effect.

### 2.2.5. CEST Spectrum (Z-Spectrum)

In CEST relative quantification is achieved by measuring the reduction in water signal caused by the saturation transfer, compared to the corresponding unsaturated image. A signal ($S_{sat}$) is measured after an RF pulse is applied at a desired offset frequency, $\Delta\omega$, from the water resonance. Another signal ($S_0$) is measured without applying a RF saturation pulse. The process is repeated over a range of saturation frequencies to generate the so-called CEST or Z-spectrum, which displays the ratio of water signal intensity acquired with and without saturation as a function of RF saturation frequency offset from free water at 0 ppm (Ward, K. M., Aletras & Balaban, 2000).

$$Z(\Delta\omega) = S_{sat}(\Delta\omega)/S_0 \quad \text{..... [2.21]}$$

A simple estimation of CEST the effect at a particular saturation frequency offset is complicated by competing factors like magnetization transfer (MT), which is transfer of magnetization between semi-solid macromolecules and water, and direct water saturation (DS) or spillover effects. These effects also reduce the water signal and should be eliminated for reliable CEST quantification.

To isolate the effects of chemical exchange from the effects of MT and DS, instead of comparing the signal reduction caused when saturating a specific spectral location ($+\omega_{ppm}$ with respect to) to that without saturation, the CEST effect is measured by comparing to the water signal reduction when saturating the opposite spectral location ($-\omega_{ppm}$). This asymmetry analysis assumes that the MT and DS effects are symmetrical about the water resonance frequency. In this way, the most commonly utilized CEST metric, the Magnetic Transfer Ratio ($MTR_{asym}$) at $+\omega_{ppm}$ is expressed as (Wu, B. et al., 2016, Zhou, J. et al., 2003, Zijl. & Yadav, 2011):

$$MTR_{asym} = \frac{(S_{sat}(-\Delta\omega) - S_{sat}(+\Delta\omega)}{S_0} \quad \text{..... [2.22]}$$

where $S_{sat}(+\Delta\omega)$ and $S_{sat}(-\Delta\omega)$ are the measured signal with RF saturation at $+\Delta\omega$ and $-\Delta\omega$, respectively.

$MTR_{asym}$ analysis assumes chemical-shift ($\Delta\omega$) > $k_{ba}$ – the transfer rate of protons from solute to water. Ideally, 3 measurements are required for $MTR_{asym}$: one each after applying an RF saturation pulse at $+\Delta\omega$ and $-\Delta\omega$, and another without applying RF saturation. However, in practice the assumption of symmetric MT and DS effects will be disrupted by $B_0$ inhomogeneity which will shift the resonance frequencies by an unknown amount.

Hence, instead of measuring signals at only 3 points, the CEST effect is measured by applying RF saturation pulses at a range of frequency offsets around the desired resonance frequencies both upfield and downfield of the water resonance frequency (0 ppm).

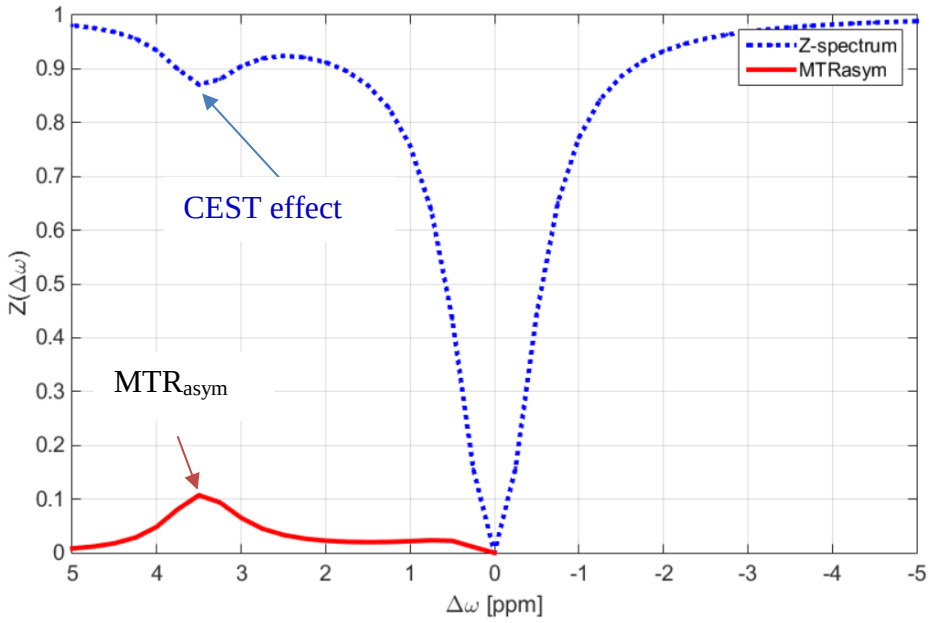


Figure 2.13: A simulated Z-spectrum and MTRasym curve. The simulation was based on an analytical solution to the two pool BM equation. A clear "suppression" in the Z-spectrum and "peak" in the $MTR_{asym}$ curve can be seen at 3.5 ppm corresponding to the CEST effect due to chemical exchange.

For molecules with resonance frequencies sufficiently far from water, the CEST effect may be visible as a "dip" or attenuation in the Z-spectrum and "peak" in the $MTR_{asym}$ curve as shown Figure 2.13. For molecules with resonance frequencies very close to water, like hydroxyl groups, the $MTR_{asym}$ plot is used to better visualize the CEST effect.

### 2.2.6. Other CEST metrics

***Bloch fitting***

The CEST spectrum can be fitted and quantified using the Bloch equations modified for chemical exchange (Li, Alex X. et al., 2008, Woessner et al., 2005). In this method, pools representing bulk water, solute molecule, and asymmetric magnetization transfer effects are typically fit to the measured CEST spectrum.

$$\text{CEST effect} = [S_a(\Delta\omega) - S_{a+\alpha}(\Delta\omega)]/S_0 \quad \ldots\ldots\ldots\ldots\ldots\ldots\ldots\ldots \text{[2.23]}$$

where $S_a$ and $S_{a+\alpha}$ are the simulated signals at $\Delta\omega$ offset frequency (chemical shift) of water pool and the water and desired molecule pool respectively. $S_0$ is the signal intensity of water without saturation. The pure CEST effect of the solute molecule can be measured from the fitted parameters. In theory this method removes the confounding effects of MT and direct water saturation.

***Lorentzian line fitting***

Analytical studies show that individual CEST effect, including the MT effect within a small range of frequency offsets, can be approximated by a Lorentzian line shape in a Z-spectrum (Zaiss, M. & Bachert, P., 2013, Zaiss, Schmitt & Bachert, 2011). The sum of these individual line shapes can provide a fit for complete CEST spectrum.

$$\text{Fitted CEST spectrum} = \sum L_i(\Delta w) \quad \ldots\ldots\ldots\ldots\ldots\ldots\ldots\ldots\ldots\ldots \text{[2.24]}$$

where Li is the Lorentzian function of a pool defined as (Kogan, Hariharan & Reddy, 2013):

$$L_i = A_i \frac{\frac{FWHM^2}{4}}{\frac{FWHM^2}{4} + (\Delta\omega - w(water))^2} \quad \ldots\ldots\ldots\ldots\ldots\ldots\ldots\ldots\ldots\ldots\ldots\ldots \text{[2.25]}$$

where *A* is the amplitude, *FWHM* is the full width half maximum, and *Δω* is the offset frequency of an individual Lorentzian function, *w(water)* is the frequency of bulk water.

This method allows fitting of multiple pools with Lorentzian line shapes. However, the reliability of this approach strongly depends on the SNR, which can be compromised by poor spatio-temporal resolution. In addition, conventional least-squares fitting is sensitive to initial and boundary values, which, if not properly selected can lead to inaccurate fitting (Zhou, Iris Yuwen et al., 2017).

***Relaxation compensated CEST MRI (AREX)***

AREX is another method of correcting the direct water saturation and MT influences (Zaiss et al., 2014), which is based on an inverse metric of the steady-state Z-spectra. To correct for MT and DS effects, a reference spectrum ($Z_{ref}$) is subtracted from the complete fit of the CEST spectrum ($Z_{lab}$). $Z_{ref}$ consists of the fit for all pools except the pool of interest in the CEST spectrum. This subtraction is assumed to yield an isolated CEST effect known as $MTR_{Rex}$.

$$MTR_{Rex} = 1/Z_{lab} - 1/Z_{ref} \quad \text{..... [2.26]}$$

After this subtraction, the influence of water longitudinal relaxation is corrected via multiplication by $R_{1w}$ ($1/T_{1w}$). This provides relaxation compensated CEST signal known as apparent exchange-dependent relaxation (AREX) (Xu et al., 2014, Zaiss et al., 2014).

$$AREX = MTRRex/T1 \quad \text{..... [2.27]}$$

$MTR_{Rex}$ and AREX are metrics for pH measurement, where exchange rate is a function of pH. However they should be used with caution as the statistical error of inverse Z is considerably higher than Z which may limit the application of $MTR_{Rex}$ and AREX, especially for exchange protons with a small chemical shift such as -OH protons in glycogen (Michael T. McMahon, 2017).

### 2.2.7. CEST pulse sequence implementation

The CEST MRI pulse sequence consists of three parts: a relaxation period that allows sufficient magnetization recovery prior to the next excitation; a saturation pulse that determines the type of image contrast and molecule to be detected, and image acquisition, which determines the image quality and scan time (Figure 2.14). There are two main approaches for RF saturation: continuous wave (CW) and pulsed wave (PW). Other types of CEST preparations have also been proposed such as frequency-labeled exchange transfer (FLEX) (Friedman et al., 2010, Lin, C. Y. et al., 2014, Lin et al., 2012, Wu, B. et al., 2016), saturation with frequency alternating RF irradiation (SAFARI) (Scheidegger, Vinogradov & Alsop, 2011), or spin-lock (Jin & Kim, 2014, Yuan et al., 2012, Zaiss, Moritz & Bachert, Peter, 2013).

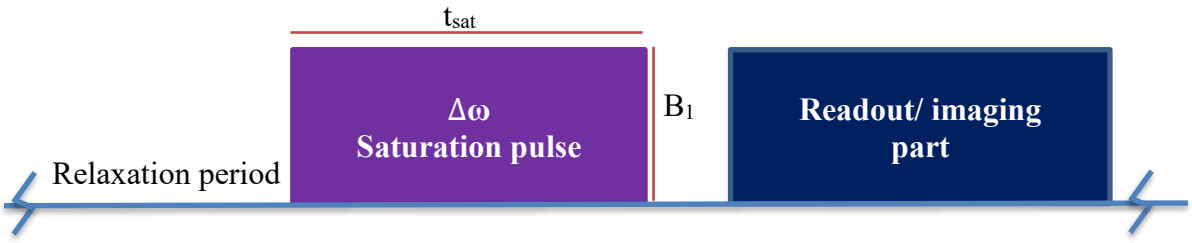


Figure 2.14: Parts of CEST pulse sequence

### *CW saturation pulse*

In this approach, a continuous off-resonance RF pulse, with a given amplitude, duration and frequency, is used for saturation. Optimization is straightforward in the CW-CEST case, because there is an analytic solution that facilitates simple and rapid calculation (Zu et al., 2011), and there are only two acquisition parameters (amplitude and duration) that need to be optimized. Experiments using CW are less sensitive to $B_1$ inhomogeneities, but have high power deposition (high SAR), that may pose a safety issue, especially at high field strengths (Wu, B. et al., 2016). Figure 2.15 shows the timing diagram of a ss-EPI sequence with a CW RF saturation pulse.

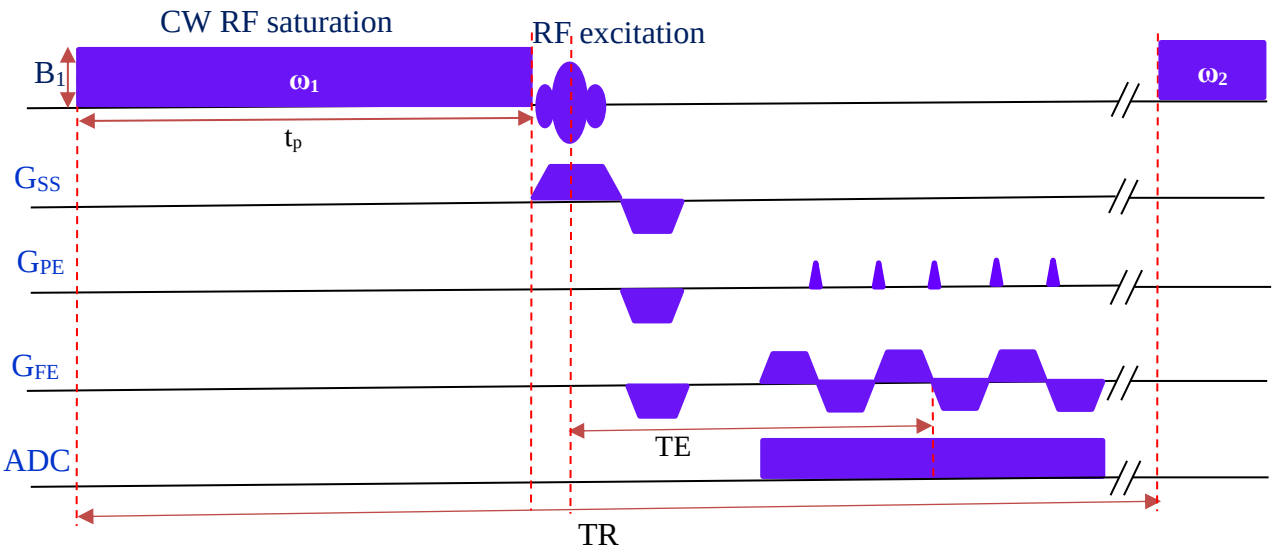


Figure 2.15: CW RF saturation pulse with amplitude (power), $B_1$ and duration $t_p$ with a GRE-EPI acquisition. TR includes both the saturation duration, acquisition duration and relaxation duration (shown broken, a time where spins are allowed to relax to their equilibrium position and be ready for next saturation and measurement with a different offset frequency) in a single measurement.

### *PW saturation pulse*

In the PW implementation, a train of short RF pulses are used with a total duration equivalent to the CW pulse (Figure 2.16). Using short repetitive pulse addresses the SAR limitation. In pulsed saturation, more sophisticated RF shapes have been proposed such as Fermi (Dixon et al., 2010),

Sinc and Gaussian (Schmitt et al., 2011, Zu et al., 2011) etc. In addition to the pulse shape, factors that need to be considered CEST signal optimization include: individual pulse length, inter-pulse gap, and number of pulses (Wu, B. et al., 2016) making it more difficult to use analytical optimization. PW saturation is sensitive to field inhomogeneities (Schneider, Prost & Glover, 1993).

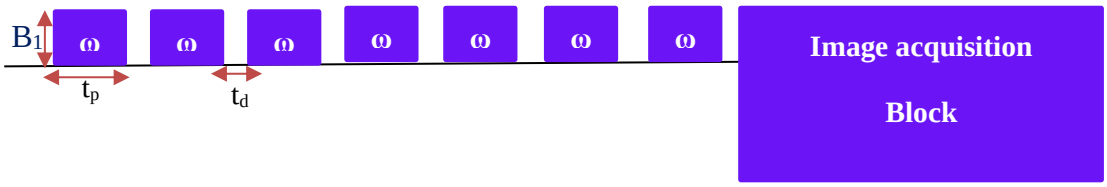


Figure 2.16: PW saturation pulse with power $B_1$, individual pulse duration $t_p$ and inter pulse gap $t_d$. The TR duration includes pulse duration, inter-pulse gap, acquisition time and relaxation duration.

## 2.3. Glycogen detection using CEST (glycoCEST) MRI

When we eat carbohydrates, our body breaks them down into smaller sugars (glucose, fructose, and galactose) which get absorbed and used as energy. Any glucose not needed right away gets stored mainly in the muscles and the liver in the form of glycogen. When glycogen stores are filled up, the extra will be stored as fat (Acheson et al., 1988).

Glycogen is a branched glucose polymer consisting of linear α-1,4 linkages and branching α-1,6 linkages. It is the primary short-term energy storage molecule in animals and bacteria (Iwase et al., 2018, Roach et al., 2012). Glycogen can be easily stored by our muscles (~500 g) and liver (~100 g) hydrated with three or four parts of water (Jensen et al., 2011, Kreitzman, Coxon & Szaz, 1992).

Muscle glycogen is converted into glucose by muscle cells and used as the primary 'fuel' during exercise., and liver glycogen converts to glucose for use throughout the body including the central nervous system (Katz et al., 1986). Glycogen is essential for energy production at all levels of effort and plays a major role in supporting the energy demands of skeletal muscle during prolonged exercise. At rest, muscle glycogen is used for about 15-20% of energy production. At moderate

intensities (~55-60% of max) glycogen usage could rise to as much as 80-85%, and this increases even more at higher exercise intensities (Kreitzman, Coxon & Szaz, 1992).

Literature shows that aerobic endurance is directly related to the initial store of muscle glycogen, that strenuous exercise cannot be maintained once these stores are depleted, and that perception of fatigue during prolonged intense exercise parallels the decline in muscle glycogen (Bergstrom et al., 1967, Hermansen, Hultman & Saltin, 1967, Ivy, 2004). During exercise, when the body runs out of glycogen, it experiences a very uncomfortable state and lacks the energy to continue exercising. For sustained intense exercise, or for rapid recovery from prolonged exercise, it is important to refill muscle glycogen stores and initiate repair and adaptation, by consuming either carbohydrate high food or glycogen gels (Ivy, 2004, Saitoh et al., 1994).

Several genetic glycogen storage diseases are characterized by an abnormal ability to utilize glycogen (Godfrey & Quinlivan, 2016, Wolfsdorf & Weinstein, 2003) that results in exercise intolerance, and glycogen content may also be abnormal in conditions such as obesity, insulin resistance, and type 2 diabetes (Cline et al., 1999, Zijl. et al., 2007).

Methods to detect and quantify glycogen *in vivo* are key for better understanding of exercise-related glycogen depletion and repletion to optimize athletic performance and in the prescription of exercise and dietary interventions for health, fitness and weight control as well as to understand the pathophysiology of glycogen related disease.

Despite limitations of the methods, glycogen can be measured by invasive tissue sampling through needle biopsy(Bergstrom, 1975, Evans, Phinney & Young, 1982, Shanely et al., 2014), $^{13}C$ Magnetic Resonance Spectroscopy ($^{13}C$ MRS) (Lei et al., 2007, Witney et al., 2014), Positron Emission Tomography (PET) (Witney et al., 2014) or high frequency ultrasound (Nieman et al., 2015, Sikdar, Wei & Cortes, 2014).

Needle biopsy provides direct glycogen measurement but is invasive and impractical for longitudinal studies due to discomfort associated with repeated biopsies from different muscle groups.

$^{13}C$ MRS can provide a direct measurement of glycogen concentration in various organs, but is not widely available. In addition to poor spatial resolution, PET involves ionizing radiation, which

limits the allowable frequency of measurement, making it unsuitable for longitudinal studies. Low spatial resolution and accuracy limit the use of ultrasound for detection of glycogen.

What makes MRI a very powerful technique compared to other imaging modalities is the ability to generate new contrasts by manipulation of hydrogen atoms in different molecules. The major difference between CEST MRI and other MRI pulse sequences is that CEST requires a train of spectrally selective CEST excitation pulses before the standard excitation pulse. These saturation pulses saturate the magnetization of the hydrogen nuclei attached to the hydroxyl (OH-) group in glycogen. Since hydrogen nuclei bound to glycogen and those in free water possess different chemical shifts, after spectrally selective saturation of the hydrogen nuclei in the glycogen pool an attenuated MRI signal can be detected in the water pool due to chemical exchange between the two pools.

The feasibility of detecting glycogen using CEST from –OH groups of glycogen to free water (glycoCEST) was previously demonstrated *in vivo* (Zijl. et al., 2007) (Kim, Mina et al., 2009). However, to date, CEST MRI is not routinely available on clinical scanners. The rapid exchange of -OH protons (which is greater than $10^3$ per second (Zijl. et al., 2007)), a small chemical shift difference with bulk water protons (0.5 – 1.5 ppm), the dependency of chemical shift as well as exchange rate on the MRI magnetic field, temperature and pH (Sun, van Zijl & Zhou, 2005) makes the detection of glycogen/hydroxyl proton groups using CEST MRI a difficult task.

The acquisition of multiple CEST images to generate the Z-spectrum results in long scan times when using traditional imaging readouts. This long scan time causes CEST MRI to be susceptible to subject motion and magnetic field inhomogeneity. To decrease the overall acquisition time, rapid MRI acquisition techniques have been adapted for CEST, including Rapid Acquisition with Relaxation Enhancement (RARE) (Liu et al., 2009), Echo Planar Imaging (Liepinsh & Otting, 1996, Sun et al., 2013), True Fast Imaging with Steady State Free Precession (FISP) (Shah et al., 2011), Gradient and Spin Echo (GRASE)(He Zhu, 2010), Variably-accelerated Sensitivity Encoding (vSENSE) (Zhang et al., 2017), keyhole (G., E. & E., 2012), as well as optimized spiral-centric-reordered GRE approaches (Zaiss, Ehses & Scheffler, 2018). These imaging methods, however, cannot eliminate motion and fluctuation in the prepared static shim between different offset frequency acquisitions.

## 2.4. Motion in MRI and correction techniques

Most MRI imaging sequences require an acquisition time that is far longer than the time scale of most types of physiological motions, including involuntary movements, cardiac and respiratory motion, gastrointestinal peristalsis, vessel pulsation and blood flow. These cause motion to occur in between or during acquisition blocks of the imaging sequence. Motion is one of the most frequent sources of artifacts in MRI. It causes the signal to be mis-registered during reconstruction and analysis and results in blurred images as well as ghosting (Ali et al., 2013, E. Mark Haacke et al., 1999). Motion induced effects in MR generally include: blurring artifacts due to interpolation (Tong & Cox, 1999), ghosting, signal loss, and the appearance of undesired strong signals (Zaitsev, Maxim, Maclaren & Herbst, 2015). Periodic motion synchronized with the *k*-space acquisition results in coherent ghosting with the number of replicas corresponding to the frequency of k-space modulation. Deviations from perfect periodicity in k-space result in incoherent ghosting, appearing as multiple overlapped replicas, and sometimes seen as stripes in the phase encoding direction (Zaitsev, Maxim, Maclaren & Herbst, 2015). Simple reconstruction using an inverse Fourier Transform (FT) assumes the object has remained stationary during the time the *k*-space data were sampled. Inconsistency between various portions of the *k*-space data causes readout-related motion artifacts (Zaitsev, Maxim, Maclaren & Herbst, 2015).

Motion in MRI can be categorized in to non-rigid and rigid motion. Non-rigid motion is hard to identify, it includes cardiac motion, gastrointestinal peristalsis, and pulsatile brain motion.

The influence of rigid body motion can be defined in the raw k-space data. Rigid body motion estimation and correction techniques in the inverse space operate by separating the translation and rotation of an object in a k-space. In general, translations only affect the phase while rotations only affect the magnitude of the raw signal (Vaillant et al., 2014).

The effect of rigid body transition on the phase of the signal is given by the Fourier shift theorem (Vaillant et al., 2014). Consider two physical representations of an object ($I_1(x, y)$, $I_2(x, y)$) translated by ($x_0$, $y_0$):

$$I_2(x, y) = I_1(x-x_0, y-y_0) \quad \text{[2.28]}$$

This translation in image space is converted to a linear phase accumulation between their corresponding Fourier pairs ($F_1(k_x, k_y)$, $F_2(k_x, k_y)$), referred to as Fourier-shift-theorem:

$$F_2(k_x, k_y) = F_1(k_x, k_y)\, e^{(-2j\pi (k_x x_0 + k_y y_0))} \quad \text{..... [2.29]}$$

The translation parameters ($x_0$, $y_0$) are encoded in the phase of the Fourier data and can be recovered by computing their normalized cross-power spectrum Q ($k_x$, $k_y$):

$$Q(k_x, k_x) = \frac{F_1(k_x,k_x)F_2^*(k_x,k_x)}{|F_1(k_x,k_x)F_2(k_x,k_x)|} \quad \text{..... [2.30]}$$

A straightforward operation to estimate ($x_0$, $y_0$) is to compute its inverse Fourier transform, leading to (Foroosh, Zerubia & Berthod, 2002, Vaillant et al., 2014)

$$p\,(x, y) = F^{-1}(Q\,(k_x, k_y)) = \delta\,(x - x_0, y - y_0) \quad \text{..... [2.31]}$$

where *p (x, y)* is referred to as the phase correlation map between the Fourier pairs $F_1(k_x, k_y)$ and $F_2(k_x, k_y)$. The $x_0$ and $y_0$ for which the cross correlation between F1 and F2 is maximum will be the estimated translations.

A rotation in object space is a rotation of the magnitude data in k-space around the central point in k-space (Hennig, 1999, Paschal & Morris, 2004, Tamhane & Arfanakis, 2009). The phase signal is not affected by rotations, apart from SNR changes due to the rotated magnitude. Estimation of the rotation of the object between two objects is equivalent to estimating the rotation in the data of the central k-space from two objects.

Since the beginning of clinical use of MRI, many techniques have been developed to prevent, suppress or correct subject motion artifacts.

The degree of motion can be minimized by simple instruction/education of the patient to stay still during a scan, or by using stabilization measures including the use of foam pads, supports, etc. Some unwanted physiological motions can be suppressed by using surface coils confined to the area of interest, or by using suppression/saturation pulses (Felmlee & Ehman, 1987) to null signals from unwanted moving anatomical objects (e.g. flow saturation pulses to suppress signals from arterial or venous blood entering a slice).

Adjusting imaging sequences and parameters is another way of reducing motion. Increasing the number of signals averaged reduce artifacts and increases SNR at the expense of imaging time. Swapping frequency- and phase encoding directions shifts the direction of artifacts (English &

Moore, 1995). Flow compensation techniques (Riek et al., 1993) can also reduce artifacts from flowing blood and spinal fluid by gradient refocusing of signal.

Motion detection and correction techniques in MRI can be grouped into two general categories: prospective and retrospective correction.

Many retrospective motion correction approaches assume that multiple images are available that can be registered to one another to determine the differences in position between them. This is applicable when the scan type naturally generates a series of image volumes, as in BOLD (fMRI). The images can be registered and resampled in post-processing to correct for some of the effects of motion. This approach has also been applied to diffusion (A.K. et al., 2016, Holdsworth et al., 2012, Kober, Gruetter & Krueger, 2012) and Arterial Spin Labeling (ASL) (Luh et al., 1999, Wang et al., 2008, Wu, W. C. et al., 2009) images, but this situation is more challenging because the images have different contrast and this will confound the motion estimation.

Prospective methods use motion-tracking data acquired during the scan to follow the subject by updating the slice positions. In prospective motion correction various methods are used to obtain pose information. Generally, they can be classified as optical methods, field methods and navigator methods.

External optical tracking devices are completely independent of the MR sequence timing. Laser systems, optical fibers or camera systems are used with the help of markers to track the patient movement (Chikop et al., 2018, H. et al., 1999, Herbst M, 2011, Maclaren et al., 2018, Todd et al., 2015, Zioga et al., 2012). These methods may not be appropriate as they require additional hardware which imposes patient discomfort and MRI issue of compatibility.

In field detection methods the scanner gradient fields are measured to localize the object. This technique requires the use of a short sequences of pulses to obtain position information from a small sample of MR visible material fixed inside a miniature receive coil (Ackerman JL, 1986, Dumoulin, Souza & Darrow, 1993). Field detection techniques require several probes or active markers to be attached to the subject. In this method, the active markers (and hence the subject) are connected to the scanner by wires. This makes patient handling more difficult and could increase patient anxiety levels. The presence of cables also increases difficulties with the rigid marker fixation (Maclaren et al., 2013).

MR navigator methods are the most common means of obtaining position information during an MRI experiment without using additional hardware. The pencil beam navigator (Ehman & Felmlee, 1989) was one of the first navigator technique used for motion correction. It was employed for the measurement of motion caused by breathing for thoracic and abdominal imaging. A line navigator was spliced into the imaging sequence to track the movement of the diaphragm. In this method the main purpose of the navigator is to track deformation or displacement of internal organs.

Advanced methods for rigid body motion have been devoped using navigator methods. Examples of navigator methods used for motion correction include navigators operating in k-space, such as orbital navigators (Fu et al., 1995), cloverleaf navigators (van der Kouwe, Benner & Dale, 2006), and spherical navigators (Welch et al., 2002) as well as image-based navigators, such as PROMO (White et al., 2010) or EPI navigators (Alhamud et al., 2012, Hess et al., 2011, Tisdall et al., 2012).

K-space navigators are used to repetitively sample parts of k-space and quantify rotations and translations of the object by measuring rotations and phase shifts in the k-space data. On the other hand, image base navigators (anatomical navigators) register the reconstructed magnitude image to a reference image to evaluate object translations and rotations. Navigator techniques with adequate accuracy for prospective motion correction all need unused time in the sequence to obtain accurate motion information. Navigator techniques have an advantage over hardware-based tracking and field detection methods, in that they require no additional hardware and that there is no need for a marker to be affixed to the subject. This is particularly important in terms of patient handling in clinical MRI.

## 2.5. Field inhomogeneity in MRI and correction techniques

MR uses three main magnetic fields: the main field ($B_0$), a radiofrequency field ($B_1$) and gradient fields. The measured MR signal depends greatly on the applied magnetic field magnitude and phases. Homogenous magnetic fields are required to create the most accurate images possible. However, a completely homogenous field is not feasible in the real world. In practice, it is not possible to build a perfect magnet. Inhomogeneity in the main field may arise both from the physical design of the magnet (although this can be improved with shimming) and from the differences in bulk magnetic susceptibility, especially on the boundary of air and tissues.

Under field inhomogeneity, the object to be imaged will have a distribution of different resonant frequencies which gives the spins phase incoherence. When the contribution from each spin is added together, this dephasing causes a signal loss. This effect is referred to as $T_2^*$ decay and causes a much faster decay in the transverse magnetization. This problem becomes even more severe and results in signal loss with longer readout times. If the $T_2^*$ decay is severe, the signal is weighted in k-space, creating blur in the final image. Geometric distortions can also result (Hong, Lee & Han, 2014, S. et al., 2004) in the image. An image is distorted due to field inhomogeneities created in two directions: distortion due to field inhomogeneities in the slice direction and distortion due to field inhomogeneities in plane of the slice.

Assuming a one-dimensional inhomogeneity along the slice-select direction and that the imaging gradient in this direction is centered at z= 0, in the presence of a local background field gradient **ΔB** treated as Gz', the slice select gradient will be (Reichenbach et al., 1997):

$$\mathbf{\Delta B} = G_z'(z).\,\mathbf{z} \quad \text{[2.32]}$$

$$\boldsymbol{\gamma}.\,(G_z + G_z')\,z' = \gamma G_z.\mathbf{z} \quad \text{[2.33]}$$

$$z' = \frac{Gz}{Gz+Gz'}.\mathbf{z} \quad \text{[2.34]}$$

where z' is the scaling factor.

Depending on Gz'>0 or Gz'<0, the slice thickness will be compressed or enlarges resulting on overall local intensity changes across the slice.

Another effect of gradient field distortion is improper refocusing of spins under the influence of the rephasing lobe of the slice-select gradient. The effect of field inhomogeneity in the slice-select direction on a signal received from a region of a sample can be expressed by looking the phase behavior. During the slice select process, the equation for the signal received from a region of a sample could be written as (E. Mark Haacke et al., 1999):

$$S(t) \propto \int \boldsymbol{\rho}(\boldsymbol{r}) e^{iG_z zt} dz \quad \text{[2.35]}$$

where **ρ(r)** is the spin density and $G_z$ the field gradient in the slice select direction.
since the measured signal is now affected by presence of field inhomogeneities in the slice select direction, G′z, misregistration of the signal occurs as a function of slice location:

$$S(t) \propto \int \boldsymbol{\rho}(\boldsymbol{r}) e^{i(G_z + G'z)zt} dz \ldots\ldots\ldots\ldots\ldots\ldots\ldots\ldots\ldots\ldots [2.36]$$

Similarly, field inhomogeneity also occurs in the plane of the slice causing image distortion and echo shift effects. Assuming readout direction in the x-direction, in the presence of field inhomogeneity, the actual readout gradient during sampling will become (G + $G_x$'), therefore the effective local field of will be scaled by the factor $\lambda$:

$$\lambda = \frac{G}{G + Gx'} \ldots\ldots\ldots\ldots\ldots\ldots\ldots\ldots\ldots\ldots\ldots\ldots [2.37]$$

Depending on the scaling factor **λ** the image information along this direction at the location of inhomogeneity either appears stretched (**λ<1,** FOV decreases locally) or shrunken (**λ>1,** FOV increases locally). The presence of **$G_x$'** causes wrong frequency encoding for a certain set of spins leading mispositioning upon reconstruction (Reichenbach et al., 1997).

The presence of **$G_x$'** will also cause an echo shift in time. The actual time at which all spins within a given voxel are rephased again, will be shifted away from the designated TE. Depending on the imaging conditions and polarity of the background gradients, the echo can be completely pushed outside the acquisition window, leading to a total signal loss (Reichenbach et al., 1997). The resulting effect of this temporal shift can be considered as an induced phase shift (Δϕ). Since the reconstruction is performed with the ideal TE taken as the origin in k-space, any temporal shift in the sampled time series leads to a phase shift during Fourier transformation.

$$\Delta\phi = 2\pi . \frac{\Delta TE}{n . \Delta t} \ldots\ldots\ldots\ldots\ldots\ldots\ldots\ldots\ldots\ldots\ldots\ldots [2.38]$$

where ΔTE is the temporal shift of the echo and n is the number of sampling points corresponding to a total sampling time per readout.

The same way, presence of local gradient along phase encoding direction will cause a net phase dispersion across the affected voxels resulting signal reduction. In addition, there will be a shearing distortion, shifting spin information from one voxel into other voxels (Bammer et al., 2005).

Field inhomogeneity rarely occurs in just one direction. The presence of field inhomogeneities along the x- and y- directions during the slice select process could cause the excited plane to be rotated (E. Mark Haacke et al., 1999). During the phase encoding process, slice distortion could occur resulting in positional misregistration of the signal. In trajectories, such as echo-planar, the

resulting geometric distortion due to field inhomogeneity is a shift. However, spiral trajectories cause a blur in the resulting image which is harder to correct for in the image domain (Jezzard & Clare, 1999, T-K. Truong, Chakeres & Schmalbrock., 2004), though both trajectories can be corrected in the signal domain.

The process of preventing magnetic field inhomogeneities (ΔB0) in MRI is called shimming. Shimming can be done passively or actively. In passive shimming**,** small pieces of sheet metal or ferromagnetic pellets are placed at various locations within the scanner bore to improve field homogeneity. On the other hand, active shimming technique uses currents directed through specialized coils to generate a "corrective" magnetic field. In both cases, the additional magnetic fields (produced by coils or steel) add to the overall magnetic field of the superconducting magnet increasing the homogeneity of the total magnetic field. Passive shimming is created for an empty magnet. But, when a subject is placed within the scanner bore, additional field distortions result from diamagnetic susceptibility effects. Each subject therefore creates a unique pattern of inhomogeneity that can only be corrected through a dynamic process. Hence, active shimming provides a method to correct for these individual field variations from subject to subject.

Shimming can be done through automatic shamming by the MR scanner in the beginning of the scan, although distortion by heating of the shim iron, subject motion and mechanical vibration may alter the field during the scanning procedure.

Several active shimming algorithms and techniques have been developed in MRI for different imaging sequences and applications using linear or higher-order resistive shim coil current updating (Alhamud et al., 2016, Balteau, Hutton & Weiskopf, 2010, Blamire AM, 1996, de Graaf et al., 2003, Gruetter, 1993, Hess et al., 2011, Lee, Jongho et al., 2009, Poole & Bowtell, 2008, Tisdall et al., 2012, Webb P, 1991, Wilson JL, 2002). The overall common goal of these techniques is to calculate the corrective shim currents to compensate for magnetic field fluctuation over a region of interest (ROI) by reducing the spatial standard deviation of the magnetic field. This includes updating zero-order, first-order and higher order shim coils. Zero-order (frequency offset) updating is done by RF frequency adjustment whereas first-order (linear gradient) adjustment is achieved by setting a constant offset to the linear spatial encoding gradients. The magnitude of each shim coil and frequency offset can either be calculated using $B_0$ field sensitive measurements of interactively by the operator. Acquiring a phase difference image (field map) (Reese, Davis &

Weisskoff, 1995) from complex division of images with different echo times and fitting the spatial shim terms to the $B_0$ field using linear regression is the most popular technique.

## 2.5. Motion and shim correction techniques in CEST MRI

CEST also suffers from the same problems as in MRI in general, in addition to its inherent difficulties. Subject motion during MR measurements is a major source of artefacts, and CEST is no exception. Subject motion is especially problematic in CEST data analysis as it relies on comparison of images acquired at multiple offset frequencies.

The acquisition of multiple CEST images results in long scan times when using traditional imaging readouts. This long scan time causes CEST MRI to be affected by motion. A CEST spectrum (also known as Z-spectrum) is generated for each acquired image voxel. If there is a mismatch between the corresponding voxels due to subject motion, the acquired Z-spectrum will not be accurate and high signal variations (peaks or dips) in the curve may be introduced, resembling detection of metabolites of interest.

The effect of motion and correction in CEST MRI is almost unexplored. The few studies that examine motion correction in CEST MRI are based either on rigid registration (Schuenke et al., 2017) or retrospective time domain analysis (Nirbhay N. Yadav, 2015). A recent similar work has included volumetric navigators to correct for motion in glutamate CEST at 7T (Auno, 2018). However, motion correction was only found to be effective for motion less than 0.7mm/0.7-degrees.

Moreover, since CEST is based on chemical shift, it is very sensitive to field inhomogeneity or fluctuation in the prepared shim. Shim fluctuations due to subject respiration, heating induced in the shim iron by eddy currents, mechanical vibrations or subject motion will affect CEST measurements.

In CEST, the irradiation RF pulses for label and reference scans are assumed to be symmetric around the free water resonance in the z-spectrum. However, in the presence of severe magnetic field inhomogeneity and motion, the label and reference scans will no longer be symmetric about the water resonance frequency, which will introduce a $B_0$ inhomogeneity-dependent MTR offset. Such an MTR offset, if not properly accounted for, may cause non-negligible errors in quantitative

CEST imaging. For OH protons that resonate close to water, the CEST effect can be observed only in the $MTR_{asym}$ plots. A shift in the Z-spectrum due to field inhomogeneity may result in either an intensity decrease or increase in the $MTR_{asym}$, misleading interpretation. Figure 2.17 is an example of artefactual $MTR_{asym}$ increase due to a Z-spectrum shift by 0.15 ppm down field of the water resonance frequency.

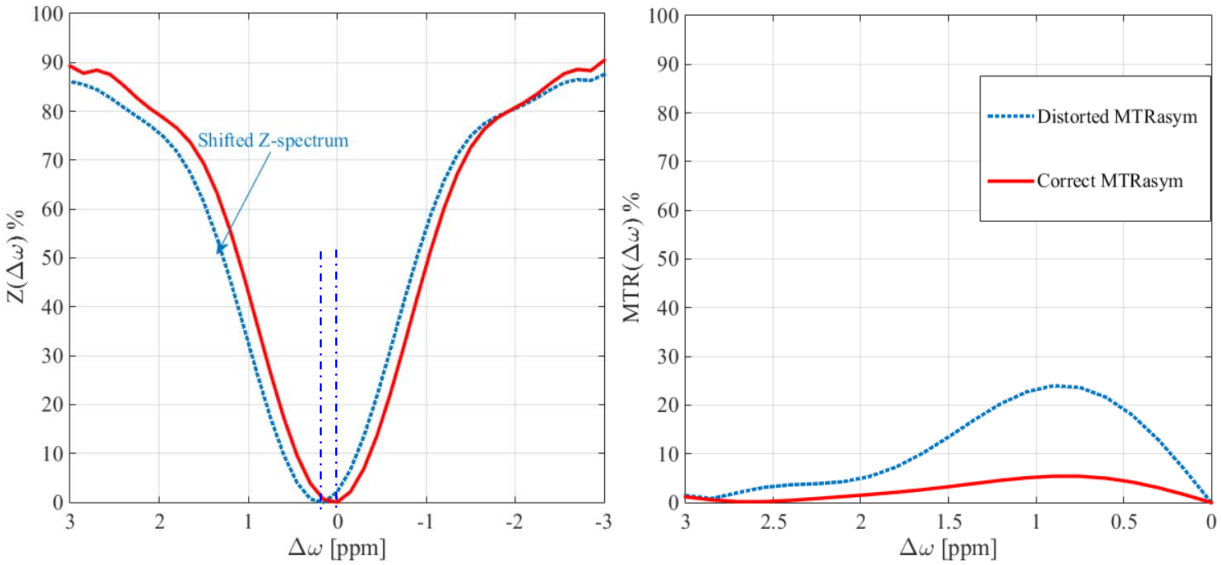


Figure 2.17: Simulated Z-spectra (left) and MTRasym plots (right). The dashed Z-spectrum is due to a shift of 0.15 ppm. A shift as small as 0.15 ppm in Z-spectrum causing relatively large changes in the MTRasym affecting the CEST quantification and misleading interpretation.

Current CEST $B_0$inhomogeneity-induced measurement error compensation techniques rely on post-processing of the CEST data using a pre-acquired $B_0$ map (Kim, Mina et al., 2009, Sun, Farrar & Sorensen, 2007), or fitting the CEST spectra to a higher-order polynomial (Zhou, Jinyuan et al., 2003, Zhou, J. et al., 2008). In the first method, the local $B_0$ shift at each voxel is determined from separately acquired gradient-echo phase images or using Water Saturation Shift Referencing (WASSR). WASSR uses a weak saturation pulse to measure the direct water saturation at each voxel (Kim, Mina et al., 2009). Assuming that maximal saturation occurs when the saturation offset equals the $B_0$ shift, the offset in the acquired CEST data is corrected, effectively moving the center of the Z-spectrum for each voxel back to 0 Hz. Alternatively, CEST spectra are fitted to a polynomial, where the minimum is deemed to be the reference frequency and each voxel's CEST spectrum is shifted accordingly (Zhou, Jinyuan et al., 2003, Zhou, J. et al., 2008). However, the robustness of this technique relies on sampling the minimum of the CEST spectra in sufficient

detail and the method is applicable only when the central peak in the Z-spectrum is sharp or if the CEST agents' exchangeable protons are sufficiently far from water that small errors in $B_0$ correction do not cause problems (i.e. MTC and DS effects are small).

The above methods of $B_0$ correction either require phase mapping using a separate pulse sequence, or an additional step for image registration and complicated curve fitting. Traditional curve fitting approaches are not suitable as a very long experiment time is required to collect the Z-spectrum with sufficiently fine frequency interval. Moreover, these post processing methods cannot remove errors that occur due to motion and field inhomogeneity between different offset scans.

Since in CEST MRI images are acquired with a longer time interval and varying contrast, it is advantageous to insert navigators with a consistent contrast independent of the CEST signal for the explicit purpose of measuring motion and shim. Such an approach has been used in diffusion (Alhamud et al., 2016), Single Voxel Spectroscopy (Hess et al., 2011), chemical shift imaging (Hess Aaron T., 2012) and GABA (Saleh et al., 2016). Navigators have the advantage of being able to measure changes in position by updating the slice positions and gradient coordinate system (Tisdall et al., 2012).

In this thesis, a method for real-time simultaneous measurement and correction of motion and field inhomogeneity, in terms of frequency (zeroth-order) and linear (first-order) shim gradients, in an optimized glycoCEST MRI sequence has been implemented using ultrafast double volumetric navigators (DvNavs).

# Chapter 3

## Chemical Exchange Saturation Transfer MRI optimal Continuous Wave RF irradiation parameters for glycogen (glycoCEST) detection[1]

Gizeaddis L. Simegn[2], Ali Alhamud[2,3], Frances Robertson[2,3], Ernesta Meintjes[2,3], and Andre van der Kouwe[2,4,5]

## Abstract

Chemical Exchange Saturation Transfer (CEST) enables detection of molecules such as glycogen, whose concentrations are too low to impact the signal intensity of standard MR imaging. Detection of these molecules is achieved by selectively saturating a molecule of interest and by measuring the reduction in water signal due to saturation transfer. CEST effects are dependent on parameters such as CEST agent concentration, pH, temperature, relaxation rate, magnetic field strength as well as on experimental parameters such as repetition time, RF irradiation amplitude and the imaging readout scheme. Measurement of molecules with exchangeable protons that resonate very close to water, e.g. hydroxyl groups in glycogen, is challenging especially at lower magnetic field strengths, mainly due to the effect of direct water saturation. Therefore, optimal RF irradiation parameters that maximize the CEST signal and reduce the competing factors are important for better quantification of glycogen-weighted CEST effects. In this study, analytical solution of the Bloch-McConnell equations was used to find optimal continuous wave RF irradiation parameters for detection of glycogen. *In vivo* tests were performed on a human calf muscle at different saturation powers to validate the optimal saturation parameters determined via simulation. The selected parameters were applied *in vitro* to CEST measurements in a phantom with varying glycogen concentrations and also *in vivo* in a human calf muscle. Our results show the possibility of detecting glycogen using CEST MRI at 3 T. It is further shown that glycoCEST signal can be

[1] Chapter written as an article intended for review and publication

[2] *UCT Medical Imaging Research Unit, Division of Biomedical Engineering, Department of Human Biology, University of Cape Town, Cape Town, South Africa*
[3] *Cape Universities Body Imaging Centre (CUBIC-UCT), Cape Town, South Africa*
[4] *Athinoula A. Martinos Center for Biomedical imaging/MGH, Charlestown, MA, United States*
[5] *Department of Radiology, Harvard Medical School, Boston, MA, United States*

maximized by optimizing the RF pulse irradiation parameters and that different glycogen concentrations can be identified when applying the optimized saturation pulse.

**Keywords:** chemical exchange saturation transfer, CEST, glycogen, glycoCEST, RF irradiation power, $B_1$, RF irradiation duration

## 3.1. Introduction

Glycogen plays a major role in supporting the energy demands of skeletal muscle during prolonged exercise. Depletion of muscle glycogen affects exercise performance; however, repletion and depletion are poorly quantified. Currently glycogen can be measured by invasive tissue sampling through needle biopsy, Positron Emission Tomography (PET) which uses ionizing radiation and $^{13}C$ magnetic resonance spectroscopy (MRS). Due to the numerous practical disadvantages of measuring glycogen in humans by tissue biopsy and using ionizing radiation, there has been widespread interest in detection of glycogen *in vivo* by $^{13}C$ MRS in multiple organs, including the heart (Bottomley et al., 1989), liver (Magnusson et al., 1992), skeletal muscle (Cline et al., 1999), and brain (Oz et al., 2003). With MRS methods, a wide dynamic range of glycogen levels has been observed. However, $^{13}C$ MRS is available only in specialized research sites and require costly hardware upgrades and $^{13}C$ isotopes, not routinely available on clinical MRI scanners (Zijl. et al., 2007). The ability to measure glycogen in different organs non-invasively using standard MRI hardware would be helpful for a wide variety of applications.

Chemical Exchange dependent Saturation Transfer (CEST) MRI, is a recent MRI contrast method that can detect macromolecules, including glycogen, from the nanomolar to millimolar range. Since hydrogen nuclei bound to different molecules and those in free water possess different chemical shifts (i.e., resonance frequencies), MRI methods to probe these exchange processes, make use of a spectrally selective excitation of the nuclei in one pool and detection of the attenuated MRI signal in the other pool (bulk water). The exchange of protons between the two pools results in unique contrasts that can be used to quantitatively assess physiological exchange processes, including Amide Proton Transfer (APT) (Zhou, Jinyuan et al., 2003), Glycosaminoglycan (GAGCEST) (Ling et al., 2008) and Glutamate and γ-aminobutyric acid (GABA) (Cai et al., 2012). This also introduces the possibility for indirect detection of glycogen via the MRI water resonance, by exploiting chemical exchange between the hydroxyl (-OH)

protons and free water. The feasibility of detecting glycogen using CEST (glycoCEST) has previously been demonstrated *in vivo* in animal studies of the liver at 4.7 T (Zijl. et al., 2007). Detection of skeletal muscle glycogen has also been performed at 3 T in different muscle groups using CEST MRI in conjunction with the Water Saturation Shift Referencing (WASSR) frequency correction method (Kim, Mina et al., 2009).

To generate CEST signal, a magnetization preparation pulse is embedded in the pulse sequence. One of two RF pulse types can be used to perform the saturation: continous wave (CW) or pulsed wave (PW). In CW-CEST a long rectangular RF pulse is used to saturate the metabolite protons whereas in pulsed-CEST multiple pulses with short duration are applied (Liu., 2008.). The specific absorption rate (SAR) and hardware limitations deterrmines the choice of pulse type (Vinogradov, Sherry & Lenkinski, 2013). Although PW saturation helps to reduce the burden on the hardware as well as the SAR level, in pracice the optimization of the PW RF pulse is often performed experimentally (Wu, B. et al., 2016). The CW RF pulse type is widely used for its simplicity and ease of optimization, although sequence parameters including saturation irradiation pulse design and readout RF pulse type and duration require consideration (Huang et al., 2015).

The CEST effect is sensitive to solute proton concentration and exchange rate and also to factors that affect the exchange rateincluding pH and temperature. However, CEST signal also depends on relaxation rate and magnetic field strength (Kim, Jinsuh et al., 2015). It has been shown that the apparent CEST measurement varies strongly with experimental parameters such as the RF irradiation amplitude (B1) and duration (Jiang et al., 2016, Kim, Jinsuh et al., 2015). Generally, fast exchanging hydrogen protons (as in glucose and glycogen) are expected to produce good CEST signal only when saturated with high RF power, whereas slower exchanging molecules (like amide groups) require less power. However, SNR also gets affected at high saturation power levels.

Magnetization transfer (MT ) - transfer of magnetization between semi-solid macromolecules and water, and the direct water saturation (DS) or spillover effect (Wu, B. et al., 2016) also affect the CEST signal depending on the RF irradiation level. The spillover effect dominates, reducing the observable signal especially close to water (Michael T. McMahon, 2017). Moreover, strong spillover effects shift the magnetic transfer ratio (MTR) asymmetry profile away from water at the center. Hence, the optimum range of offset frequencies that contain the CEST information depends

on the applied saturation power. Precise optimization of saturation power depends on the characteristics of the tissue inspected, including water content, T1 and T2 relaxation times, and pH. Recent studies have also shown that the CEST effect depends on experimental factors such as repetition time (TR) and flip angle (FA) (Sun et al., 2013), which also need to be taken into account. For small molecule contrast agents that have a chemical shift very close to the water resonance frequency, like -OH molecules in glycogen, the CEST effect is very sensitive to parameter selection, and choosing the saturation parameters that maximize the signal is crucial. Previous studies have used a continuous-wave rectangular RF saturation pulse with a B1 field strength of 3 μT and duration 300 ms to detect glycogen in the liver (Deng et al., 2016b) and a B1 field strength of 0.75 μT, duration 500 ms for skeletal muscle (Kim, Mina et al., 2009). Although the optimal RF power and duration have not been systematically determined, they are likely to differ between tissues due to differences in T1, T2 and water content.

Different approaches have been used to optimize the amplitude of RF pulses that maximize CEST signal (Sun, 2010a, Zhe Sun et al., 2008). Both analytical and numerical mathematical models have been developed to describe the CEST signal mechanism. However, numerical methods are computationally complex, the insight into the intrinsic structure of Z-spectra is limited, and no analytical optimization for designing experiments is possible.

Despite its broad range of potential applications (Jin et al., 2014, Ling et al., 2008, Nasrallah et al., 2013, Sun & Sorensen, 2008, Ward, K. M., Aletras & Balaban, 2000, Zhou, Jinyuan et al., 2003, Zhou, J. et al., 2008), CEST MRI lacks a standard as to which RF pulse type, duration and power, and pulse sequence to use for a specific molecule of interest at a particular magnetic field strength, limiting its use for routine clinical applications. In this study analytical solution of the Bloch-McConell (BM) equations was used to analyze the dependence of the glycoCEST effect on CW RF irradiation parameters and to select optimal values that maximize the proton transfer ratio using a 2D single-shot gradient echo EPI sequence at 3 T. This is then validated *in vivo* and demonstrated on a glycogen phantom.

## 3.2. Theory

### 3.2.1. Bloch–McConnell (BM) equations

The Bloch-McConnell equations are two sets of Bloch equations modified with exchange terms between the solute and free water protons, that are commonly used to describe proton transfer experiments. Even though the general solution for a broad range of irradiation parameters is complicated, concise results can be derived under certain assumptions (Sun, van Zijl & Zhou, 2005). For a typical 2-pool chemical exchange model, comprising pool *a* (the water pool) and pool *b* (the dilute solute pool, glycogen in this case), with forward (a → b) exchange rate $k_a$ and thermal equilibrium magnetizations $M_{0,a}$ and $M_{0,b}$, in a static magnetic field $B_0 = (0, 0, B_0)$, the ratio $M_{0,b}/M_{0,a}$ is conserved by the backward (b → a) exchange rate $k_a$ ($M_{0,b}/M_{0,}$= fb/kb . Pool a is the measured pool, which is the spin ensemble of water protons.

On resonance, the RF irradiation field $B_1 = (B_1,0, 0)$ causes the magnetization to precess around the x-axis in the rotating frame, with frequency $\omega_1 = \gamma B_1$. For off-resonance irradiation, the magnetization rotates around the effective field $B_{eff} = (\omega_1, 0, \Delta\omega)/\gamma = \omega_{eff}/\gamma$ at an angle $\theta = \tan^{-1}(\omega_1/\Delta\omega)$ from the z-axis. The dynamics of magnetizations of the two pools during off-resonance irradiation is described by the BM equations for the case of exchange between pool *a* and *b* and by the differential equations for dipolar–coupled systems (Henkelman et al., 1993). In the rotating frame of reference (x, y, z), the time dependent BM equations for two pools, water (pool a), CEST (pool b) are (Murase & Tanki, 2011, Woessner et al., 2005):

$$\frac{dM_{xa}}{dt} = \Delta\omega_a M_{ya}(t) - R_{2a}M_{xa}(t) - k_a M_{xa}(t) + k_b M_{xb}(t)$$

$$\frac{dM_{xb}}{dt} = \Delta\omega_b M_{yb}(t) - R_{2b}M_{xb}(t) - k_b M_{xb}(t) + k_a M_{xa}(t)$$

$$\frac{dM_{ya}}{dt} = -\Delta\omega_a M_{xa}(t) - R_{2a}M_{ya}(t) - k_a M_{ya}(t) + k_b M_{yb}(t) + \omega_1 M_{za}(t) \quad \text{..... [3.1]}$$

$$\frac{dM_{yb}}{dt} = -\Delta\omega_b M_{xb}(t) - R_{2b}M_{yb}(t) - k_a M_{ya}(t) + k_a M_{ya}(t) + \omega_1 M_{zb}(t)$$

$$\frac{dM_{za}}{dt} = \omega_1 M_{ya}(t) - R_{1a}[M_{za}(t) - M_{0a}] - k_a M_{za}(t) + k_b M_{zb}(t)$$

$$\frac{dM_{zb}}{dt} = \omega_1 M_{yb}(t) - R_{1b}[M_{zb}(t) - M_{0b}] - k_b M_{zb}(t) + k_a M_{za}(t)$$

The differential equations given by Equation [3.1] above can be combined into one vector equation as follows (Zaiss, M. & Bachert, P., 2013):

$$\frac{d}{dt}\vec{M} = A \cdot \vec{M} + \vec{C} \quad \text{..... [ 3.2]}$$

with the six-dimensional magnetization vector M

$$\vec{\mathrm{M}} = \begin{pmatrix} \mathrm{M_{xa}} \\ \mathrm{M_{ya}} \\ \mathrm{M_{za}} \\ \mathrm{M_{xb}} \\ \mathrm{M_{yb}} \\ \mathrm{M_{zb}} \end{pmatrix} \quad \text{..... [3.3]}$$

And a block matrix A:

$$A = \begin{bmatrix} L_a - K_a & +K_b \\ +K_a & L_b - K_b \end{bmatrix} \quad \text{..... [3.4]}$$

consisting of 3x3 submatrices $K_i = k_i \cdot I$, and $L_i$ where i = a, b

$$L_i = \begin{pmatrix} -R_{2i} & -\Delta\omega_i & 0 \\ +\Delta\omega_i & -R_{2i} & +\omega_1 \\ 0 & -\omega_1 & -R_{1i} \end{pmatrix} \text{..... [3.5]}$$

And the constant vector C:

$$\vec{\mathrm{C}} = \begin{pmatrix} 0 \\ 0 \\ \mathrm{R_{1a}M_{0a}} \\ 0 \\ 0 \\ \mathrm{R_{1b}M_{0b}} \end{pmatrix} \text{..... [3.6]}$$

$\Delta\omega_a = \omega_{rf} - \omega_a$ is the frequency of the oscillating $B_1$ field ($\omega_{rf}$) offset relative to the Larmor frequency $\omega_a$ of pool a (for $^1$H: $\omega_a/B_0 = \gamma = 42.58$ Hz/$\mu$T). The offset of pool b: $\Delta\omega_b = \omega_{rf} - \omega_b = \Delta\omega_a - \delta_b\omega_a$, is shifted by $\delta_b$ parts per million (ppm) relative to the water proton resonance. $R_{1,a/b} = 1/T_{1,a/b}$ and $R_{2,a/b} = 1/T_{2,a/b}$ are longitudinal and transverse relaxation rates.

The exchange rate from free water to solute protons ($K_a$) can be calculated from the following relationship based on the mass balance between two pools (Zaiss, M. & Bachert, P., 2013)

$$K_a = f_b K_b = f_b \begin{pmatrix} k_b & 0 & 0 \\ 0 & k_b & 0 \\ 0 & 0 & k_b \end{pmatrix} \text{..... [3.7]}$$

$$f_b = \frac{M_{0b}}{M_{0a}} = \frac{n_b \cdot [b]}{n_a \cdot [a]} \text{..... [3.8]}$$

Where $f_b$ is the proton fraction, [a] and [b] are the concentrations and $n_a$ and $n_b$ are the number of protons per molecule for pools a and b. The population fraction $f_b$ can be assumed to be < 1 %, hence $k_{ab} << k_{ba}$ (Zaiss, M. & Bachert, P., 2013).

For n-pools the system of equations [3.1-3.4] increases in dimensionality. E.g. for three pools, pool c for semi-solid macromolecular protons, Equation [3.4] transforms to (Zaiss, Moritz & Bachert, Peter, 2013)

$$A = \begin{bmatrix} L_a - K_{ab} & +K_{ba} & +K_{ca} & +K_{da} & +K_{fa} \\ +K_{ab} & L_b - K_{ba} & 0 & 0 & 0 \\ +K_{ac} & 0 & L_c - K_{ca} & 0 & 0 \\ +K_{ad} & 0 & 0 & L_d - K_{da} & 0 \\ +K_{ae} & 0 & 0 & 0 & L_e - K_{ea} \end{bmatrix} \text{..... [3.9]}$$

### 3.2.2. Solution of The Bloch–McConnell Equations

The BM equations are first–order ordinary differential equations with an inhomogeneous term (Equation [3.2]). The formal solution of the BM equations that is commonly used for numerical solution is (Murase & Tanki, 2011):

$$\vec{M} = (\vec{M}_0 + A^{-1}\vec{C})\exp(A \cdot t_{sat}) - A^{-1}\vec{C} \text{..... [3.10]}$$

However, this method is computationally complex and does not allow analytical optimization for designing experiments.

The CEST effect is usually analyzed using Magnetic Transfer Ratio asymmetry ($MTR_{asym}$) obtained from Z-spectra (CEST spectra) plotted as a function of RF irradiation frequency (Murase

& Tanki, 2011, Sun, van Zijl & Zhou, 2005). The Z value after long irradiation at an RF frequency offset $\Delta\omega$ is given by the z component of the water (pool a) magnetization $(M_{za}(\Delta\omega))$ normalized by the equilibrium magnetization ($M_{0a}$) without RF saturation:

$$Z(\Delta\omega) = \frac{M_{za}(\Delta\omega_a)}{M_{0a}} \quad \text{[3.11]}$$

The proton transfer ratio that excludes effects of direct water saturation and semi-solid macromolecular magnetization transfer (MT) can be analyzed via Z-spectrum asymmetry obtained from saturation of corresponding frequencies +Δω and -Δω either side of the water resonance, as follows (Murase & Tanki, 2011, Sun, van Zijl & Zhou, 2005):

$$MTR_{asym} = \frac{M_{za}(-\Delta\omega_a) - M_{za}(\Delta\omega_a)}{M_{0a}} = Z(-\Delta\omega) - Z(+\Delta\omega) \quad \text{[3.12]}$$

Using an Eigenspace solution to the Bloch-McConnell equation for two pools, Equation [3.11] can be formulated as:

$$Z(\Delta\omega) = \frac{\cos^2\theta . R_{1a}}{R_{1p}(\Delta\omega_a)} \quad \text{[3.13]}$$

For two pools, the longitudinal relaxation in the rotating frame $R_{1p}$ is a superposition of water relaxation $R_{eff}$ and exchange dependant relaxation (CEST) $R_{cest}$ (Sun, van Zijl & Zhou, 2005, Zaiss, Moritz & Bachert, Peter, 2013, Zaiss et al., 2015):

$$R_{1p}(\Delta\omega) = \underbrace{(R_{1a}\cos^2\theta + R_{2a}\sin^2\theta)}_{R_{eff}} + \underbrace{(f_b\, k_{ba} . \frac{{\omega_1}^2}{{\omega_1}^2 + k_{ba}(k_{ba} + R_{2a})})}_{R_{cest}} \quad \text{[3.14]}$$

where

$$\sin^2\theta = \frac{{\omega_1}^2}{({\omega_1}^2 + \Delta\omega^2)}; \cos^2\theta = \frac{\Delta\omega^2}{({\omega_1}^2 + \Delta\omega^2)} \quad \text{[3.15]}$$

For three pools (water, CEST and MT) if $fb_{,fc} << 1$, the longitudinal relaxation $R_{1p}$ can be described as follows (Zaiss, Moritz & Bachert, Peter, 2013, Zaiss et al., 2015):

$$R_{1p}(\Delta\omega) = R_{eff}(\Delta\omega)(\Delta\omega) + R_{mt}(\Delta\omega) + R_{cest} \quad \text{[3.16]}$$

where the MT relaxation rate $R_{mt}$ in rotating frame is:

$$R_{mt}(\Delta\omega) = \frac{(\Delta\omega_1{}^2 + r_{2a}{}^2).(k_{ca}r_{1a} + r_{1c}(k_{ac}+r_{1a})) + \omega_1{}^2.r_{2a}.(k_{ca}+r_{1c})}{(\Delta\omega_1{}^2 + r_{2a}{}^2).(k_{ca}+k_{ac}+r_{1a}+r_{1c}) + 2.r_{2a}.(k_{ca}r_{1a} + r_{1c}(k_{ac}+r_{1a})) + \omega_1{}^2.(k_{ca}+r_{2a}+r_{1c})} \quad \ldots [3.17]$$

and $r_{1a} = R_{1a} - R_{eff}$, $r_{2a} = R_{2a} - R_{eff}$, and $r_{1c} = R_{1c} + R_{1s} - R_{eff}$

Zaiss et al (Zaiss et al., 2015) show that considering the effect of semi-solid MT pool *c* on $T_1$ recovery time, the relaxation rate $R_{1a}$ in Equation [3.13] is $R_{l\,obs}$. Since CEST pools have a low relative concentration, the effect of the labile proton pool *b* can be neglected and $R_{1\,obs}$ expressed as:

$$R_{1\,obs} \approx \frac{R_{1a} + f_c R_{1c}}{1 + f_c} \quad \ldots [3.18]$$

Then from Equation [3.13] the adjusted Z-spectrum for 3 pools is:

$$Z_{ss}(\Delta\omega) = \frac{cos^2\theta.\ R_{1\,obs}}{R_{1p}} \quad \ldots [3.19]$$

The Z-spectrum after RF irradiation of duration $t_p$ is then given by:

$$Z(\Delta\omega, t_p) = (cos^2\theta\,.Z_i - Z_{ss}).e^{-R_{1P}t} + Z_{ss} \quad \ldots [3.20]$$

Where $Z_i$ is the initial magnetization before saturation (Zaiss, Moritz & Bachert, Peter, 2013, Zaiss et al., 2015). This allows for optimization of irradiation parameters that maximize the Z-spectrum and hence the $MTR_{asym}$.

## 3.3. Methods

### 3.3.1. Simulation

The CEST (Z) spectra for glycoCEST were simulated in Matlab (MathWorks 2014b) using a three-pool exchange model (Equation [3.20]). The dependence of CEST on RF irradiation power and duration was examined. Taking into account the specific absorption rate limit (Acheson et al., 1988), irradiation RF power was simulated between 0 and 4μT for a fixed pulse duration of 1 s and pulse duration was varied between 10 ms and 3.5 s while power was fixed at 1 μT. From the simulated $MTR_{asym}$ curves, the $MTR_{asym}$ integral was calculated within the glycogen resonance

frequency range (between 0.5 ppm to 1.5 ppm down field of water) and examined as a function of irradiation power and pulse duration.

The following parameters were used in the simulation: longitudinal relaxation rate and transverse relaxation rate for water pool $R_{1a}$ = 0.66 $s^{-1}$, $R_{2a}$ = 2 $s^{-1}$ , which is $T_{1a} \approx$ 1500 ms and $T_{2a} \approx$ 50ms for skeletal muscle at 3 T (Gold et al., 2004, Stanisz et al., 2005). The fraction of exchangeable protons for glycogen has been reported as $n_b \leq 3$ depending on the branching of the glycosyl links (Zijl. et al., 2007). Using $n_b$ = 3, proton fraction ($f_b$) = 0.00135 (using Equation [3.8] 50mM glycogen in water: 3*50/(2*55.5*1000) = 0.00135), exchange rate for glycogen is approximately 1000 $s^{-1}$ at room temperature (Liepinsh & Otting, 1996, Zijl. et al., 2007), chemical shift of the glycogen pool =1 ppm, longitudinal and transversal relaxation rates of pool *b* are approximately $R_{1b}$ =1.1 $s^{-1}$ ($T_{1b}$ = 900 ms) and $R_{2b}$ = 76.9 $s^{-1}$ ($T_{2b}$ = 13 ms) (Weis, Kullberg & Ahlström, 2018). Standard parameters were chosen for MT: $T_{1c}$=1 s, $T_{2c}$=8.7 µs, $f_c$=7.4 %, $k_{ca}$= 66 $s^{-1}$, $\Delta\omega_c$=0 ppm (Stanisz et al., 2005, Zaiss et al., 2015). The glycogen hydroxyl proton resonates between approximately 0.5 and 1.5 ppm down field from water (Zijl. et al., 2007), that is 63.87 Hz to 191.61 Hz at 3 T. We used 127.74 Hz (1 ppm) down field of water as the glycogen chemical shift signature point to evaluate the optimum irradiation parameters that maximizes the CEST signal.

### 3.3.2. CEST pulse sequence and acquisition parameters

The CEST sequence was implemented by adding a frequency selective continuous wave RF pulse on to a 2D gradient echo single-shot Echo Planar Imaging pulse sequence with a rectangular saturation pulse swept between -383.22 Hz to 383.22 Hz in intervals of 19.16 Hz (-3:0.15:3 ppm) with respect to the water resonance frequency.

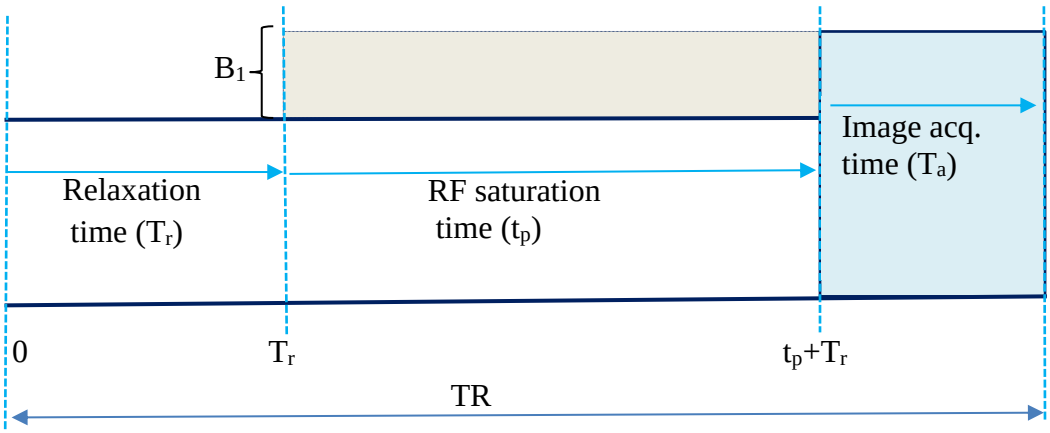


Figure 3.1: Illustration of the CEST-EPI pulse sequence. The repetition time (TR) is approximately equal to the sum of recovery time (Tr) and RF saturation time $t_p$.

Figure 3.1 shows the employed CEST sequence with a continuous wave (CW) RF irradiation of duration ($t_p$) and power ($B_1$). Since the 2D EPI image acquisition duration is very small, the repetition time can be assumed to be approximately equal to the saturation time plus relaxation recovery time. Hence, the RF duty cycle of 50% given by $t_p$/TR was selected for good RF amplifier performance (Jiang et al., 2016).

For both phantom and *in vivo* acquisitions, a 15-channel Tx/Rx knee coil was used with scanning parameters of: TR 2000 ms, TE 21 ms, 43 offset measurements (including two reference unsaturated measurements). Single slice scans with 5 mm thickness, 64 x 64 acquisition matrix and 220 x 220 mm FOV mm were acquired and analyzed using custom written Matlab program (MathWorks 2014b) to generate the Z-spectra and $MTR_{asym}$ curves.

### 3.3.3. *In vivo* validation

*In vivo* scans were performed on the calf muscle of 2 human volunteers on a 3 T Skyra (Siemens, Erlangen, Germany) according to protocols approved by the Faculty of Health Sciences Research Ethics Committee of the University of Cape Town. All experiments were performed following an informed written consent. The experiment was first performed at different saturation powers (0.5 µT - 4 µT) with a CW pulse duration of 1 s to validate the simulation. A second *in vivo* test was performed on a volunteer using the optimized RF irradiation parameters obtained from simulation and *in vivo* validation tests. For this a 1 s CW saturation pulse with power of 1.5 µT was applied. Curves were generated from selected 35x35x5 $mm^3$ region of interest (ROI) from the inferior part of the gastrocnemius muscle.

### 3.3.4. Phantom test

Five different Bovine liver glycogen (Type IX G0885, CAS Number: 0009005792, Sigma, Aldrich) concentrations (10mM, 20mM, 50mM, 100mM and 200mM) mixed with phosphate-Buffered Saline (PBS) solution with a pH of 7 were prepared and tested to demonstrate that the CEST effect changes with different glycogen concentrations at the optimal values of irradiation power and duration selected from the simulation. The concentration of glycogen is expressed in millimolar glycosyl units, with each glycosyl unit contributing 168 g/mol (Zijl. et al., 2007). For example, 100.8 mg of glycogen was dissolved in a 60 ml PBS solution to obtain a 10mM solution of glycogen (*168 mg/mmol x 0.01mol x 60ml = 100.8 mg*). The phantom scans were performed on a Siemens Skyra 3 T (Erlangen, Germany) scanner at the Athinoula A. Marthinos center for

Biomedical Imaging, Massachusetts General Hospital, Boston, USA. The CEST-weighted images for all offsets of each concentration were co-registered to the unsaturated (reference) image and the CEST spectrum was defined as the normalized water intensity ($M_{zw}/M_{0w}$) as a function of RF saturation frequency or chemical shift.

## 3.4. Results

### 3.4.1. Simulation

Figure 3.2 shows the simulated z-spectra and corresponding MTR asymmetry ($MTR_{asym}$) spectra as a function of RF irradiation power and duration. Spectral widening can be observed as either saturation power or duration increases.

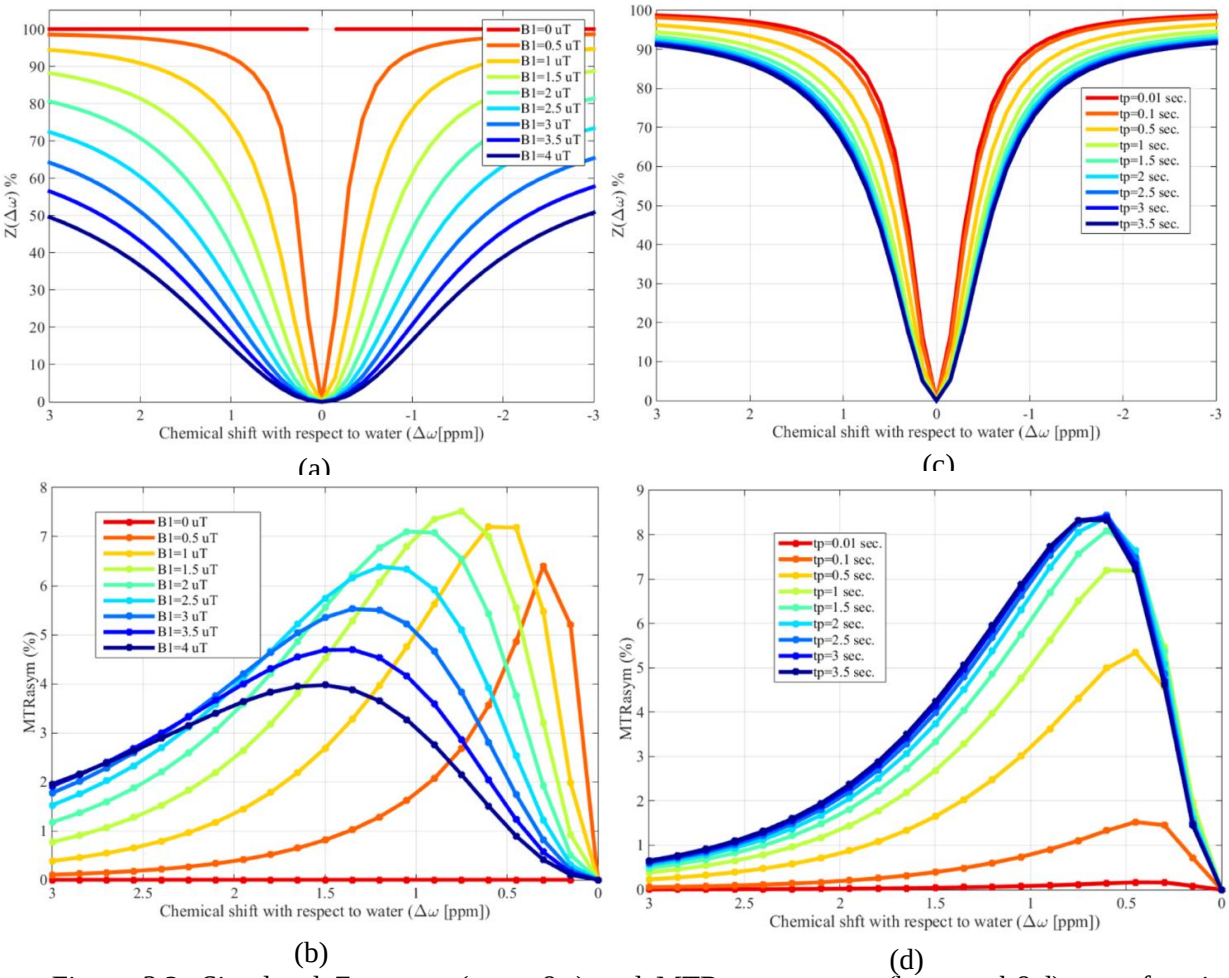


Figure 3.2: Simulated Z-spectra (top, a&c) and MTRasym curves (bottom, b&d) as a function of irradiation power (B1) (left, a&b) and irradiation pulse duration (right, c&d). A strong dependence of the CEST effect on saturation power is observed in both MTRasym curves and CEST spectra. Relatively slow CEST effect variations are observed at longer saturation durations. Irradiation power and duration were fixed at 1μT and 1s, respectively, when duration/power was varied.

The z magnetization is attenuated (saturated) with increasing saturation power. Changing pulse duration has less of an effect on CEST spectra than varying saturation power, the effect of saturation (spectral widening) approaches a steady state with further increase in saturation power. A similar effect is observed in the $MTR_{asym}$ curves (Figure 3.2 b&d). At lower saturation powers (0 – 1.5 μT) the $MTR_{asym}$ peak shifts towards 1 ppm. However, with a further increase in saturation power there is a line broadening and loss of the CEST effect. Figure 3.3 shows the simulated $MTR_{asym}$ integral values calculated between 0.5 to 1.5 ppm as a function of irradiation power and irradiation pulse duration. The simulated $MTR_{asym}$ integral increases towards a maximum at a saturation power of 1.5μT, decreasing at higher saturation powers. The $MTR_{asym}$ integral value also increases with increasing RF irradiation duration, levelling off at durations longer than ~2 s (Figure 3.3b).

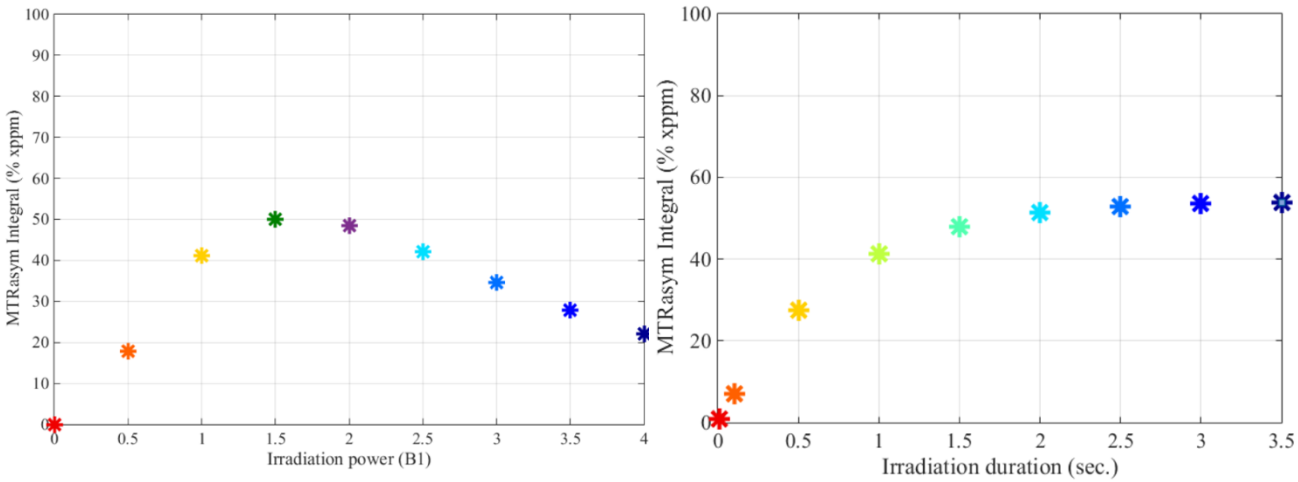


(a) (b)

Figure 3.3: Simulated MTRasym integral values calculated between 0.5 to 1.5 ppm as a function of (a) irradiation power and (b) irradiation pulse duration. The integrated MTRasym shows maximum value at 1.5μT RF power and a stable value beyond 2 seconds saturation duration.

### 3.4.2. *In vivo* test

Figure 3.4 shows z-spectra and corresponding $MTR_{asym}$ curves from in vivo tests at different saturation powers. In agreement with the simulation, a widening effect can be seen in the CEST spectrum with increasing saturation power. Table 3.1 shows that the $MTR_{asym}$ integral calculated between 0.5 – 1.5 ppm gradually increases with increasing irradiation power and decreases after reaching a maximum value at1.5 µT.

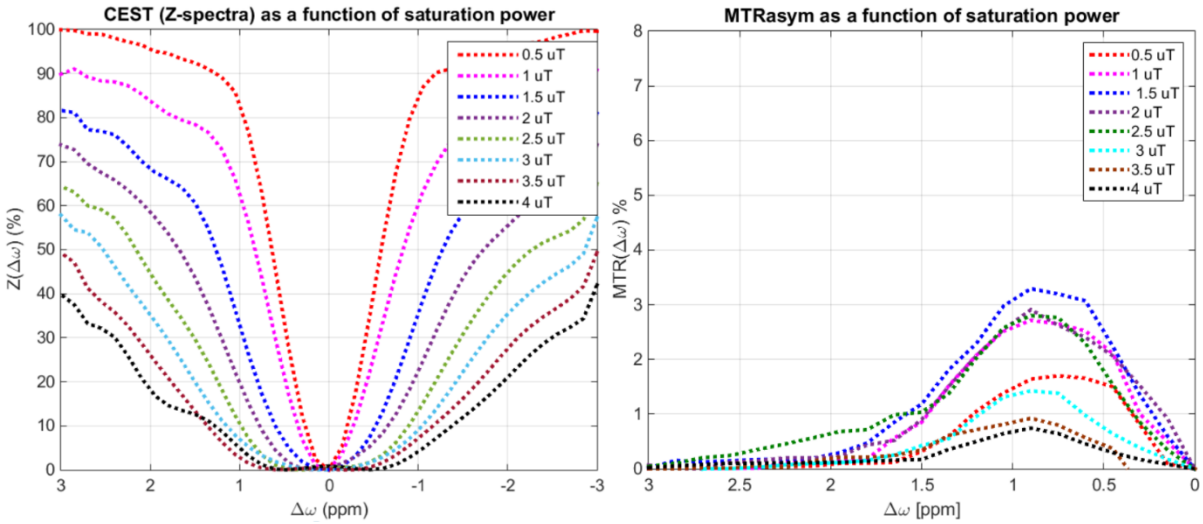


Figure 3.4: Z-spectra (left) and $MTR_{asym}$ curves (right) from a calf muscle of single volunteer acquired at different saturation powers. A widening effect in the Z-spectra is observed as the saturation power increases. Highest peak values are seen in the $MTR_{asym}$ curve at 1.5 µT.

| Saturation power | $MTR_{asym}$ integral |
|---|---|
| 0.5 µT | 10.31 |
| 1 µT | 17.74 |
| 1.5 µT | 21.17 |
| 2 µT | 18.04 |
| 2.5 µT | 17.33 |
| 3 µT | 7.98 |
| 3.5 µT | 5.12 |
| 4 µT | 3.98 |

Table 3.1 : $MTR_{asym}$ integrals between 0.5 and 1.5 ppm as a function of saturation power for in vivo acquisition on a calf muscle

Figure 3.5 shows the CEST and $MTR_{asym}$ curves for the calf muscle scan of a second volunteer acquired at the selected optimal irradiation parameters (1.5 µT saturation power and 1 s saturation duration). The "peak" at around 0.9 ppm in the $MTR_{asym}$ curve demonstrates the detection of glycogen-weighted signal using the selected irradiation parameters.

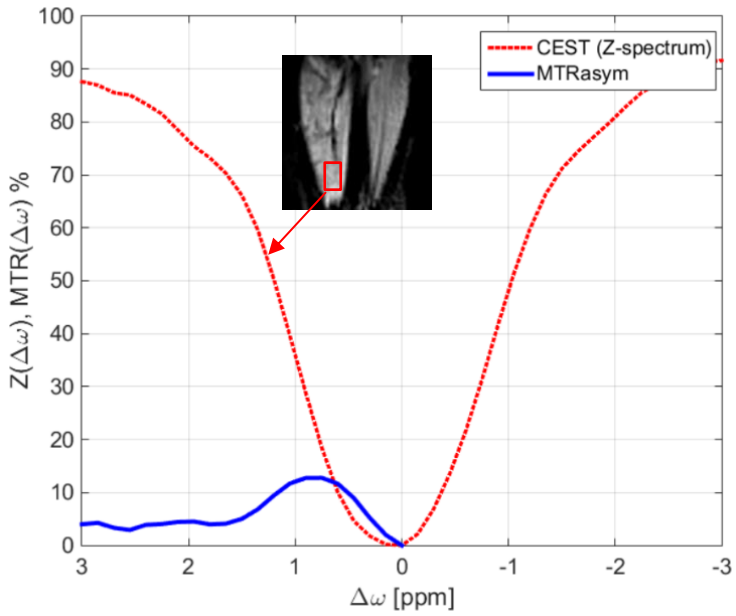


Figure 3.5: CEST spectrum and $MTR_{asym}$ curve of the *in vivo* test for a single volunteer acquired from the inferior part of the gastocnemius muscle

Figure 3.6 shows CEST images acquired using the selected optimal saturation power and duration (left to right) without saturation, after saturation at 1ppm and the MTRasym map overlaid on the reference image. The saturated image displays lower intensity due to the CEST effect.

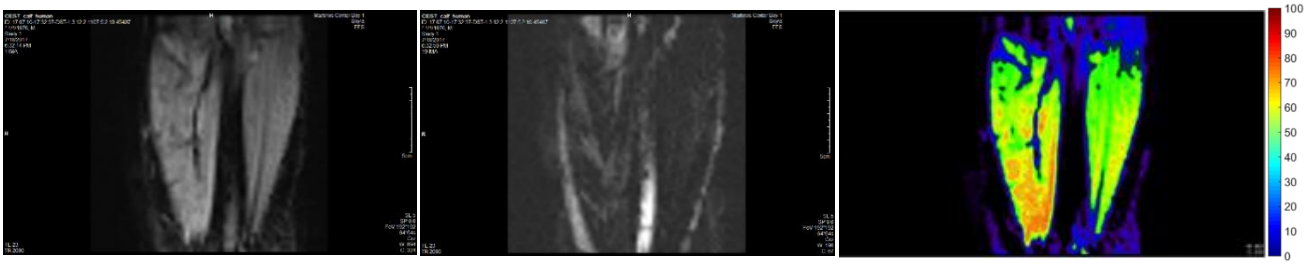


(a) (b) (c)

Figure 3.6: glycoCEST imaging of human calf muscle (a) unsaturated image, (b) saturated image at 1ppm, and c) color-coded MTRasym map at 1 ppm overlaid on the reference image.

### 3.4.3. Phantom test

The calculated maps of MTRasym at 1 ppm for 5 different glycogen phantom concentrations overlaid on the reference image (Figure 3.7) demonstrate the ability to detect glycogen-weighted signal using optimized RF saturation parameters for CEST at 3 T. In the MTRasym maps at 1ppm from water a slight intensity increase can be observed with increasing glycogen concentration. Figure 3.8 shows the CEST and corresponding MTRasym curves for 5 different glycogen concentrations, also demonstrating a larger CEST effect with increasing glycogen concentration.

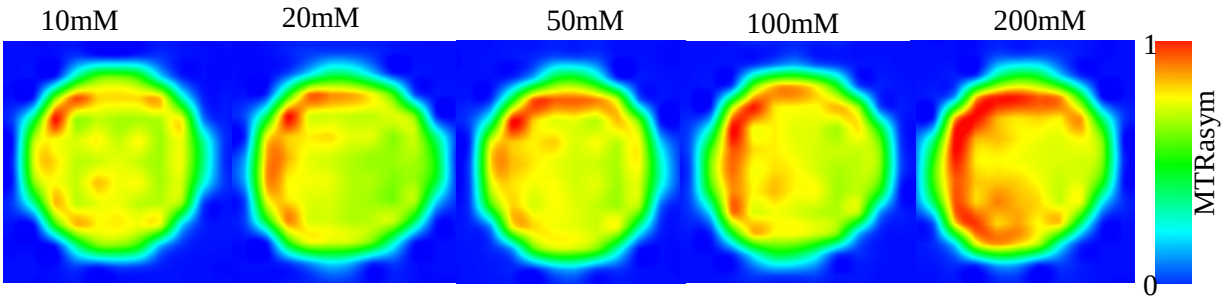


Figure 3.7: $MTR_{asym}$ maps of glycogen phantom images at 1 ppm overlaid with the reference image demonstrating the different glycogen concentration levels

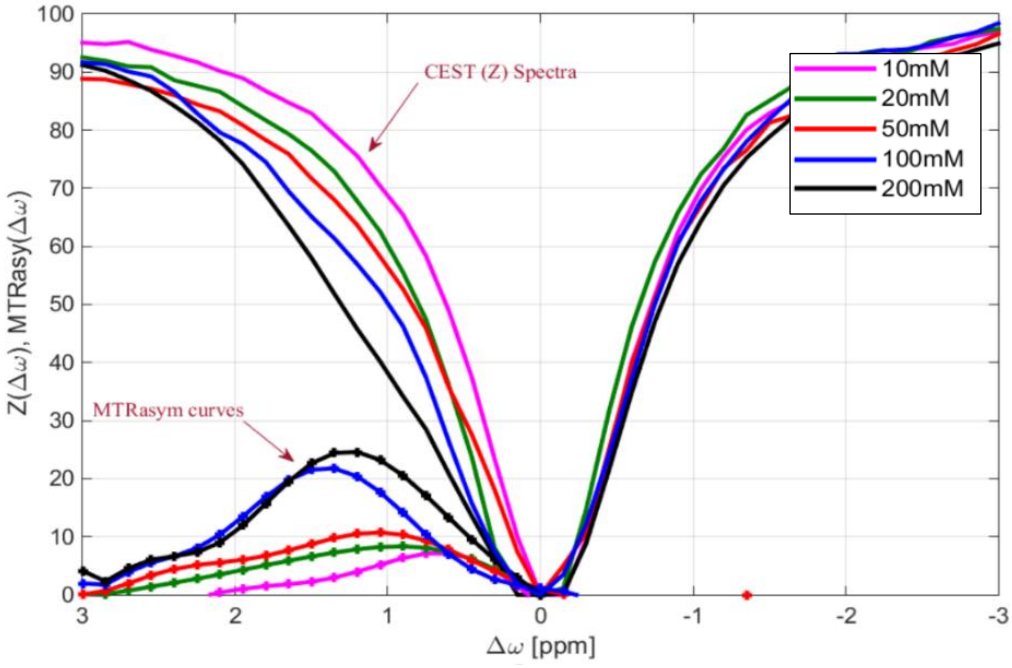


Figure 3.8: CEST-spectra and $MTR_{asym}$ curves of glycogen phantom tests at different concentration levels

Table 3.2 shows the $MTR_{asym}$ integral between 0.5 to 1.5 ppm and peak values at 1 ppm as a function of glycogen concentration. The $MTR_{asym}$ integral and peak values show a significant linear correlation (Pearson's r = 0.98 and 0.98 respectively, both p's < 0.05) with glycogen concentration.

.

| Concentration | $MTR_{asym}$ peak (max. 0.5 – 1.5 ppm) | $MTR_{asym}$ integral (0.5 – 1.5 ppm) |
|---|---|---|
| 10mM | 5.18 | 36.95 |
| 20mM | 8.34 | 53.55 |
| 50mM | 10.33 | 65.75 |
| 100mM | 17.46 | 104.32 |
| 200mM | 23.19 | 139.18 |

Table 3.2: $MTR_{asym}$ peak values and $MTR_{asym}$ integral between 0.5 and 1.5 ppm for glycogen phantom tests of different concentrations level showing a linear correlation with glycogen concentration

## 3.5. Discussion

Although CEST MRI is a promising technique to detect dilute CEST agents and microenvironmental properties, experimental measurement of the CEST effect is complex due to its dependence not only on CEST agent concentration but also on experimental parameters such as scanner field strength, RF irradiation amplitude and duration, pulse sequence and image acquisition scheme. Detecting glycogen using CEST MRI is more challenging due to its close resonance with free water, which makes it more likely to be contaminated by direct water saturation (spillover effect) and other CEST pools resonating at approximate frequencies due to smaller absolute chemical shift (Deng et al., 2016b). This is especially problematic at lower magnetic field strengths, such as 3 T, where the sensitivity of CEST signals substantially decreases compared to high and ultra-high magnetic fields (>7 T) scanners (Liu G, KWY. & MT., 2013).

However, an optimal irradiation power and saturation duration can be selected by balancing saturation efficiency, direct water saturation and MT (Desmond & Stanisz, 2012, Liu G, KWY. & MT., 2013, Sun et al., 2007) to maximize the measurable CEST effect.

Weak power causes inefficient labile proton saturation leading to an attenuated CEST effect, on the other hand, very strong RF power directly attenuates the bulk water signal (in addition to saturating the solute protons), reducing the sensitivity and specificity of CEST (Kim, Jinsuh et al., 2015, Sun & Sorensen, 2008, Sun et al., 2011).

As demonstrated in the simulated z-spectrum (Figure 3.2 and 3.3), very weak irradiation power (<0.5μT) causes saturation efficiency for the solute resonance to be low, and the water signal reduction due to saturation transfer is small. The saturation efficiency increases gradually with the applied irradiation power and reaches its optimal value (≈1.5 μT), correspondingly reducing the water proton signal. On the other hand, strong saturation power (>2.5 μT) introduces additional spillover effects, thus reducing proton transfer ratio as reflected by the $MT_{Rasym}$ curve at the glycogen proton frequency (≈1 ppm) (Figure 3.2b).

The simulated $MTR_{asym}$ integral also increases asymptotically towards a maximum at durations longer than ~2 s (Figure 3.3b), reflecting the steady state proton exchange between solute and water pool where further irradiation is not required. As saturation duration increases, higher saturation is accumulated and a larger CEST effect is seen compared to short durations. The simulation results confirm the dependence of $MTR_{asym}$ on RF saturation power and duration, identifying a maximum $MTR_{asym}$ peak at a power of 1.5 μT, with a pulse duration of 1 s. Beyond 1 s only an incremental gain in MTRasym peak is achieved.

In agreement with the theory and simulation, in the *in vivo* experiment a widening effect is seen in the CEST spectrum when saturation power is increased (Figure 3.4). Even though the $MTR_{asym}$ curves plotted as a function of saturation power do not exactly mirror the results obtained via simulation (compare Figure 3.3), the peak $MTR_{asym}$ is also seen for an acquisition with 1.5 μT saturation power. The $MTR_{asym}$ integral calculated between 0.5 – 1.5 ppm (Table 3.1), also shows a maximum at 1.5 μT, with lower and higher irradiation powers resulting in smaller values of $MTR_{asym}$, as expected.

Overall, the simulations and *in vivo* tests show that for a continuous wave CEST experiment, using a 2D gradient echo single shot EPI pulse sequence, hydroxyl protons are more sensitive to approximately 1 - 2 μT irradiation power, and longer saturation durations (1 – 2.5 s) are desirable to achieve maximal CEST signal. The specific absorption rate limit during *in vivo* tests (Acheson

et al., 1988) restricts the irradiation duration. Hence a 1 s irradiation duration, which results in a 50 % duty cycle as recommended (Jiang et al., 2016) was selected as an optimal value for our test. However, this can be increased by selecting a longer repetition time (TR) at the cost of extending scanning time.

Because glycogen hydroxyl protons resonate close to the water resonance frequency and since their proton exchange is intermediate to fast in the MR time scale, they are not visible in a standard proton spectrum under physiological conditions (Zijl. et al., 2007), especially at lower magnetic fields. Hence, "suppression" or "dips" around the expected glycogen resonance are not directly observable in the CEST spectrum. However, peaks in the $MTR_{asym}$ curves between 0.75 ppm - 1.2 ppm are evidence of glycogen hydroxyl proton exchange and are more prominent at higher glycogen concentrations (Figure 3.7).

Higher glycogen phantom concentrations result in asymmetric broadening of the z-spectrum. Correspondingly an increase in signal intensity with increasing glycogen concentrations was apparent in the $MTR_{asym}$ maps at 1ppm overlaid on the reference image (Figure 3.6). The amount of saturation depends on the proton exchange rate and concentration, and saturation efficiency can only approach a maximum of 100% which may be reached at lower concentrations and higher exchange rates (Zijl. et al., 2007). Hence the magnitude of the CEST effect may not scale linearly with concentration. However, phantom test results in Table 3.2 show that $MTR_{asym}$ integral has a significant linear correlation ($r = 0.981$, $p < 0.05$) with glycogen concentration. Although $MTR_{asym}$ integral values do not represent absolute glycogen concentrations, this confirms that they can be used as glycogen-weighted values for comparative analysis, including longitudinal studies, perfusion studies, or muscle glycogen depletion-repletion studies in sports physiology.

The principle of endogenous glycogen CEST (glycoCEST) imaging was first demonstrated by van Zijl et al (Zijl. et al., 2007) in the excised perfused mouse liver at 4.7T. Other studies have been conducted to study the distribution of glucose in mice livers at 4.7 T using a PARACEST sensor (Ren et al., 2008), at 9.4 T using CEST (Sagiyama K, Zhang S & Dimitrov I, 2014). *In vivo* studies of glycogen in humans are limited and only a few have been performed at 3 T (Deng et al., 2016b, Kim, Mina et al., 2009). In agreement with the literature, a higher peak at around 0.9 to 1 ppm in the $MTR_{asym}$ curve was observed in our *in vivo* test on a human calf muscle demonstrating the detection of glycogen-weighted signal using the selected irradiation parameters at 3 T (Figure 3.5).

The image acquired after applying saturation (Figure 3.6b) displays lower intensity because of the CEST effect from presaturation at 1 ppm. The $MTR_{asym}$ map (Figure 3.6c) shows regions where there is strong CEST-weighted effect, presumably showing regions of the imaged calf muscle where glycogen storage is highest. The *in vivo* test results demonstrate the possibility of detecting glycogen hydroxyl protons at 3 T using optimized irradiation parameters.

Further work could assess the dependence of the glycoCEST effect on readout RF pulse flip-angle and pulse sequence type.

## 3.6. Conclusion

Given that the concentration of certain endogenous molecules is very low, detection using the CEST method requires optimization of experimental parameters to maximize the CEST effect and reduce competing factors. Along with the $B_0$ magnetic field strength, RF irradiation parameters play a determining role in the size of the observable CEST effect. In this study, analytical solution of the Bloch-McConnell equations was used to find the optimal RF irradiation power and duration that maximize the glycoCEST weighted signal, which were found to be 1.5 μT and 1 s, respectively, for the 2D gradient echo ss-EPI pulse sequence. *In vivo* tests were performed at different RF saturation powers to validate the simulation results. Further phantom and *in vivo* test results demonstrate the ability of the optimized CEST MRI sequence to detect and measure different concentrations of glycogen at 3 T. This ability to non-invasively measure muscle glycogen using CEST MRI has the potential to advance our understanding of glycogen metabolism in sports physiology, as well in glycogen related disorders.

# Chapter 4

## Real-time simultaneous shim and motion measurement and correction in glycoCEST MRI using Double Volumetric Navigators (DvNavs)[1]

Gizeaddis L. Simegn[2], Andre van der Kouwe[2,3,4], Frances Robertson[2,5], Ernesta Meintjes[2,5], and Ali Alhamud[2,5]

## Abstract

CEST MRI allows for indirect detection of molecules with exchangeable protons, measured as a reduction in water signal because of continuous transfer of saturated protons. CEST requires saturation pulses on the order of a second, as well as repeated acquisitions at different offset frequencies. The resulting extended scan time makes CEST susceptible to subject motion, which introduces field inhomogeneity, shifting offset frequencies and causing distortions in CEST spectra that resemble true CEST effects. This is a particular problem for molecules that resonate close to water, such as the hydroxyl group in glycogen. To address this, a technique for real-time measurement and correction of motion and field inhomogeneity is proposed. A CEST sequence was modified to include Double volumetric Navigators (DvNavs) for real-time simultaneous motion and shim correction. Phantom tests were conducted to investigate the effects of motion and shim changes on CEST quantification, and to validate the accuracy of DvNav motion and shim estimates. To evaluate DvNav shim and motion correction in vivo, acquisitions including 5 experimental conditions were performed in the calf muscle of 2 volunteers. Phantom data show that DvNav-CEST accurately estimates frequency and linear gradient changes because of motion and corrects resulting image distortions. In addition, DvNav-CEST improves CEST quantification in vivo in the presence of motion. The proposed technique allows for real-time simultaneous motion and shim correction with no additional scanning time, enabling accurate CEST quantification even in the presence of motion and field inhomogeneity.

[1] Chapter has been peer reviewed and published in Magnetic Resonance in Medicine (MRM)

[2] *UCT Medical Imaging Research Unit, Division of Biomedical Engineering, Department of Human Biology, University of Cape Town, Cape Town, South Africa*
[3] *Athinoula A. Martinos Center for Biomedical imaging/MGH, Charlestown, MA, United States*
[4] *Department of Radiology, Harvard Medical School, Boston, MA, United States*
[5] *Cape Universities Body Imaging Centre (CUBIC-UCT), Cape Town, South Africa*

**Keywords:** $B_0$ correction, chemical exchange saturation transfer, CEST, double volumetric navigator, DvNav, glycogen, motion correction.

## 4.1. Introduction

Magnetic resonance spectroscopy (MRS) allows for direct detection and quantification of different endogenous metabolites containing $^1$H. However, in vivo measurement of certain metabolites remains challenging because of their low concentrations. In 2000, Ward and Balaban (Ward, K. M., Aletras & Balaban, 2000) demonstrated that molecules can be detected indirectly through the chemical exchange of protons from preselected labile groups with free water. This technique is CEST MRI.

Because hydrogen nuclei bound to metabolites and those in free water possess different chemical shifts, chemical exchange processes can be probed by selectively saturating the bound hydrogen nuclei and detecting the attenuated MR signal in the water pool. CEST typically involves exchange of protons from amides (-NH), termed Amide Proton Transfer (APT) (Zhou, Jinyuan et al., 2003), amines ($-NH_2$) and hydroxyls (-OH). Transfer of amine protons is involved in the quantification of glutamate (Glu-CEST), γ-aminobutyric acid (GABA) (Cai et al., 2012) and creatine (Cr-CEST), and transfer of hydroxyl protons in measuring glucose (Gluco-CEST), myo-inositol (MICEST), as well as glycosaminoglycan content (GagCEST) in cartilage (Ling et al., 2008). The feasibility of detecting glycogen using CEST (glycoCEST) from hydroxyl protons (–OH) was demonstrated previously in vitro and in vivo in animal studies of the liver at 4.7 T (Zijl. et al., 2007).

In the ideal CEST experiment, quantification is achieved by measuring the reduction of the water signal because of saturation transfer ($S_{sat}$) relative to the corresponding unsaturated image ($S_0$). However, there are several factors that complicate CEST measurements. These include magnetization transfer (MT) between semi-solid macromolecules and water, and direct water saturation (DS) (Kim, Mina et al., 2009, Wu, B. et al., 2016, Zijl. & Yadav, 2011).These effects reduce the attenuated water signal and should be eliminated for reliable quantification of CEST.

To mitigate the effects of MT and DS, and isolate the effects of chemical exchange, instead of comparing only the signal reduction caused when saturating a specific spectral location ($+\Delta\omega$ with respect to water) to that without saturation, the CEST effect is assessed by subtracting the labeled signal ($S_{sat}(+\Delta\omega)$) from the reference signal acquired after applying a saturation pulse at the

opposite spectral location ($S_{sat}(-\Delta\omega)$) (Baguet & Roby, 1997). This assumes that the MT and DS effects are symmetrical about the water frequency. The most commonly used CEST metric, the Magnetization Transfer Ratio ($MTR_{asym}$) at $+\Delta\omega$, is defined as:

$$MTR_{asym} = \frac{(S_{sat}(-\Delta\omega) - S_{sat}(+\Delta\omega))}{S_0} \quad \text{.....[4.1]}$$

where $S_{sat}(+\Delta\omega)$ and $S_{sat}(-\Delta\omega)$ are the measured signals with RF saturation at +Δω and -Δω, respectively, and $S_0$ is the signal measurement without RF saturation (Baguet & Roby, 1997, Zhou, Jinyuan et al., 2003, Zhou, J. et al., 2003, Zhou, J. et al., 2008). Although it is difficult to absolutely quantify the CEST effect, the relative magnitude can be described using $MTR_{asym}$. Although $MTR_{asym}$ is the most widely used metric to quantify CEST effects, it is contaminated by asymmetry of MT in the frequency range close to the water resonance (J. et al., 2007). Therefore, instead of comparing the saturated water signals at a pair of offsets, CEST is quantified by comparing the saturated water signals over a range of offsets. Furthermore, in the presence of severe $B_0$ inhomogeneity, the labeled and reference scans will no longer be symmetric about the true water resonance of the spin system (He Zhu, 2010, Sun, van Zijl & Zhou, 2005) resulting in a $B_0$ inhomogeneity-dependent MTR offset that may cause errors in CEST quantification.

Because CEST acquisitions are repeated at different spectral offsets to adequately sample the CEST spectrum (Z-spectrum) for each voxel, the acquisition will be long when using traditional imaging readouts. This causes CEST MRI to be sensitive to motion and $B_0$ inhomogeneity. To decrease the overall acquisition time, rapid MRI acquisition techniques such as Rapid Acquisition with Relaxation Enhancement (RARE) (Liu et al., 2009), EPI (Liepinsh & Otting, 1996, Sun et al., 2013), True Fast Imaging with Steady State Free Precession (FISP) (Shah et al., 2011), Gradient and Spin Echo (GRASE)(He Zhu, 2010), Variably-accelerated Sensitivity Encoding (vSENSE) (Zhang et al., 2017), keyhole (G., E. & E., 2012), as well as optimized spiral-centric-reordered GRE approaches (Zaiss, Ehses & Scheffler, 2018) have been adapted for CEST. Fast imaging techniques, however, cannot eliminate motion between the different offset frequency acquisitions. If there is a mismatch between the corresponding voxels because of subject motion, the acquired Z-spectrum will not be accurate and high signal variations (peaks or dips) that resemble those expected from the metabolites of interest may be introduced in the curve (Gizeaddis L. Simegn, 2017). The effect of motion in CEST MRI is almost unexplored. The few studies that

examine motion correction in CEST MRI are based either on rigid image registration (Schuenke et al., 2017) or retrospective time domain analysis (Nirbhay N. Yadav, 2015).

During a prolonged CEST scan, several sources can alter the homogeneity of the static shim prepared by the MRI scanner. These include subject motion (Ward, Heidi A., Riederer & Jack, 2002), breathing (Pfeuffer et al., 2002), heating of the iron plates in the shim trays by eddy currents and mechanical vibrations (Benner et al., 2006, Foerster, Tomasi & Caparelli, 2005). This can severely impact the accuracy of the CEST measurement. For example, at 3 T, a shift of just 100 Hz in the central frequency may cause the amine ($-NH_2$) group to be saturated instead of the -OH group in glycogen. Although shim changes before the start of the scan can be corrected by the scanner's automatic shimming or by manual shim optimization, standard techniques cannot correct shim changes that occur during the scan. Given that the endogenous CEST signal is only a few percent, accurate quantification requires correction of field inhomogeneity-induced measurement errors.

To date, shim has been corrected retrospectively in CEST imaging using a pre-acquired $B_0$ map (Kim, Mina et al., 2009, Sun, Farrar & Sorensen, 2007), or by fitting the CEST spectrum to a higher-order polynomial (Zhou, Jinyuan et al., 2003, Zhou, J. et al., 2008). In the first method, the local $B_0$ shift at each voxel is determined from separately acquired gradient-echo phase images or using Water Saturation Shift Referencing (WASSR). WASSR uses a weak saturation pulse to measure the direct water saturation at each voxel (Kim, Mina et al., 2009). Assuming that maximal saturation occurs when the saturation offset equals the $B_0$ shift, the offset in the acquired CEST data is corrected, effectively moving the center of the Z-spectrum for each voxel back to 0 Hz. Alternatively, CEST spectra are fitted to a polynomial, where the minimum is deemed to be the reference frequency and each voxel's CEST spectrum is shifted accordingly (Zhou, Jinyuan et al., 2003, Zhou, J. et al., 2008). These techniques, which rely on sampling the minimum of the CEST spectrum in sufficient detail, are only applicable when the spectrum is symmetric and the water peak is sharp, or if the CEST agents' exchangeable protons are sufficiently far from water that small errors in $B_0$ correction do not cause problems (i.e. MTC and DS effects are small). It is worth noting that these methods cannot detect and remove errors that occur because of motion and dynamic changes in field inhomogeneity between different frequency offsets.

In contrast, navigator methods are able to detect $B_0$ changes throughout the scan and correct these in real time by adjusting both zeroth- and higher-order shims. Navigators can also correct for motion during the scan by updating the slice positions and gradient coordinate system (Alhamud et al., 2012, Tisdall et al., 2012, van der Kouwe, Benner & Dale, 2006), and are advantageous for CEST over hardware-based motion detection methods (Andrews-Shigaki et al., 2011, Lange et al., 2012, Zaitsev, M. et al., 2006) in that they can be inserted into unused time during the imaging sequence and require no additional hardware. To accurately measure motion and shim changes, navigator images require a consistent contrast independent of the CEST signal. Volumetric imaging navigators have been used previously for prospective motion and shim correction in diffusion tensor imaging (Alhamud et al., 2016), single voxel spectroscopy (Hess et al., 2011) and chemical shift imaging (Hess Aaron T., 2012). A similar approach based on dual-echo Prospective Motion correction (PROMO) has also been reported to correct for motion in single voxel spectroscopy(Keating & Ernst, 2012).

The current work presents a method for real-time simultaneous measurement and correction of motion and field inhomogeneity, in terms of frequency (zeroth-order) and linear (first-order) shim gradients, in CEST MRI using ultrafast double volumetric navigators (DvNavs).

## 4.2. Methods

### 4.1.1. CEST-EPI pulse sequence

The CEST MRI pulse sequence consists of three blocks/stages (Figure 4.1a): relaxation, saturation and image acquisition. A long recovery period ensures sufficient magnetization (Mz) before to excitation. The relaxation period is followed by RF saturation and comprises either a long continuous-wave radio frequency pulse or a train of short pulses. The current implementation uses a long continuous-wave pulse. For image acquisition, we use 2D gradient echo single-shot echo planar imaging. These 3 blocks are repeated for saturation pulses with chemical shifts ranging from -3 to 3 ppm relative to free water in increments of 0.15 ppm.

### 4.1.2. Volumetric navigated CEST-EPI for prospective motion correction

The volumetric navigator (vNav) was previously implemented in DTI (Alhamud et al., 2012), single voxel spectroscopy (Hess et al., 2011), chemical shift imaging (Hess Aaron T., 2012), MEGA-SPECIAL (Saleh et al., 2016) and morphometry (Tisdall et al., 2012). The vNav uses

multi-shot EPI with 3D encoding. A single complete slice of k-space is collected with a Cartesian sampling scheme after each excitation. The full navigator consists of a stack of k-space slices collected across multiple excitations.

Because the relaxation period in the CEST sequence occupies a significant portion of the repetition time (TR), the vNav was inserted into this block, immediately before the saturation block (Figure 4.1b). This ensures that all CEST measurements are affected equally. A small flip angle (2°) further ensures minimal impact on the CEST signal. vNav sequence parameters TE 6 ms, repetition time ($TR_{vNav}$) 11 ms, bandwidth 4882 Hz/px, 6/8 slice partial Fourier, turbo factor 32, acquisition matrix 32 x 32 x 32, resolution 8 x 8 x 8 $mm^3$, and FOV 256 mm; duration 264 ms.

For pose estimation, each 3D navigator magnitude image is compared to a reference, selected to be the first navigator after the dummy scans. Prospective Acquisition CorrEction (PACE) (Thesen et al., 2000), performed immediately after the navigator acquisition, computes translation and rotation parameters relative to the reference. Motion estimates are sent to the sequence and slice position and orientation are updated for subsequent CEST and vNav acquisitions. The complete navigator block, including computation and transmission of the motion estimates back to the sequence, requires 344 ms and fits into the CEST relaxation period without requiring any additional time.

### 4.1.3. DvNav CEST-EPI for prospective motion and shim correction

For simultaneous shim and motion correction, the navigator sequence was modified to acquire a pair of navigators (double vNavs) with different echo times (TE1/TE2 = 4.8/7.0 ms). The 2.2 ms difference in TE is chosen so that fat and water are in phase at 3 T. The partitions of the 2 navigators are acquired in an interleaved fashion as shown in Figure 4.1c. Because of the longer TE2, the TR of the navigator had to be increased to 13 ms, increasing the total acquisition time for the pair of navigators to 624 ms. All other parameters are as for vNav-CEST.

The sequence protocol was enabled to run with 3 options; the standard CEST sequence (CEST), DvNav-CEST with only prospective motion correction, and DvNav-CEST with prospective motion and shim correction.

The magnitude and phase images of both navigators (vNav1 and vNav2) are generated after acquisition. Pose estimation is performed in real-time using successive vNav1 images and shim

correction using successive navigator pairs. Each vNav1 image is co-registered to the reference using PACE and motion estimates are sent back to the sequence.

A 3D field map is computed by complex division of the vNav1 and vNav2 phase images. Voxels with low SNR are excluded using a mask created from the vNav1 magnitude image. Phase unwrapping is performed online using Phase Region Expanding Labeler for Unwrapping Discrete Estimates (PRELUDE) (Jenkinson, Mark, 2003). Motion parameters calculated from vNav1 are used to reorient the field map to the current position. Because DvNav-CEST effectively consists of 2 interleaved sequences with different FOVs, 2 frequency ($\Delta$Fs) and first order shim (linear shim gradients $G_x$, $G_y$ and $G_z$) estimates are calculated online, 1 for the selected CEST FOV and 1 for the DvNav FOV. The shim estimate for the DvNav is calculated using an unweighted least squares regression (Hess et al., 2011). For CEST, the shim estimate within the plane uses a weighted least squares regression, where the weighting of each navigator voxel is according to its intersection with the CEST FOV, whereas the through-plane (slice direction) shim is set equal to that of the DvNav. Shim parameters for CEST and DvNav are sent to the sequence.

First, slice position and orientation are corrected for both CEST and DvNav, followed by adjustment of the linear shim gradients for both sequences. Frequency correction involves recalculating the frequency and the phase of the RF and ADC pulses for both the vNav and CEST sequences. Although higher order shim terms can be calculated from the field map, only the linear terms can be applied in real time by the hardware. Using 6/8 partial Fourier in the slice direction, the total time required for the DvNav block (including communication time) is ~704 ms, which is short enough to fit inside the CEST relaxation time without requiring any additional imaging time. Therefore, any motion and accompanying field changes are corrected immediately after the navigator block so that the CEST offset is corrected in the very next measurement. Because the first measurement in the CEST acquisition will not be shim corrected, 2 reference measurements (images without saturation) are acquired. This ensures that shim-corrected data are available for all CEST offsets, including the reference. To avoid interaction with the DvNav, the standard frequency offset correction for the Siemens platform based on the non-phase-encoded echoes embedded into each EPI readout was disabled during DvNav-CEST acquisitions. Figure 2 shows a flow diagram of the DvNav-CEST sequence.

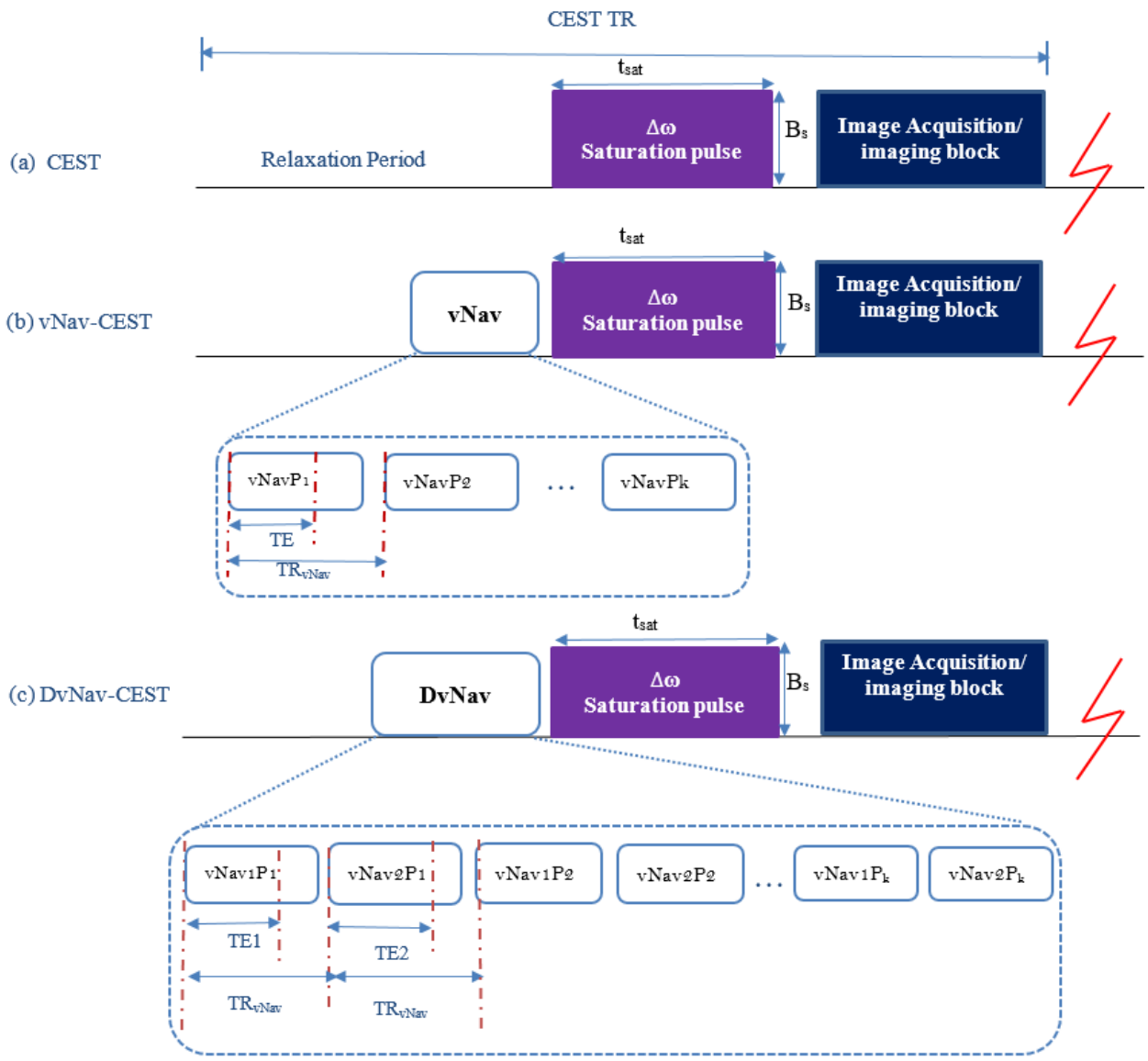


Figure 4.1: (a) Standard CEST-EPI sequence blocks; $t_{sat}$ and $B_s$ are, respectively, the duration and amplitude of the saturation pulse. (b) vNav-CEST with the volumetric navigator (vNav) inserted for prospective motion correction. (c) DvNav-CEST with a pair of volumetric navigators (DvNavs) inserted for real-time motion and shim correction. Individual partitions (P) of the pair of navigators are acquired in an interleaved fashion. **vNavP**i, **vNav1P**$_i$ and **vNav2P**$_i$ are the i$^{th}$ partitions of **vNav**, **vNav1** and **vNav2**, respectively; k is the total number of partitions.

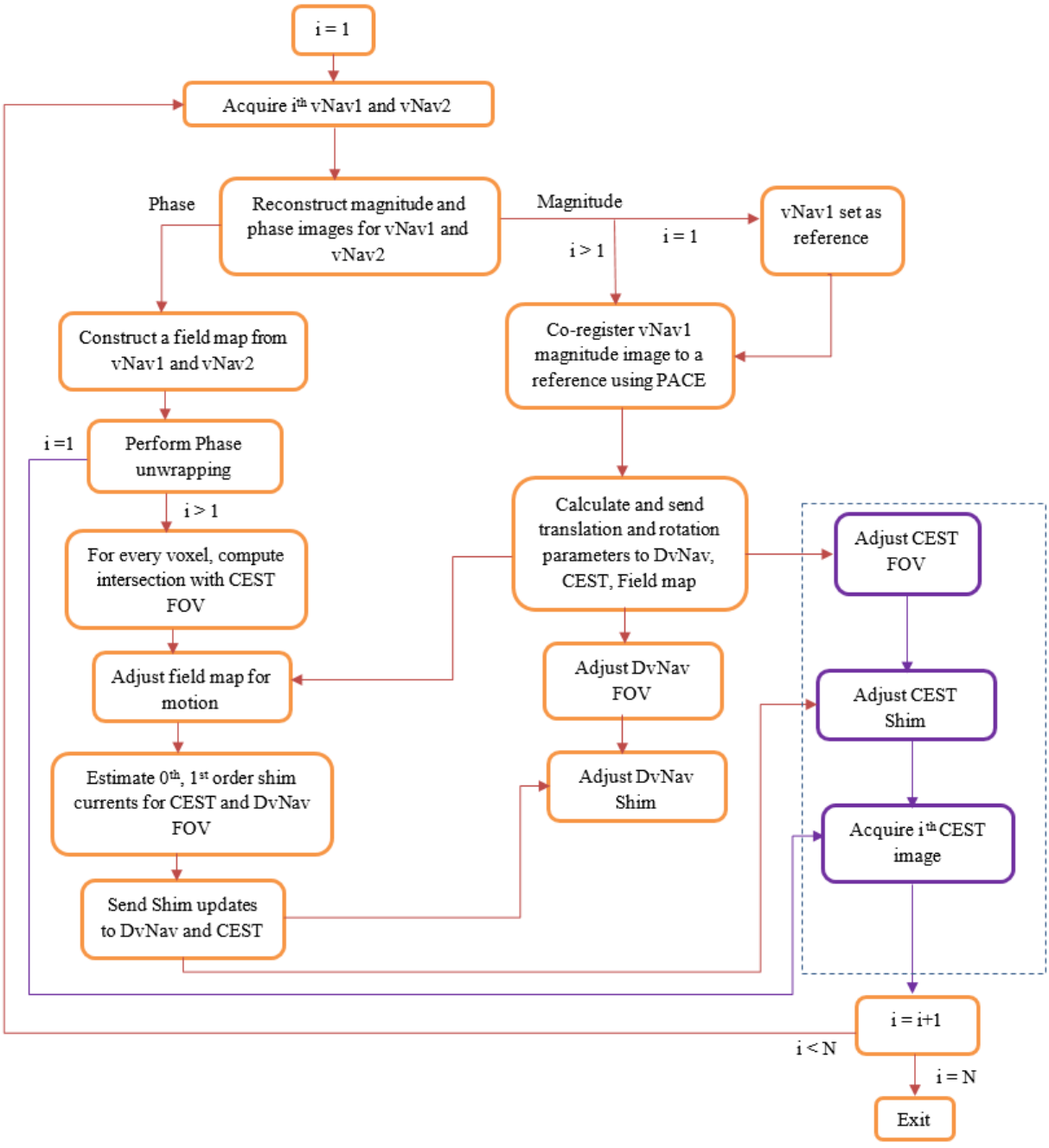


Figure 4.2: Flow diagram showing how the DvNav sequence (orange blocks) is integrated into the CEST acquisition (purple blocks) to perform real-time motion and shim correction. Shim correction is applied to all CEST measurements except the first one. N = total number of CEST measurements.

### 4.1.4. MRI data acquisition and scanning protocols

All scans were performed on a Skyra 3 T (Siemens, Erlangen, Germany) according to protocols that had been approved by the Human Research Ethics Committee of the Faculty of Health Sciences, University of Cape Town. Sequences were tested on water, pineapple, and bovine liver glycogen (Type IX G0885, CAS Number: 9005 79 2, Sigma, Aldrich) phantoms, and in vivo on the calf muscle of 2 volunteers using a 15-channel Tx/Rx knee coil. vNav parameters were as described earlier. The CEST parameters for both in vitro and in vivo acquisitions were: TR = 2000 ms (including the navigator time), TE = 21 ms, 1 average, single slice, slice thickness = 5 mm, 64 x 64 acquisition matrix and FOV = 220 mm. Each CEST acquisition included 2 reference measurements and 41 CEST offsets between -3 and 3 ppm (relative to free water) in increments of 0.15 ppm with an optimized rectangular RF saturation pulse of duration 700 ms and amplitude 1.5 μT; total CEST acquisition time 86 s. MATLAB (The MathWorks, Natick, MA) was used to process the images and generate CEST and $MTR_{asym}$ curves. For all acquisitions, glycogen concentrations were determined by integrating the $MTR_{asym}$ curve across the region where glycogen resonates (0.5 – 1.5 ppm downfield of water) (Zijl. et al., 2007).

### 4.1.5. Validations

#### I. Assessing the effect of the vNavs on CEST and vice versa

First, we investigated the effect of the navigator on CEST saturation and acquisition efficiency, as well as the effect of the CEST saturation pulse on the navigator signal. To this end, a pineapple was scanned twice, once using the standard CEST sequence and again using the DvNav-CEST sequence, both without motion. We examined how the navigator signal intensity varied for different CEST offsets and compared the CEST and $MTR_{asym}$ curves for the 2 acquisitions.

#### II. Assessing the effect of motion and $B_0$ inhomogeneity on CEST quantification

The effect of motion on CEST data was examined by scanning a pineapple using the standard CEST sequence both without (NoMo) and with (Mo) motion. A motion stick was used to introduce pose changes during the "with motion" acquisition. The $MTR_{asym}$ curves were integrated from 0 to 3 ppm downfield of water to compare effects on quantification.

The effect of $B_0$ inhomogeneity was assessed by scanning a 50mM bovine glycogen phantom with saturation pulses applied at -1, 0, and 1 ppm while intentionally manipulating the zero- and first-

order shims. After the baseline acquisition, the acquisition was repeated with the central frequency manually adjusted by ±32 Hz, ±64 Hz, ±96 Hz, ±128 Hz, and ±160 Hz from its nominal value (equivalent to ±0.25 ppm, ±0.5 ppm, ±0.75 ppm, ±1 ppm, and ±1.25 ppm at 3 T). Next, the linear shim gradient values were manually adjusted simultaneously in $G_X$, $G_Y$ and $G_Z$ by ±5 µT/m, ±10 µT/m and ±20 µT/m. The $MTR_{asym}$ values in a 35x35x5 $mm^3$ ROI at 1ppm downfield of water were compared for the different acquisitions.

### III. Performance of the DvNavs in estimating and correcting zero- and first-order shim changes

To assess the ability of the DvNavs to accurately detect and correct zero- and first-order shim changes, the central frequency and linear gradients were manually adjusted for successive DvNav-CEST acquisitions. First a baseline acquisition was performed on the standard MRI water phantom with the scanner's initial system settings. The acquisition was then repeated with the system frequency adjusted by 32 Hz, 64 Hz, 96 Hz, 128 Hz, and 160 Hz, respectively. These frequency shifts (0.25 – 1.25 ppm in steps of 0.25 ppm) were selected to assess the ability of the DvNav to correct frequency changes of the same order as the chemical shift of the glycogen hydroxyl group. Next, the acquisition was repeated with the gradient values changed by 10 µT/m in Gx only, both Gx and Gy, and finally Gx, Gy, and Gz together. DvNav shim correction was applied to all acquisitions. Because shim correction is only applied from the second measurement, we compared, for each acquisition, the first uncorrected CEST reference image to the second shim-corrected reference image. In addition, shim estimates computed by the DvNavs were compared to known adjustments.

### IV. *In vivo* validation

To investigate the benefits of real-time simultaneous motion and shim correction on CEST data in the presence of subject motion *in vivo,* 5 acquisitions were performed on the calf muscle, targeting the middle of the gastrocnemius, in each of 2 healthy adult male volunteers: 2 DvNav-CEST acquisitions without motion (NoMo) – 1 without correction (-NoCo) and 1 with both motion and shim correction (-AllCo); and 3 acquisitions with motion (Mo) – 1 without correction (-NoCo), 1 with motion correction only (-MoCo), and the last with both motion and shim correction (-AllCo). Before the scan session, participants were instructed to lie still unless prompted to move. For acquisitions with motion, subjects were instructed to change their position slightly twice to the left

and twice to the right (for volunteer 1), and 4 times progressively to the left (for volunteer 2) at equal intervals during the CEST acquisition. The speed of motion was intended to mimic small voluntary leg movements that a subject might make to adjust to a comfortable position during scanning. Before each CEST acquisition the scanner's shim was manually optimized. All the measurements were acquired in the transverse plane and the center slice of the navigator was aligned to the CEST slice.

## 4.3. Results

### 4.3.1. Assessing the effect of the vNavs on CEST and vice versa

Figure 4.3 demonstrates the effect of the navigator and CEST sequences on each another. The navigator curve (blue) shows the normalized signal intensity in a 35 x 35 x 5 $mm^3$ ROI on the pineapple as a function of different CEST offsets. The green and red lines are CEST and $MTR_{asym}$ curves for the CEST and DvNav-CEST acquisitions, respectively. The black dotted curve indicates the difference between the CEST curves acquired with and without the navigator.

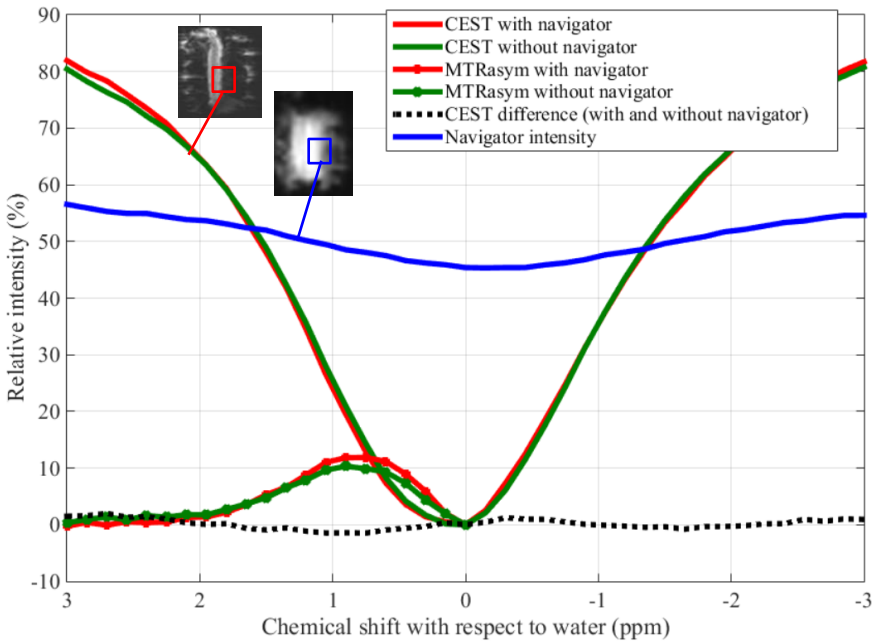


Figure 4.3: A plot showing how the navigator signal intensity (blue) in a pineapple phantom varies for different CEST offsets, as well as a comparison of CEST and $MTR_{asym}$ curves obtained from the standard CEST and DvNav-CEST (red) acquisitions, respectively. The black dotted curve indicates the difference between the CEST curves acquired with and without the navigator.

### 4.3.2. Assessing the effect of motion and $B_0$ inhomogeneity on CEST quantification

Figure 4.4 shows how motion (red curve) during the acquisition causes artifacts (evident here at 1.3 ppm and 1.8 ppm) that resemble the features expected in a CEST curve, as well as inaccurate CEST estimates (38.8% in the presence of motion compared to 23.3% in the absence of motion).

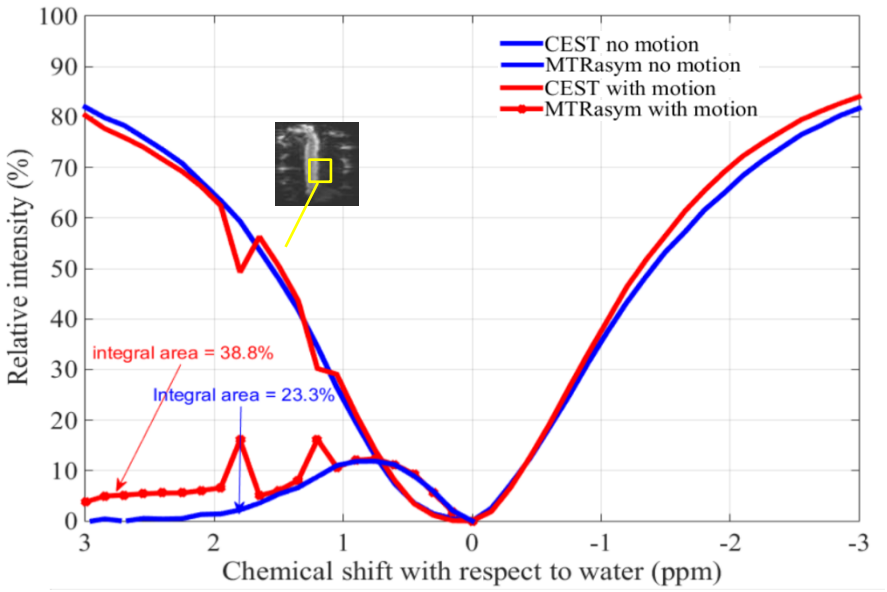


Figure 4.4: CEST and $MTR_{asym}$ curves for a pineapple phantom in the absence (blue) and presence (red) of motion. The peaks and dips in the $MTR_{asym}$ and CEST curves correspond to measurements when the pineapple was intentionally moved. The $MTR_{asym}$ curve was integrated between 0 and 3 ppm to compare CEST quantification.

Figure 4.5a show the $MTR_{asym}$ value at 1 ppm downfield of water for a 50mM glycogen phantom for various manual frequency adjustments both downfield and upfield of the scanner central frequency.

The $MTR_{asym}$ value at 0 ppm was acquired without any change to the system frequency. $MTR_{asym}$ values to the left of 0 ppm are from acquisitions where the system frequency was manually increased in 32 Hz intervals (~0.25 ppm at 3 T) and those on the right from acquisitions where it was manually decreased in 32 Hz (-0.25 ppm) intervals. Figure 4.5b shows the effect of linear gradient (Gx, Gy, Gz) changes on $MTR_{asym}$ values at 1 ppm.

### 4.3.3. Performance of the DvNavs in estimating and correcting zero- and first-order shim changes

Figure 4.6 shows geometric distortions and voxel shifts in the CEST reference images of a water phantom after manual adjustment of the system frequency and linear gradient values. For each acquisition, the top row shows the first CEST reference image (before shim correction), and the bottom row shows the second reference image acquired after shim correction by the DvNavs. Frequency shifts cause the image to shift in the phase encoding direction (Figure 4.6a), whereas gradient changes cause geometric distortions (Figure 4.6b). Figure 4.6c demonstrates how a frequency shift of -128 Hz introduces a Nyquist N/2 ghost in the CEST reference image that is minimized after frequency correction by the DvNavs.

Figure 4.7 shows good agreement between shim estimates computed by the DvNavs and known adjustments. Across all frequency shifts, the mean absolute estimation error was 0.23±0.15 Hz, with a maximum error of 0.45 Hz for a 32 Hz frequency change (Figure 4.7a). Additionally, we found that changes in the linear shim terms also caused global frequency changes, which could be correctly detected by the DvNav (Figure 4.7b). Each manual adjustment was performed after first resetting both the system frequency and linear-gradients to their optimal ("well shimmed") values.

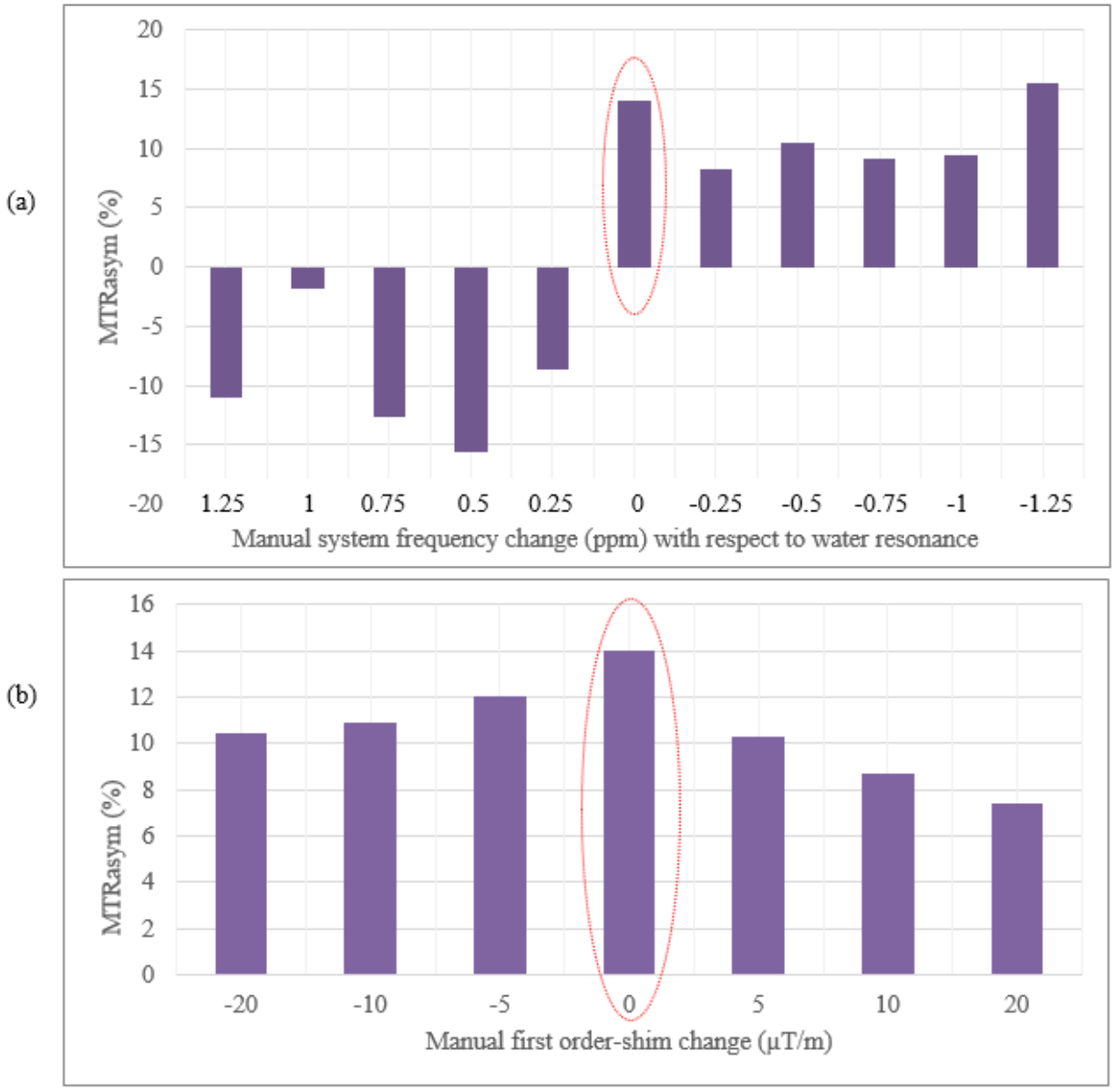


Figure 4.5: MTRasym at 1 ppm as a function of (a) zero-order (ΔF) shim change, and (b) first-order shim change (Gx, Gy, Gz) for a 50mM glycogen phantom. The value at 0 (circled) is without any manual adjustment and represents the true MTRasym value at 1ppm downfield of water

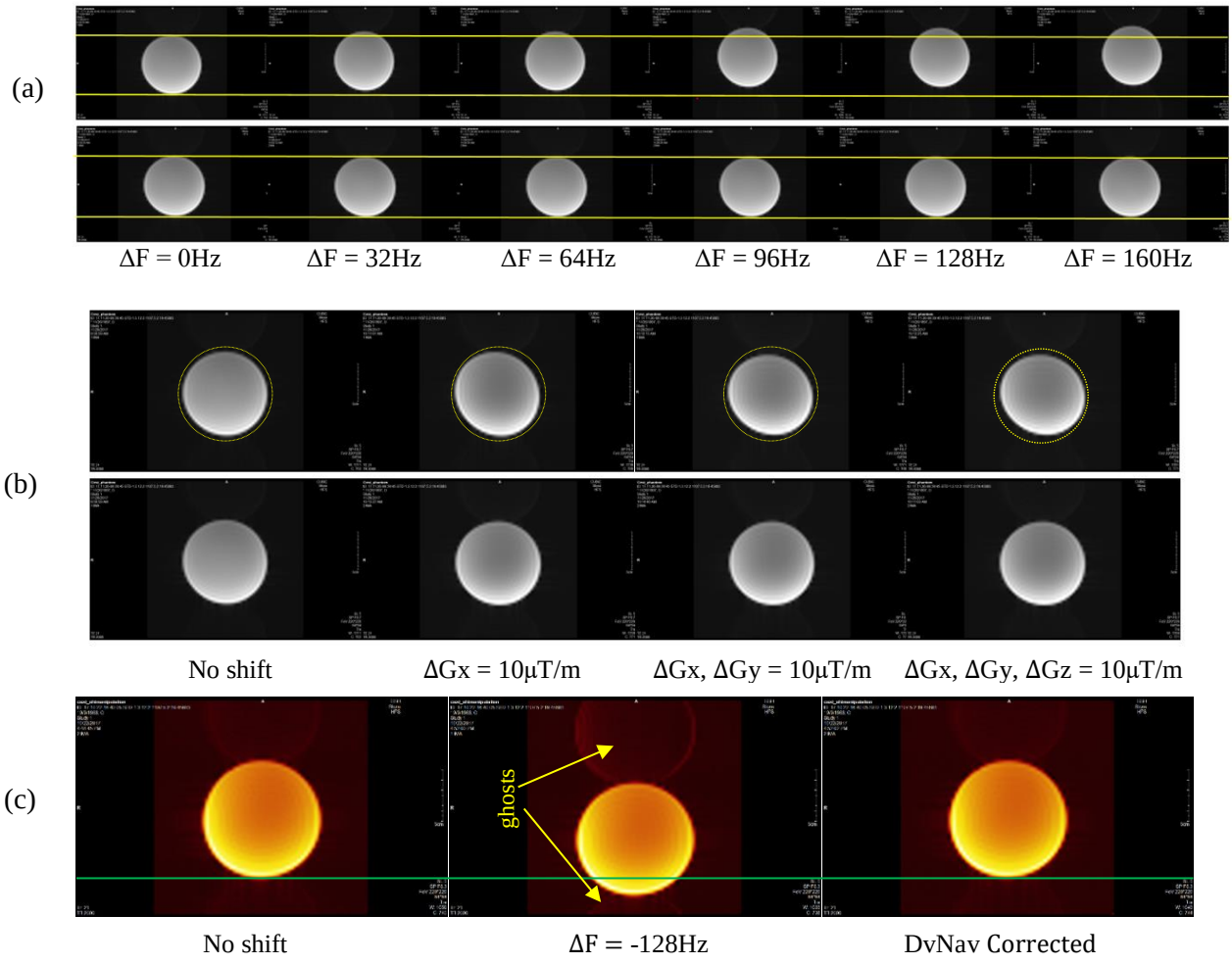


Figure 4.6: CEST reference images of a water phantom following (a) Zero-order and (b) first-order shim changes. In each case, the top row shows the reference image acquired after shim changes, and the second row the image acquired following shim correction by the DvNavs. (c) Illustration of the Nyquist N/2 ghost that is introduced by a -128 Hz frequency shift, and correction of the artifact by shim correction.

(a)

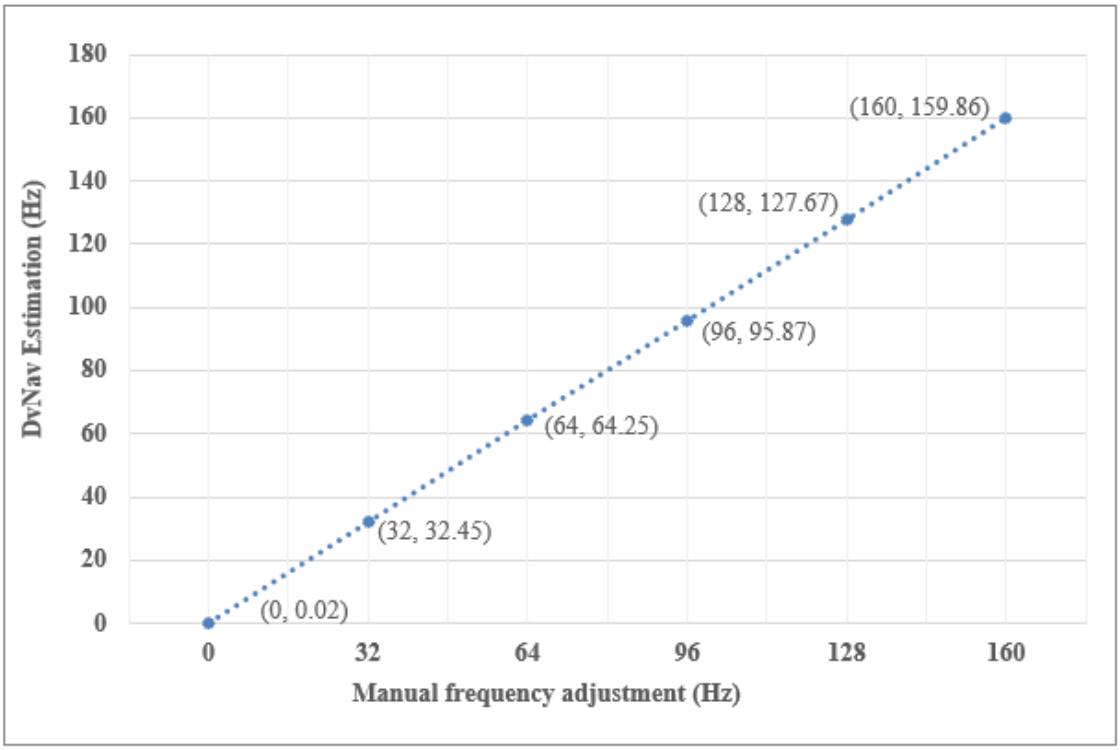


(b)

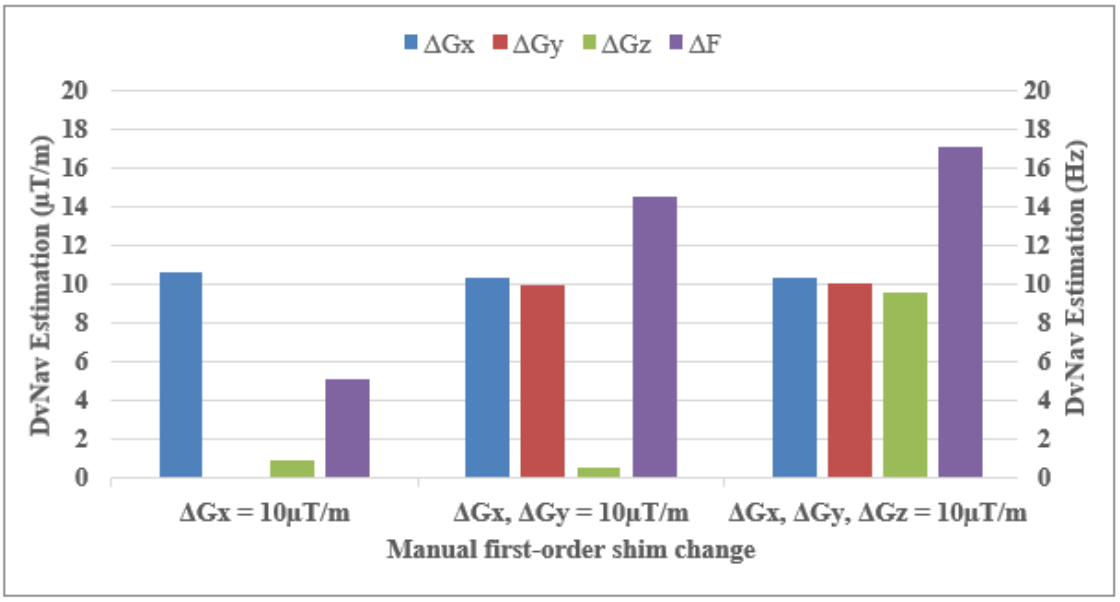


Figure 4.7: Comparison of (a) zero- and (b) first order shim changes computed by the DvNavs to known adjustments. The bottom plot also shows the effect of first-order shim changes on system frequency.

### 4.3.4. In vivo validation

Figure 4.8 shows the translation, rotation and shim parameters estimated by the DvNav for in vivo scans of 1 volunteer. In the motion corrected cases, the image FOV and shim are immediately adjusted when a change in position is detected. The coordinates of the current acquisition (including the DvNav) and shim are adjusted by the previously detected translation, rotation and shim parameters, respectively. This causes measured parameters in the prospectively-corrected case to resemble the derivative of these parameters in the non-corrected case.

Figure 4.9 shows the CEST and $MTR_{asym}$ curves from a 35 x 35 x 5 $mm^3$ ROI for the NoMo-NoCo, NoMo-AllCo, Mo-NoCo, Mo-MoCo and Mo-AllCo acquisitions of 1 volunteer. The uncorrected and incompletely corrected acquisitions with motion result in corrupted $MTR_{asym}$ curves. Table 1 compares the integral of the $MTR_{asym}$ curve between 0.5 and 1.5 ppm downfield of water, and peak values at 1 ppm, for the different acquisitions in each of the volunteers. Motion without correction or motion correction only result in inaccurate CEST quantification.

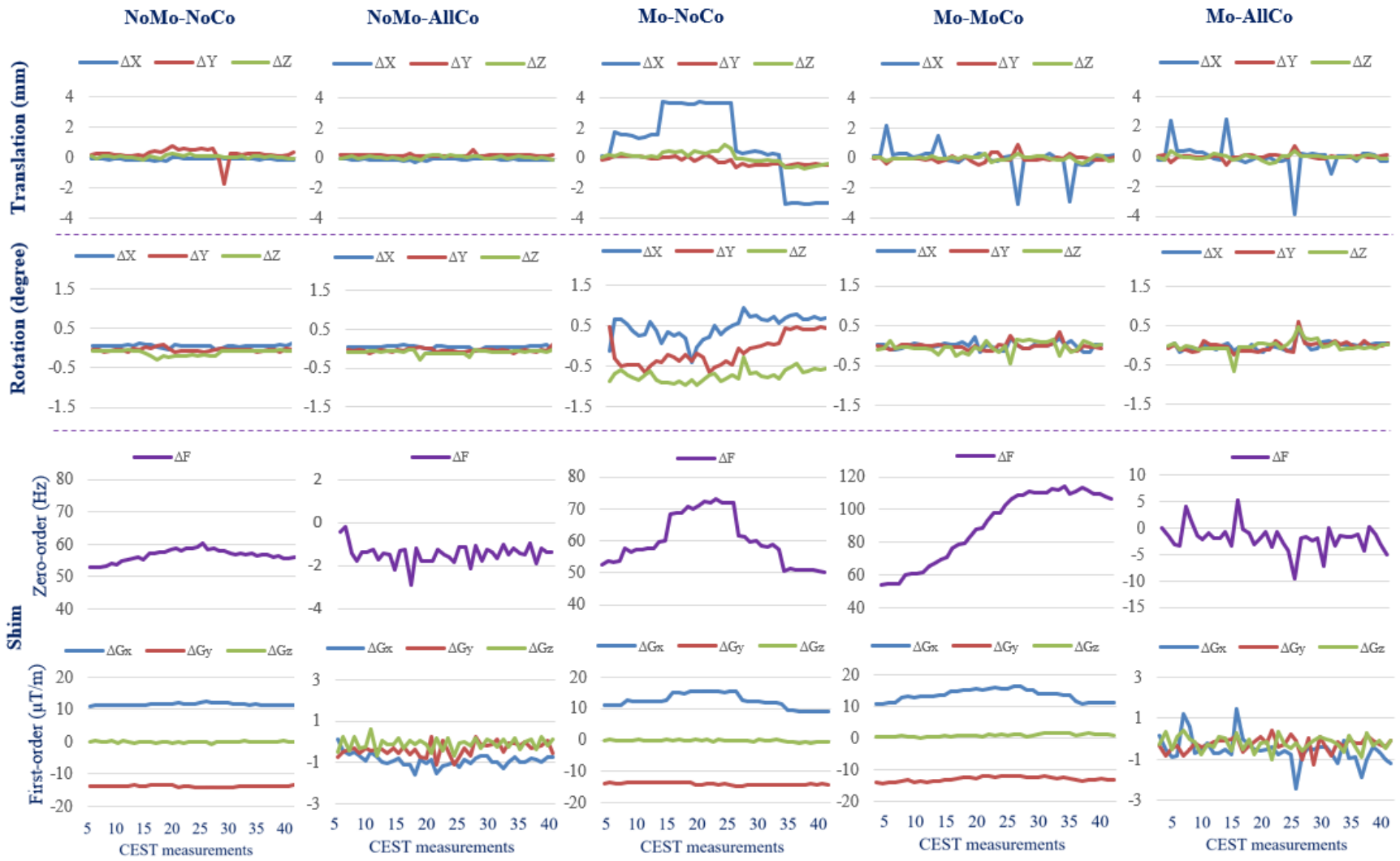


Figure 4.8: DvNav motion and shim estimates for NoMo-NoCo, NoMo-AllCo, Mo-NoCo, Mo-MoCo and Mo-AllCo acquisitions in one volunteer. The corrected plots demonstrate how the DvNav-CEST sequence adjusts the image FOV and shim parameters to correct for changes that occur due to motion. Top: Translation (mm), Middle: Rotation (degrees) and Bottom rows: Shim (zero-order and first-order). (NoMo = no motion, Mo = motion, NoCo = no correction, MoCo = motion correction only, AllCo = both shim and motion correction)

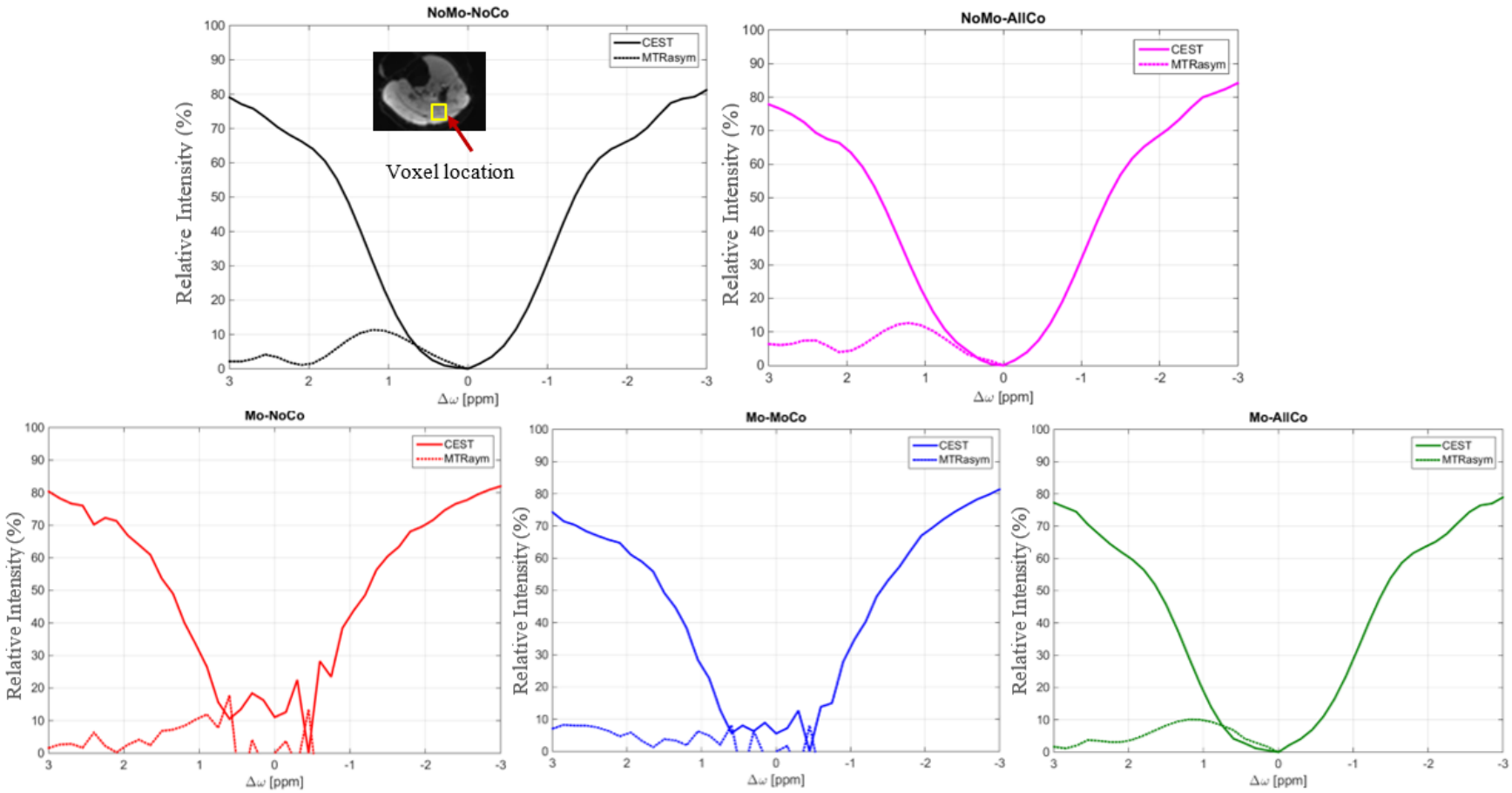


Figure 4.9: CEST spectra and MTRasym curves acquired in the calf muscle in one volunteer. **Top row:** (left) no motion and no correction (NoMo-NoCo); (right) no motion but with both shim and motion correction applied (NoMo-AllCo). **Bottom row:** (left to right) motion but no correction (Mo-NoCo), motion and motion correction only (Mo-MoCo), and motion and both shim and motion correction (Mo-AllCo).

| | Volunteer 1 | | Volunteer 2 | |
|---|---|---|---|---|
| **Scans** | **$MTR_{asym}$ peak (1ppm)** | **$MTR_{asym}$ integral (0.5 – 1.5 ppm)** | **$MTR_{asym}$ peak (1ppm)** | **$MTR_{asym}$ integral (0.5 – 1.5 ppm)** |
| **NoMo-NoCo** | 11.34 | 32.62 | 11. 90 | 38.66 |
| **NoMo-AllCo** | 12.14 | 34.21 | 14.64 | 41.80 |
| **Mo-NoCo** | 8.36 | 28.25 | 5.04 | 11.36 |
| **Mo-MoCo** | 1.94 | 12.42 | 5.35 | 15.37 |
| **Mo-AllCo** | 10.08 | 29.56 | 13.99 | 40.63 |

Table 4.1: Summary of $MTR_{asym}$ peak values at 1ppm and integrals between 0.5 - 1.5 ppm downfield of water for two volunteers during NoMo-NoCo, NoMo-AllCo, Mo-NoCo, Mo-MoCo and Mo-AllCo acquisitions.

## 4.4. Discussion

Although CEST MRI has emerged as a promising technique to detect molecules present in concentrations in the nanomolar to millimolar range, accurate analysis and quantification using remains challenging. Because the CEST spectrum is generated from multiple acquisitions with different saturation frequencies, it is prone to subject motion and heating of the iron shim coils because of eddy currents or mechanical vibrations, both of which can lead to significant fluctuation in the $B_0$ field (Benner et al., 2006, Clark et al., 2016, Foerster, Tomasi & Caparelli, 2005). Even after automatic shimming at the beginning of every acquisition, field homogeneity may change between measurements because of many unavoidable factors (Alhamud et al., 2016). The dependence of CEST on the chemical shift of endogenous molecules makes it especially sensitive to $B_0$ field inhomogeneity. This is exacerbated in glycoCEST where the resonance frequency of hydroxyl protons is very close to the water resonance (Kim, Mina et al., 2009). Effective shim correction is therefore essential for accurate quantification, particularly at 3 T.

Current CEST $B_0$ correction methods rely on data post-processing and require either a separate field map acquisition or multiple acquisitions with a fine frequency interval to correct the shift in the CEST spectrum caused by zero-order shim changes (Kim, Mina et al., 2009, Sun, Farrar & Sorensen, 2007). Motion correction is performed retrospectively via rigid (Schuenke et al., 2017)

or nonrigid (Muller-Lutz et al., 2015) registration of CEST offset-images. However, the CEST signal attenuation caused by geometric distortion because of gradient field variation cannot be corrected in this way. To our knowledge, no previous study has examined the effects of both motion and shim on CEST data analysis and quantification.

We have implemented fast double volumetric navigators in the CEST sequence to measure and correct shim changes and motion for each CEST frequency offset measurement. For each offset measurement, the motion and shim parameters are calculated and the FOV, frequency and gradient currents are updated for subsequent navigator and CEST measurements in real-time. This improves on existing correction methods by incorporating prospective correction, as well as the ability to report and correct changes in field inhomogeneity between different frequency offset measurements.

Placing the navigator immediately before the RF saturation pulse of the parent sequence is intended to minimize the signal saturation from the CEST sequence on the navigator. Accordingly, we observe a relatively stable navigator signal across the offset scans, with only a slight signal drop observed close to the water frequency, because of the residual saturation effect from the preceding CEST (Figure 4.3). The stable signal intensity over successive navigator images allows for accurate registration and motion estimation, whereas methods that attempt to correct for motion by registering CEST offset images (Li, Bian et al., 2017, Wech & Kostler, 2018) must address the challenge of registering images with varying contrast. Similarly, the small mean difference between CEST curves generated from acquisitions with and without the navigator confirms that the navigator's $2^0$ flip-angle RF excitation is sufficiently low not to affect CEST saturation.

Although it is difficult to absolutely quantify glycogen levels, relative quantification is possible using the $MTR_{asym}$ integral. For example, exercise-induced glycogen depletion can be examined using $MTR_{asym}$ measured before and after exercise, provided that all other conditions are identical between scans. However, a small change in intensity because of motion and $B_0$ variation may alter the $MTR_{asym}$ integral between 0 and 3 ppm downfield of water by up to 60% of its true value (Figure 4.4). Given the low MRI signal of endogenous molecules, even a small change in $MTR_{asym}$ has a large effect on data interpretation, and artifacts may resemble a metabolite of interest.

Our phantom results demonstrate the sensitivity of $MTR_{asym}$ values to slight zero-order shim changes. As the frequency of the saturation pulse shifts away from the expected glycogen resonance, saturation of glycogen protons decreases and hence also the indirect saturation of the water signal because of proton transfer. Changes in linear gradients also affect $MTR_{asym}$, possibly because of intensity variation resulting from geometric distortion and phase encoding shifts. The pattern of artefactual changes in $MTR_{asym}$ as a function of shim variation is not deterministic but Figure 4.5 demonstrates the substantial effect of small variations in zero- and first-order shim.

The CEST-DvNav sequence accurately detects, measures and corrects the change in $B_0$ following manual adjustment of the scanner system frequency (zero-order shim) and the linear gradients (first-order shim). A change in zero-order shim results in a shift of the volume image in the phase encoding direction, and a visible phase wraparound (Nyquist N/2 ghost) artifact, especially for larger zero-order shim changes (Figure 4.6). This causes misregistration of voxels from consecutive offset volumes, in addition to a shift in offset frequency in the CEST-spectrum. These artifacts, as well as geometric distortions and intensity variations caused by varying linear shim gradients (particularly apparent when more than 1 shim term is adjusted) are corrected by the DvNav. Because variations in $B_0$ can result in misinterpretation during voxel-wise CEST analysis, for accuracy it is important that $\Delta B_0$ be corrected in each CEST offset volume acquisition.

In our in vivo test, the relatively stable zero and first-order shims are distorted directly after pose changes during acquisitions with motion but no correction (Figure 4.8). Without correction, the frequency increases and/or decreases as pose changes with respect to the initial frequency and returns towards its initial value upon return to the initial pose. Both pose changes and shim distortions are corrected when shim and motion correction are applied using the DvNav-CEST sequence (Figure 4.8: Mo-AllCo). Because of motion, a gradient change of about 5 μT/m (uncorrected case) and 4 μT/m (corrected case peak to peak) occurred in $G_x$ (excluding the initial shim offsets), which is a significant amount to alter the CEST effect (as demonstrated in Figure 4.5).

Although a single vNav can correct a subject's pose change, it cannot correct the resultant offset shifts in the CEST-spectrum and yields corrupted CEST and $MTR_{asym}$ curves (Mo-MoCo). In contrast, motion- and shim-corrected (AllCo) CEST-spectra and $MTR_{asym}$ curves both without and with motion are in good agreement with the NoMo-NoCo baseline scan (Figure 4.9). Although the

$MTR_{asym}$ integral and peak values between 0.5 and 1.5 ppm downfield of water for both volunteers are substantially reduced in scans with motion and either no correction (Mo-NoCo) or motion correction only (Mo-MoCo), values are similar for scans without motion (NoMo) –both with and without correction and for scans with motion and both shim and motion correction (Mo-AllCo). This highlights the importance of correcting both motion and shim to achieve accurate CEST quantification in the presence of motion.

Recent similar work has included volumetric navigators to correct for motion in glutamate CEST at 7T (Auno, 2018). However, motion correction was only effective for motion < 0.7 mm/$0.7^0$. By contrast the PACE estimation method used here is potentially effective for translations and/or rotations of up to 20 mm/$8^0$ (Thesen et al., 2000). We have demonstrated effective motion correction for up to 7 mm transition and 2 degrees rotation. Although the $B_0$ field was corrected retrospectively in Auno (Auno, 2018) using the dual echo of the CEST sequence, and receiver sensitivity using the vNav intensity, the current implementation corrects $B_0$ prospectively in real-time without additional scanning time.

Very few studies have attempted glycoCEST in humans at 3 T as motion of organs, and $B_0$ spatial inhomogeneity and temporal changes present a challenge to quantification. One study has demonstrated liver glycogen reduction after fasting (Deng et al., 2016b). Another has shown that muscle glycogen can be assessed at 3 T with proper frequency correction using the WASSR method (Kim, Mina et al., 2009). The DvNav-based prospective frequency and first order shim measurement and correction presented here could improve accuracy of muscle glycogen CEST measurements. Even with minimal motion, the proposed method would correct any drift in the scanner center frequency that occurs during the CEST acquisition (Windschuh et al., 2018).

A limitation of this work is that reproducibility of the CEST measurements obtained with the DvNav sequence was not evaluated. This will be addressed in future work. We also did not quantify the incremental benefit of linear shim correction above frequency correction alone.

## 4.5. Conclusion

Given that endogenous CEST imaging contrasts are only a few percent, even small errors significantly impact CEST data analysis and quantification. Field inhomogeneity is unavoidable and may occur during a scan because of heating of the shim iron, subject motion and other factors.

We have presented a technique that accurately detects, measures and corrects changes in the $B_0$ field using DvNavs. Our method was shown to decrease the effects of subject motion and field inhomogeneity by simultaneously correcting for both in real-time with no additional scanning time. Phantom and in vivo test results show improved CEST quantification in the presence of motion and field variations. Although the method was demonstrated for glycogen, which is more sensitive to field inhomogeneity than other metabolites because of its resonance being close to that of water, it can be extended to other metabolites detectable with CEST-MRI.

## 4.6. Acknowledgements

Resources necessary for the study were provided by Athinoula A. Martinos Center for Biomedical Imaging/Massachusetts General Hospital, University of Cape Town Medical Imaging Research Unit and Cape Universities Body Imaging Centre. The study was supported by the University of Cape Town international travel award, NRF/DST South African Research Chairs Initiative, NRF Thuthuka grant TTK 150612119380, and NIH grants R01HD071664, R01HD085813, R21MH108346.

# Chapter 5

## Reproducibility study of glycoCEST MRI using a motion and shim navigated 2D EPI CEST sequence[1]

Gizeaddis L. Simegn[2], Ali Alhamud[2,3], Andre J.W. Van der Kouwe[2,4,5] , Ernesta Meintjes[2,3], and Frances Robertson[2,3]

## Abstract

The effectiveness of CEST MRI for detecting macromolecules *in vivo* depends on several factors including body temperature, pH, the prepared static shimmed $B_0$ and other experimental parameters. Repeated measurements on the same subject should produce similar results under the same environmental and experimental conditions. However, fluctuation in the static prepared $B_0$ field, which may occur between measurements due to heating of the iron shim coils or subject motion, may alter CEST results and affect reproducibility. The aim of this study was to investigate the reproducibility of CEST measurements from consecutive acquisitions and to examine the effectiveness of using a navigated CEST sequence with real-time shim and motion correction to improve reproducibility. Nine healthy subjects were scanned on the calf muscle. For every subject, five CEST scans were acquired in each of two sessions, in the first without shim correction applied, and in the second with shim correction applied. In both sessions a 5-minute gradient intensive diffusion sequence was run to introduce a dynamically changing field as a result of coil heating. Tests were performed to evaluate the effect of the introduced $B_0$ inhomogeneity on the reproducibility of glycogen CEST, where the small chemical shift difference between the hydroxyl protons and bulk water protons at 3 T makes CEST quantification extremely sensitive to magnetic field inhomogeneities. With shim correction applied**,** CEST results were relatively consistent with mean coefficient of variation (CoV) of 2.67 ± 1.37 % across all subjects, whereas without correction the results were less consistent with CoV of 83.70 ± 70.79 %. Our results demonstrate that the fluctuation in the $B_0$ field affects reproducibility of CEST data and that the navigated CEST

[1] Chapter written as an article intended for review and publication

[2] *UCT Medical Imaging Research Unit, Division of Biomedical Engineering, Department of Human Biology, University of Cape Town, Cape Town, South Africa*

[3] *Cape Universities Body Imaging Centre (CUBIC-UCT), Cape Town, South Africa*

[4] *Athinoula A. Martinos Center for Biomedical imaging/MGH, Charlestown, MA, United States*

[5] *Department of Radiology, Harvard Medical School, Boston, MA, United States*

sequence produces more reproducible measurements. This is important when conducting longitudinal studies or when using CEST MRI to assess treatment or physiological responses over time.

**Keywords:** Reproducibility, glycoCEST, field inhomogeneity, DvNav-CEST sequence, Shim correction

## 5.1. Introduction

Chemical exchange saturation transfer (CEST) is a relatively new MRI contrast method that allows for indirect detection of low concentration metabolite pools bearing exchangeable protons through the large exchange-mediating water proton pool (Khlebnikov et al., 2017, Sun, van Zijl & Zhou, 2005, Zaiss, M. & Bachert, P., 2013, Zhou, Jinyuan et al., 2004, Zijl. & Yadav, 2011).

CEST imaging provides a more specific means to probe tissue composition compared with conventional MRI through the exchange of specific labile protons that are generally not detectable with standard MRI methods. However, the magnitude of the CEST effect is typically a few percent, and therefore, it is important to improve its sensitivity by optimizing acquisition parameters. The effectiveness of CEST to indirectly detect specific macromolecules *in vivo* depends on both acquisition parameters and physiological factors (Wu, B. et al., 2016). These can be optimized prior to the CEST scan, by selecting values that maximize signal reduction from the specific molecule of interest (see chapter 3).

Field homogeneity can be distorted by several factors including subject motion (Pfeuffer et al., 2002, Ward, Heidi A., Riederer & Jack, 2002) and heating of the iron plates in the shim trays by eddy currents and mechanical vibrations (Benner et al., 2006, Foerster, Tomasi & Caparelli, 2005) during measurement. Since CEST imaging is based on chemical shift difference of metabolites from water, it is extremely sensitive to field fluctuation. Small variations in the field may strongly impact the apparent CEST effects due to interference of direct saturation effects that have a strong frequency dependence, especially when in close proximity to the water signal (Liu et al., 2010), as in the case of glycogen.

The degree of field inhomogeneity, and therefore its effect, may vary within a CEST scan, from offset measurement to measurement, and scan to scan making CEST measurement unreliable during studies that require multiple rounds of CEST scan repetitions, such as pre- and post-exercise

glycogen depletion and repletion studies, perfusion studies (Pekar et al., 1996, Yeung & Aisen, 1992), and assessment of glucose metabolism using CEST MRI (GlucoCEST) in the brain (Nasrallah et al., 2013) (Jin et al., 2014).

Repeatability of measurements refers to the variation in repeated measurements made on the same subject under identical conditions, using the same instrument or method, and over a short time period during which the measured value is assumed to be constant. Variability in such cases therefore results only from measurement itself (Bartlett & Frost, 2008). Reproducibility refers to the variation in measurements made on a subject under changing conditions (Bartlett & Frost, 2008, Casadevall & Fang, 2010, Crook, Davison & Plesser, 2013), which may be different measurement methods, different observers or measurements being made over a period of time.

Under constant experimental conditions CEST offset measurements for the same subject should be repeatable. To be of practical use, measurements in different sessions should also be reproducible, that is robust to instrument-related or environmental variations besides that of the CEST effect itself. Any differences in the CEST data should therefore reflect only physiological variations.

A motion and shim navigated CEST sequence (Simegn et al., 2018)has recently been introduced and shown to decrease the effects of subject motion and field inhomogeneity by simultaneously correcting for both in real-time. To date, the effect of field inhomogeneity on the reproducibility of CEST data has not been assessed. This work examines the effect of field inhomogeneity on the reproducibility of *in vivo* glycoCEST acquisition and evaluates the effectiveness of our navigated CEST sequence with dynamic shim and motion correction in producing more repeatable results.

## 5.2. Methods

### 5.2.1. Data Acquisition

All scans were performed on a Skyra 3 T MRI scanner (Siemens, Erlangen, Germany) using a 15-channel Tx/Rx knee coil according to protocols that had been approved by the Human Research Ethics Committee of the Faculty of Health Sciences, University of Cape Town. Written informed consent was obtained from all volunteers.

Nine healthy subjects (7 male and 2 females; age: 23 - 38) were recruited for the study. The calf muscle of each subject was scanned 5 times in each of two sessions. In the first session – set of 5

scans - shim correction was not applied, and in the second both shim and motion correction were applied, to evaluate the reproducibility of the CEST sequence in each case. Between the two sessions there was a short pause in scanning, but the subject was not removed from the scanner. During all scans, subjects were instructed to lie still. In addition, the leg was immobilized using foam padding. A Diffusion Tensor Imaging (DTI) sequence with a duration of five minutes was run in between the third and fourth CEST scans for 7 subjects, and before all scans for the remaining 2 subjects to introduce a dynamically changing field during the remaining scans subsequent to heating induced by the gradient-intensive diffusion scan, and to evaluate the effect of this shim change on the reproducibility of the CEST scans. The DTI sequence can cause field drift to up to 30Hz due to heating of the shim iron (Alhamud et al., 2016) and mechanical vibration (Alhamud et al., 2016, Avram et al., 2014, Bodammer et al., 2004, Truong, Chen & Song, 2008).

### 5.2.2. Scanning Protocols

A 2D gradient echo single-shot echo planar imaging (ss-EPI) continues wave (CW) CEST sequence optimized with Double Volumetric Navigators (DvNav-CEST) for real-time shim and motion correction (Simegn et al., 2018) was used for this study. The CEST imaging parameters were: TR = 2000 ms; TE = 21 ms; FOV = 256 × 256 $mm^2$; pixel size = 4 × 4 $mm^2$; slice thickness = 5 mm; 43 offset measurements (including 2 reference unsaturated measurements) acquired with an optimized RF power of 1.5 µT and saturation pulse duration 1000 ms swept between -3 to 3 ppm (with respect to water) with an interval of 0.15. The DvNav parameters were: TR=13 ms, $TE_1$ = 4.8 ms and $TE_2$ = 7.0 ms, acquisition matrix of 32 x 32 x 32, 8 mm isotropic voxels (with 6/8 partial Fourier encoding in the slice direction), FOV 256 mm, turbo factor 32, $2^0$ flip angle and bandwidth 4882 Hz/px. A 2.2 ms echo time difference (ΔTE) was chosen to maintain fat and water in phase. The total data acquisition time, including the navigator, was 1 min and 30 seconds. Volunteers were instructed to maintain their position during the whole acquisition.

### 5.2.3. Data analysis

For each subject a 35x35x5 $mm^3$ region of interest (ROI) was manually selected from the largest muscle group (gastrocnemius) in the calf (Figure 5.1) for glycoCEST analysis. Consistent placement between subjects was achieved by visual comparison. Since there was assumed to be minimal displacement between scans of one subject, within each subject the identical ROI positioning was used for all scans. A custom-written Matlab (MathWorks, Inc 2014) program was

used to process all the images and generate CEST spectra and $MTR_{asym}$ curves. The $MTR_{asym}$ curve was generated by subtracting the intensity of CEST spectra down field of water (positive offset frequencies) from that upfield of water (negative offset frequencies). For all acquisitions, the $MTR_{asym}$ integral was calculated between 0.5 – 1.5 ppm downfield of water, targeting glycogen.

For comparison to the navigator based real-time shim correction, a polynomial fitting field inhomogeneity correction method (Zhou, Jinyuan et al., 2003, Zhou, J. et al., 2008) was used to correct CEST spectra acquired from the 8$^{th}$ subject during the shim-uncorrected session. CEST spectra were fitted to a 12$^{th}$ order polynomial, and the frequency corresponding to the lowest signal intensity in the fitted spectra was assumed to be water resonance frequency. All spectra were shifted accordingly in order to correct field inhomogeneity shift effects.

The standard deviation and coefficient of variation (CoV) of the $MTR_{asym}$ integral for scans within a session were calculated for each subject and session to compare reproducibility between sessions with and without shim correction. CoV for each subject *i* and session *j* was calculated as follows:

$$CoV_{i,j}\ (\%)\ = \frac{\sigma_{i,j}}{\mu_{i,j}} \text{ x } 100 \quad \text{..... [5.1]}$$

where σ and μ are the standard deviation and means respectively of *n* scans in session *j*. To investigate measurement repeatability, the CoV was calculated over the first 3 pre-DTI scans (*n* = 3), and to investigate the reproducibility under the changing shim conditions CoV was calculated over all scans in each session (*n* = 5). To investigate inter-session variations (the effect of introducing shim correction), the Pearson correlation coefficient of the session mean $MTR_{asym}$ integral (*n* = 3) for each subject was calculated between sessions with and without shim correction. The inter-subject CoV was calculated as the ratio of the SD of subject $MTR_{asym}$ means to the mean of the subject $MTR_{asym}$ means. The measured shim parameters for all scans were analyzed in Microsoft Excel.

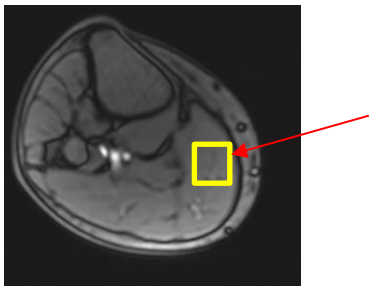


Figure 5.1*:* Location of selected ROI used for CEST analysis

## 5.3. Results

A total of 90 CEST spectra and $MTR_{asym}$ curves (9 subjects x 5 scans x 2 sessions) were generated and analyzed. Figure 5.2 shows the CEST and $MTR_{asym}$ curves for the first 3 subjects with and without shim correction.

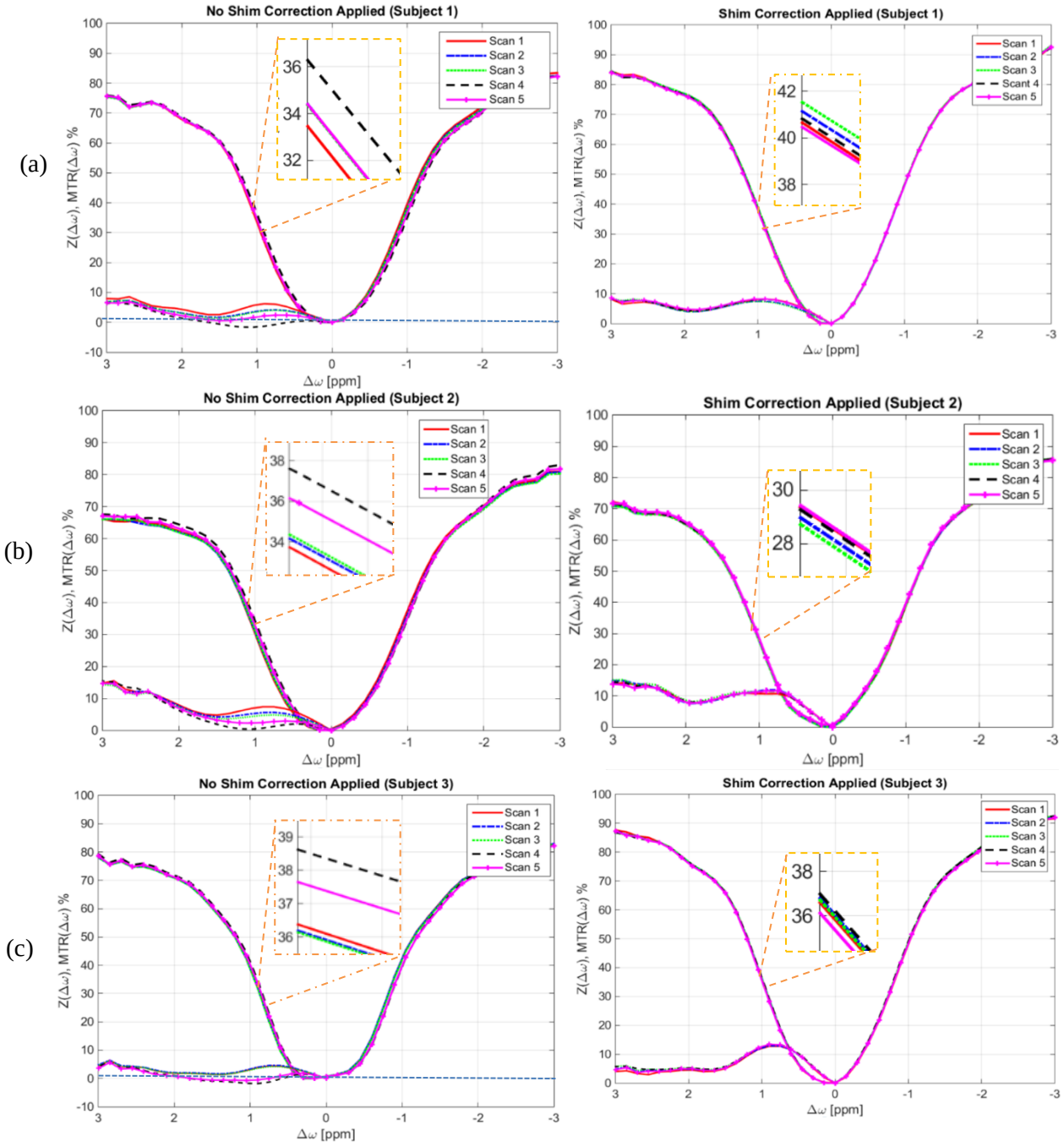


Figure 5.2: CEST spectra and $MTR_{asym}$ curves for three subjects (a), (b) and (c) the DTI was run in between the third and fourth scans. All scans were repeated five times in each of the two sessions (left: no shim correction applied, right: shim correction applied).

For the remaining two subjects the 5-minute DTI scanning was performed prior to the CEST acquisitions in both shim uncorrected and corrected cases. This is shown in Figure 5.3 where after the DTI in the shim uncorrected case a reduction in signal intensity, resulting in flatter CEST spectra with broadening around 0 ppm and spectral shifts, are observed in the first scans directly after DTI in the shim uncorrected case. This causes distortion of the $MTR_{asym}$ curve, which is particularly severe in the first scan after DTI. On the other hand, consistent intensities are observed in the shim corrected cases. Post-processing with a high-order polynomial to correct a shift in the CEST spectrum is shown for comparison.

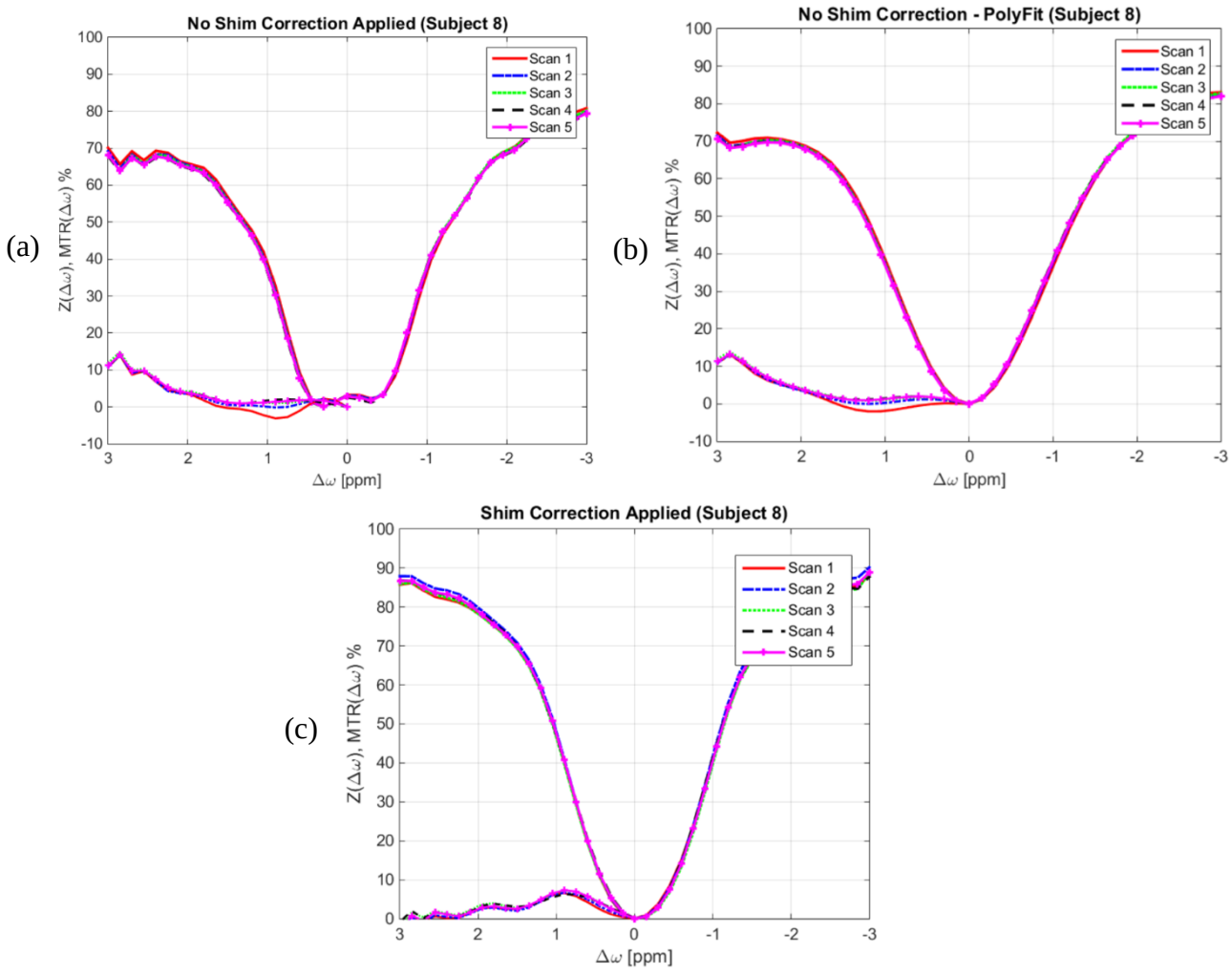


Figure 5.3: CEST Spectra and $MTR_{asym}$ curves from 5 CEST scans in a single subject all obtained after a 5-minute DTI scan. The top left panel shows curves obtained from session without shim correction while the right panel shows curves obtained after spectral shift correction using high-order polynomial fitting technique. Bottom panel shows curves obtained from CEST acquisitions with shim correction applied. The polynomial fitting technique failed to recover the reduction in $MTR_{asym}$ integral due to shim distortion.

Figure 5.4 shows the shim parameters (zero-order and first-order) measured for a single subject acquired during scans before the DTI sequence (3rd scan) and after the DTI sequence (4th scan) during the two sessions, demonstrating how the gradient intensive DTI sequence alters the scanner field.

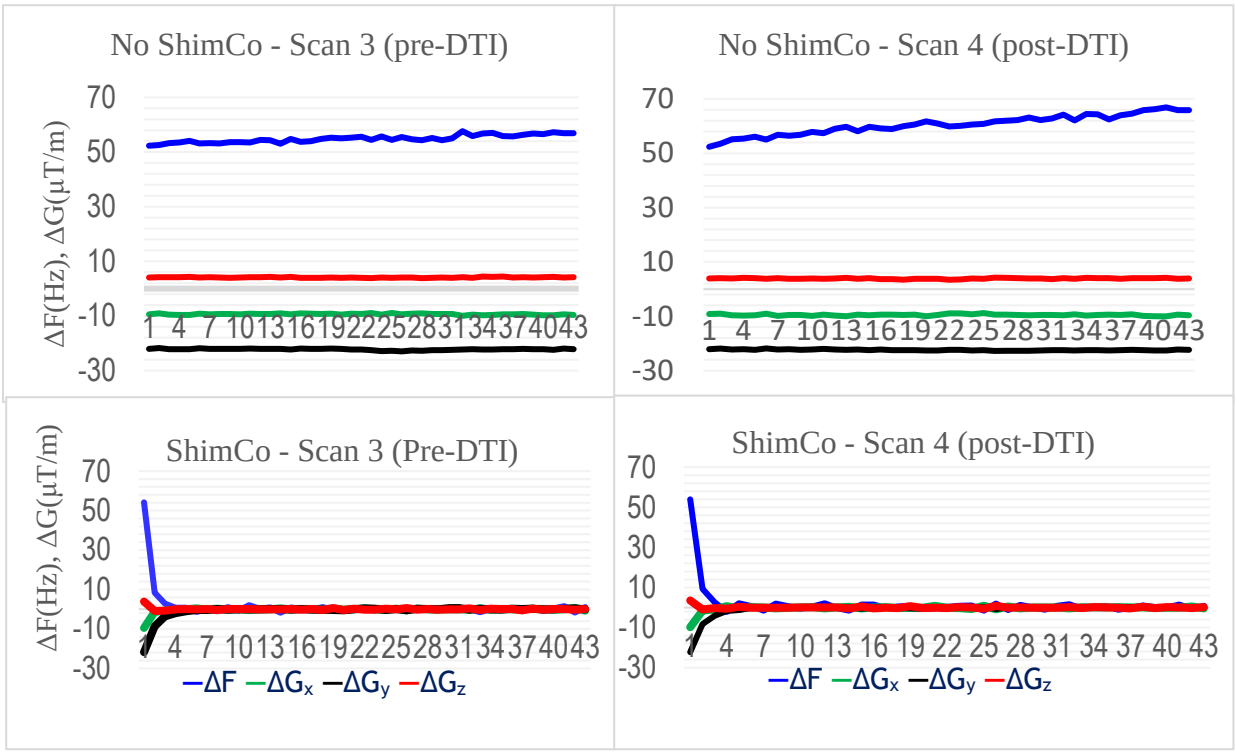


Figure 5.4:Measured shim parameters for a single subject; Scan 3 (pre-DTI), Scan 4 (post-DTI). The top row shows shim parameters for the scans acquired without shim correction, while the bottom row shows shim parameters for the scans acquired with shim correction applied. A frequency drift of approximately 10Hz/min is observed in scans acquired immediately after DTI.

Figure 5.5a shows a plot of the MTRasym integral for consecutive scans, demonstrating relatively more consistent values for scans acquired with shim correction applied than for those acquired without shim correction. Distinct alterations in MTRasym integral are evident for post-DTI CEST scans (scans 4 and 5). Figure 5.5b shows the MTRasym integral for two volunteers acquired in two sessions post-DTI, where the first scan is most affected by the preceding DTI, followed by a gradual increase in MTRasym.

(a)

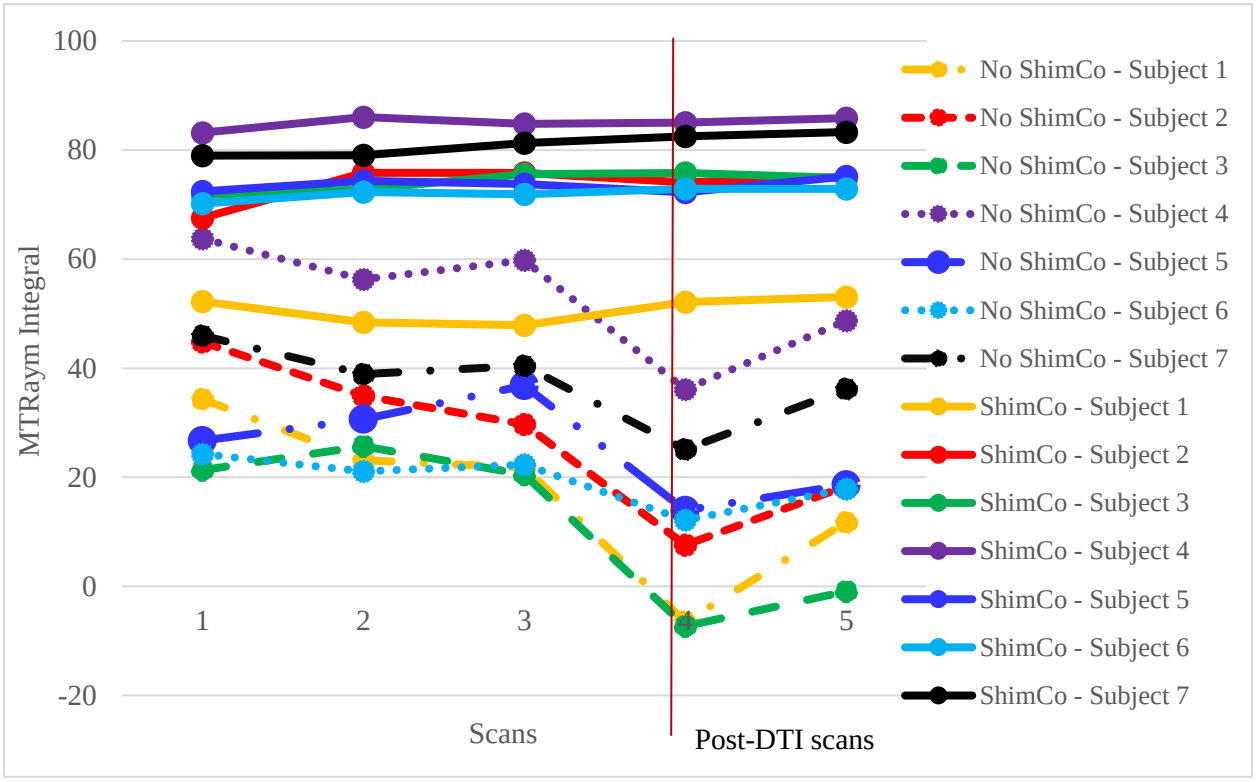


(b)

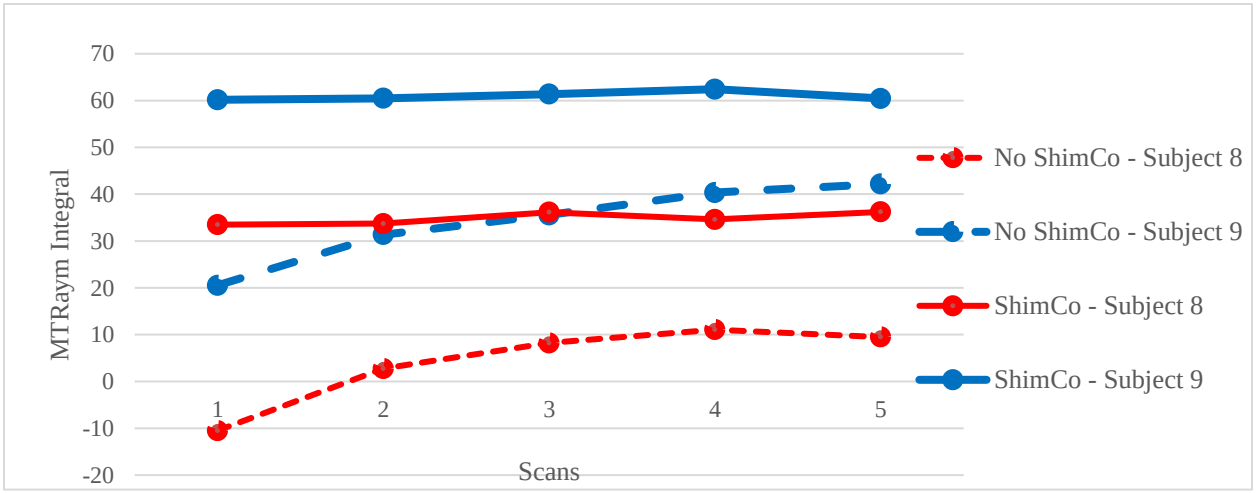


Figure 5.5: $MTR_{asym}$ integral for each volunteer of five consecutive scans acquired in session 1 without shim correction (No ShimCo) and in session 2 with shim correction applied (ShimCo). In (a) for subject 1-7 the DTI sequence was run between 3rd and 4th CEST scans while for the volunteers 8&9 shown in (b) all scans in both sessions were acquired post-DTI.

Table 5.1 shows Coefficient of variation (CoV) and standard deviation (Std) of the $MTR_{asym}$ integral for the 5 consecutive scans acquired in uncorrected and shim-corrected scans for all subjects. Table 5.2 shows the same, but only for the 3 scans acquired prior to DTI (i.e. without deliberate introduction of $B_0$ changes) for 7 subjects. For comparison Table 5.3 shows the reproducibility of the $MTR_{asym}$ integral for a single subject (subject 8) without shim correction, with real-time shim correction and with shim correction by postprocessing using a polynomial fitting method only.

| | Coefficient of Variation (CoV) | | Standard deviation (Std) | |
|---|---|---|---|---|
| Volunteer | No ShimCo | ShimCo | No shim Correction | Shim Corrected |
| 1 | 90.74 | 4.74 | 15.33 | 2.40 |
| 2 | 53.44 | 4.74 | 14.47 | 3.49 |
| 3 | 125.65 | 2.43 | 14.88 | 1.80 |
| 4 | 20.60 | 1.33 | 10.90 | 1.13 |
| 5 | 36.18 | 1.70 | 9.17 | 1.25 |
| 6 | 24.25 | 1.54 | 4.73 | 1.11 |
| 7 | 20.63 | 2.41 | 7.7 | 1.95 |
| 8 | 208.67 | 3.71 | 8.79 | 1.29 |
| 9 | 173.15 | 1.51 | 8.62 | 0.92 |

Table 5.1: Measures of $MTR_{asym}$ integral reproducibility calculated over 5 consecutive scans acquired from 9 subjects without shim correction and with shim correction applied.

| | CoV | | Std. | |
|---|---|---|---|---|
| Volunteer | No ShimCo | ShimCo | No ShimCo | ShimCo |
| 1 | 26.08 | 4.80 | 6.88 | 2.38 |
| 2 | 21.02 | 6.53 | 7.67 | 4.77 |
| 3 | 12.42 | 2.72 | 2.79 | 1.99 |
| 4 | 6.21 | 1.69 | 3.72 | 1.43 |
| 5 | 16.17 | 1.36 | 5.07 | 1.0 |
| 6 | 7.15 | 1.57 | 1.61 | 1.12 |
| 7 | 8.89 | 1.61 | 3.71 | 1.29 |

Table 5.2: Measures of $MTR_{asym}$ integral reproducibility calculated for the first 3 (pre-DTI) scans acquired from 7 subjects without shim correction and with shim correction applied

| | CoV | Std. |
|---|---|---|
| No Shim Correction | 208.67 | 8.79 |
| Shim Corrected | 3.71 | 1.29 |
| PolyFit | 173.15 | 8.27 |

Table 5.3: $MTR_{asym}$ integral reproducibility calculated from 5 CEST acquisitions in a single volunteer all obtained after a 5 minute DTI scan without shim correction, with real-time shim correction applied and after correction by a $12^{th}$ order polynomial fitting technique (PolyFit).

Between subject CoV of the mean $MTR_{asym}$ integral for the No ShimCo session is 38.71 % and for the ShimCo session it is 15.30 %.

The mean $MTR_{asym}$ integral across the first 3 consecutive scans for each subject in shim uncorrected and shim corrected sessions is shown in Figure 5.6. In uncorrected scans the $MTR_{asym}$ integral appears to be underestimated relative to corrected scans. However, a correlation of $r$ = 0.62, $p$ = 0.1 is observed between average values acquired in each session.

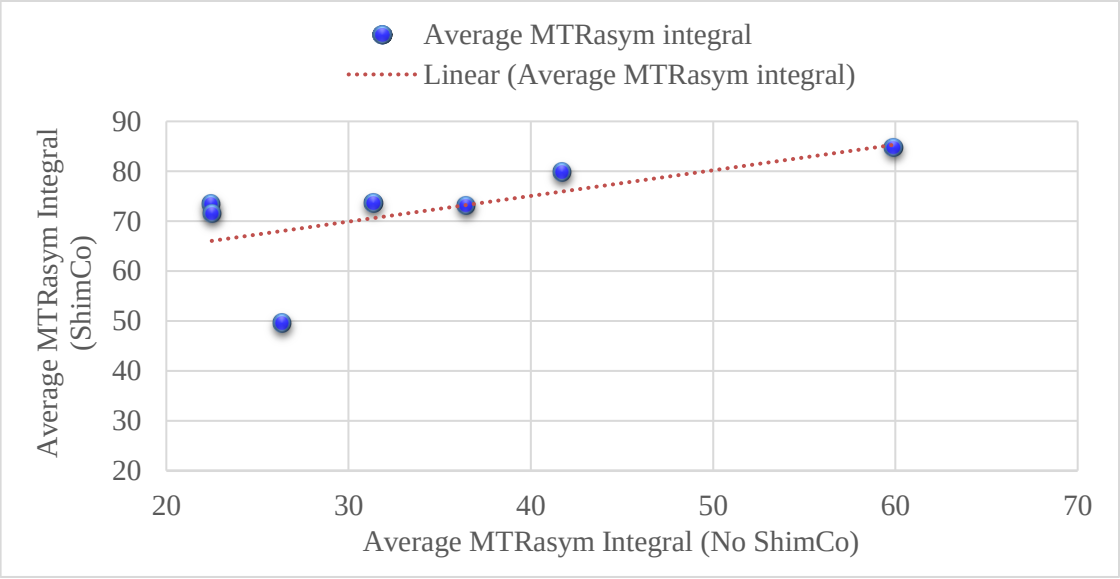


Figure *5.6*: Scatter plot of Average $MTR_{asym}$ integral for 3 consecutive scans (Pre-DTI) of each subject acquired without shim correction and with shim correction applied. A reduction in $MTR_{asym}$ integral is observed for all uncorrected scans compared to shim corrected scans. Correlation between No ShimCo and ShimCo measurements is $r$ = 0.62, $p$ = 0.1.

## 5.4. Discussion

CEST MRI is a promising technique to detect metabolites, including glycogen, that are difficult to observe using standard MRI techniques due to their low concentrations. However, CEST imaging is complex, due to its dependence on physical and physiological parameters (Zaiss, M. & Bachert, P., 2013). Moreover, the strong dependence of CEST on the magnetic field affects the parameters of radiofrequency irradiation for selective CEST saturation and complicates interpretation of acquired signals. $B_0$ field inhomogeneities lead to a distortion in the acquired images and a shift in the water resonance frequency that results in asymmetric direct water saturation effects. This introduces artificial CEST effects in asymmetry analysis (Kogan, Hariharan & Reddy, 2013). Due to a very small frequency separation from water, hydroxyl groups are particularly sensitive to fluctuations in field homogeneity, where a small change in system frequency leads to direct saturation effects and decreases the sensitivity of CEST.

Studies using CEST MRI typically employ multiple scanning sessions to examine changes in physiology, biochemistry (e.g. pH) (Sun & Sorensen, 2008), molecular composition (Haris et al., 2013), metabolism (e.g. muscle glycogen depletion and repletion), and perfusion (Anemone, Consolino & Longo, 2017, Haris et al., 2011). For accurate and reproducible results, all experimental and physical parameters should ideally be kept constant. However, changes in field homogeneity may occur between measurements as a result of instrumental factors (e.g. heating of shim coils) and subject-related factors (small motions, such as respiration), causing inconsistencies in the acquired data. Technological improvements that address some of these issues will improve the practical utility of CEST imaging. We previously introduced a navigated CEST sequence (DvNav-CEST) for real-time motion and shim correction and demonstrated how it corrected CEST measurements that were corrupted due to motion (Simegn et al., 2018). In the current work, we investigated the reproducibility of glycoCEST MRI, under different consecutive scanning scenarios using the both standard and DvNav-CEST sequence.

Without correction CEST spectra and $MTR_{asym}$ curves were distorted, particularly for scans acquired after DTI (Figure 5.2 and Figure 5.3) where the $MTR_{asym}$ curve even dipped below zero. This is due to slight changes in frequency and linear gradient shim causing saturation asymmetry between corresponding offset measurements. As a result, for shim-uncorrected scans in all subjects, the $MTR_{asym}$ integral was reduced in the $4^{th}$ CEST scan, which was performed directly

post-DTI showing evidence of recovery (about 10%) towards its pre-DTI value on the 5$^{th}$ scan (Figure 5.2). The CoV increased by about 39% for post-DTI scans compared to the first three pre-DTI scans, highlighting the effect of shim distortion on CEST reproducibility.

By contrast, CEST spectra and $MTR_{asym}$ curves for consecutive shim-corrected scans, were qualitatively similar, including for scans acquired post-DTI, with consistent $MTR_{asym}$ values. With shim correction, the mean (±sd) $MTR_{asym}$ integral CoV across 7 subjects was 2.67 ± 1.37 % compared to 83.70 ± 70.79% without shim correction. CoV of 2.69 % for CEST is comparable to GluCEST reproducibility studies conducted at 7 T in repeated measurements of five mice (Bagga et al., 2018) and *in vivo* in the human brain (Nanga et al., 2018).

Post processing using high-order polynomial fitting (Zhou, Jinyuan et al., 2003, Zhou, J. et al., 2008) helps to center the CEST spectra at the minimum to compensate for shifts of the entire Z-spectrum due to $B_0$ zero-order shim, however, a reduction in the $MTR_{asym}$ integral due to combined zero- and first-order magnetic field distortion cannot be recovered (Figure 5.3). The technique also cannot correct $B_0$ fluctuations that occur between different frequency offset measurements that cause asymmetric direct saturation effects in the Z-spectrum. In CEST acquisitions obtained after DTI, although a slight reduction in the CoV is observed for the $MTR_{asym}$ integral obtained after post-processing using a 12$^{th}$ order polynomial (173.15%) compared to the uncorrected case (208.67%), the intensity variation is still large. This shows that the CEST signal attenuation due to the cumulative effect of zero-order and first-order shim in the presence of fluctuating field cannot be corrected using simple post-processing techniques alone.

Even without the deliberate introduction of $B_0$ instability, the mean CoV for the first 3 scans of 1 to 7 subjects were lower for the shim-corrected session (CoV = 2.89$\pm$2 %) than for the session without shim correction (CoV = 13.99$\pm$7.48 %), showing improved measurement repeatability under conditions assumed to be constant. The $MTR_{asym}$ integral is also lower for scans acquired without shim correction compared to scans acquired with shim correction applied, suggesting that CEST measurements may be underestimated without proper correction. This reduction is due to the initial field homogeneity setting (i.e. pre-scan frequency and gradient offset) and due to the shim fluctuation, that may occur in between CEST offset measurements as a result of the eddy current sensitive EPI acquisition.

Zero-order shim (frequency offset shift) causes a shift in the entire CEST spectrum leading to a mismatch between the assumed and actual 0 ppm position (Wu, B. et al., 2016). Without proper shift correction, this causes an increase or decrease in the calculated $MTR_{asym}$ integral depending on the direction of the shift. The presence of field inhomogeneity along slice, phase encoding and readout directions (gradients) can cause a temporal shift, geometric distortion (shearing, stretching, compression, scaling) (Bammer et al., 2005, E. Mark Haacke et al., 1999), or phase dispersion across affected voxels (Reber et al., 1998, Wachowicz, Tadic & Fallone, 2012, Ward, Heidi A., Riederer & Jack, 2002) resulting in signal loss and positional mis-registration of the signal and the acquired offset images during voxel-wise CEST data analysis. As shown in Figure 5.4, during all acquisitions, a drift in both zero-order (frequency) shim and first-order (linear) shim was observed for scans acquired without shim correction. Directly after DTI the drift in zero order shim was as much as 10 Hz/min. However, this, as well as the shim offset observed at the beginning of the CEST measurement, was corrected when prospective shim correction was applied.

Considering the mean $MTR_{asym}$ in the first 3 pre-DTI scans only (Figure 5.6), the inter-session correlation (reproducibility between ShimCo and No ShimCo measurements) is reasonable ($r$ = 0.62), indicating that similar conclusions about relative glycogen concentrations in subjects could be drawn using the standard or shim-corrected CEST sequences. Although no gold standard glycogen measurement s available to us to confirm this, we expect the shim-corrected version to produce more accurate measurements by correcting for small subject motions and changes in field homogeneity. Subject 3 appears to be the cause of the modest correlation between sessions, since the $MTR_{asym}$ integral for that subject is unexpectedly low even in the shim corrected session. This is due to high initial offset frequency (zero-order shim) observed for the same subject resulting in CEST spectral shift from 0 ppm (Figure 5.2c). However, in addition to producing more repeatable and reproducible within-subject measurements, the navigated sequence also results in a lower between subject CoV (15.30 %) for $MTR_{asym}$ than the standard CEST sequence (38.71%).

Due to several instrumental and physiological factors, that influence the CEST effect, longitudinal and multicenter reproducibility is challenging in practice. The glycoCEST effect may be confounded by other CEST contrasts that appear in the Z-spectrum. Notably we observe reproducible dips at 2.5 ppm and -2 ppm, possibly corresponding to APT and NOE effects respectively that may affect glycogen MTRasym estimation. A handful of studies have examined

reproducibility of CEST measurements *in vivo* including Amine Proton Transfer Imaging (APTCEST) of the human breast at 7 T (Klomp et al., 2013), glutamate in mice using GluCEST (Bagga et al., 2018) and gray and white matter glutamate contrast in the human brain (Nanga et al., 2018). However, the effect of field inhomogeneity on repeatability and reproducibility of CEST data has not been evaluated. To our knowledge no study has evaluated the reproducibility of glycogen measurement using CEST MRI.

Our results demonstrate that drift in the scanner center frequency and gradients resulting from coil heating affects CEST spectra, misleading CEST interpretation and that this effect can be eliminated with application of prospective shim correction. This highlights the importance of correcting field inhomogeneity prospectively during longitudinal studies. The navigated CEST MRI sequence provides highly reproducible measurements in human calf muscle when shim correction is applied. Additional work needs to be established to investigate the reproducibility of CEST within and across specific regions of the calf muscle.

We acknowledge several other limitations of the current study, including a limited number of subjects. Effects of scanner field strength, RF coil type and environmental factors such as temperature were not assessed; however, we anticipate that this assessment of reproducibility lays the groundwork for further CEST reproducibility studies that will systematically investigate these important questions.

## 5.5. Conclusion

Scans acquired on the calf muscle of nine subjects, 5 times in each of two sessions in a total of 90 CEST scans, show that the motion and shim navigated CEST sequence produces more repeatable results compared to the standard unnavigated CEST sequence. The effect of $B_0$ field fluctuations on CEST reproducibility was also demonstrated. Our simultaneous real-time shim and motion navigated CEST sequence shows the potential to produce reproducible results by mitigating the effect of changes in field homogeneity. The navigated CEST sequence may prove particularly valuable for applications that require multiple scanning sessions, for example to study glycogen depletion and repletion in skeletal muscle.

# Chapter 6

# Summary and future work

CEST is an emerging MRI technique that has the ability to noninvasively measure endogenous biomarkers and exogenous agents relevant to various physiological, disease and medical conditions. CEST signal is proportional to the labile proton concentration and exchange rate and therefore provides measurable sensitivity enhancement for detecting CEST agents (Sun et al., 2011, Terreno, Castelli & Aime, 2010). The low concentration level of endogenous molecules (e.g. glycogen) makes the application of CEST MRI *in vivo* extremely susceptible to artefacts induced by environmental, experimental and physical factors. While some experimental parameters can be optimized to maximize the detection of the required CEST signal, subject motion and induced field inhomogeneity that may occur at any time during CEST acquisition are difficult to avoid. The problem is worse for endogenous molecules, such as hydroxyl groups that resonate very close to water, in which field inhomogeneity and motion escalate the effect direct water saturation by shifting the CEST-spectrum leading to misinterpretation of the CEST data.

In this thesis, the standard 2D gradient echo single shot EPI sequence was modified to include a continuous wave RF saturation pulse, RF irradiation parameters were optimized to maximize the glycoCEST signal, and finally the optimized CEST sequence was further modified to include double 3D-EPI volumetric navigators prior to the RF saturation pulse, for dynamic simultaneous motion and shim measurement and correction. The prospective motion and shim correction technique is independent of the CEST sequence. Its ability to detect changes in zero- and first-order shim was validated in phantom through manual adjustment of the system frequency (zero-order shim) and linear gradients (first-order shim). The technique was tested *in vivo* in the presence of subject pose changes. The scan-rescan reproducibility study was also examined in the presence of field inhomogeneity to validate the stability of the technique.

## 6.1. Selecting optimal RF irradiation parameters

Although CEST imaging allows indirect detection of species normally undetectable in standard MRI, the CEST effect is only a few percent. CEST signal is dependent on physiological as well as instrumental/experimental factors; the latter can be optimized for a specific metabolite of interest in order to maximize the CEST signal.

In Chapter 3, analytical solution of the Bloch-McConnell equations was used to find optimal irradiation parameters that maximize glycoCEST signal. The RF power and duration were systematically varied from weak to strong and short to long, respectively, in the three-pool exchange simulation model. The $MTR_{asym}$ and CEST spectra were shown to vary strongly with saturation power. An increase in saturation power resulted in widening of the CEST spectra while the $MTR_{asym}$ integral first increased to a maximum at an optimal power level of 1.5 μT and decreased with a further increase in saturation power (Figure 3.2 a&b). Although CEST signal also gradually increased with increasing RF irradiation duration (Figure 3.2 c&d), its effect was small compared to the effect of varying saturation power, especially at pulse durations longer than 2 seconds, where CEST signal became stable, reflecting the steady state proton exchange between solute and water pool.

Due to their small chemical shift from water, signal from hydroxyl groups is particularly dependent on saturation power. As shown by the simulation, weak power causes inefficient solute proton saturation leading to an attenuated CEST effect; on the other hand, very strong RF power directly attenuates the bulk water signal in addition to saturating solute protons, reducing sensitivity and specificity of CEST (Kim, Jinsuh et al., 2015, Sun & Sorensen, 2008, Sun et al., 2011). The variation in magnitude of CEST signal, spillover and MT effects on RF irradiation power shows that there is an optimal RF power that maximizes the CEST signal. The optimal power and duration for the RF irradiation (presaturation pulse ($B_1$)), is dependent on the rate constant, relaxation times, proton fraction, and chemical shift of the metabolite of interest. Despite limits on RF energy deposition, pulse width and duty cycle in standard continuous wave RF irradiation, it enables effective saturation, and an analytical solution for modeling the dynamics of the spin system can be obtained from the coupled Bloch-McConnell equations (Zaiss et al., 2015), which includes cross-relaxation terms to take MT into account.

The simulation result was validated in *in vivo* tests conducted at different saturation powers (see Figure 3.5 and Table 3.1), which also showed maximum glycoCEST signal at 1.5 μT. A saturation power of 1.5 μT and 1 second saturation pulse duration were subsequently selected as optimal parameters for glycoCEST, although a 700 ms pulse duration also produced meaningful results during validation of motion and shim correction in Chapter 4. In order to overcome hardware limitations on duty cycle and tissue SAR restrictions to obtain longer saturation pulse durations a

longer TR can be used, with the cost of extending scanning time. However, for clinical applications it is important to minimize both scan duration and energy deposition. Longer CW irradiation is sometimes not possible on clinical scanners, but the optimal saturation power and duration presented here may provide a good starting point for optimizing a pulsed irradiation scheme. Although optimization of pulsed RF irradiation is more complicated and requires optimization of additional parameters, including flip angle, and inter-pulse delay, it has been shown that a good CW design can inform optimal pulsed wave irradiation (Sun et al., 2011, Zhe Sun et al., 2008, Zu et al., 2011).

Using the optimized parameters, different glycogen phantom concentration levels could be distinguished (Figure 3.7 & Figure 3.8). The linear correlation (Pearson's $r = 0.98$, $p < 0.05$) between the $MTR_{asym}$ integral and phantom glycogen concentration demonstrates that detection of relative glycogen levels using CEST MRI is feasible with optimized RF irradiation parameters. Moreover, such optimization of parameters that affect the measured glycoCEST effect should improve reproducibility, opening the way to unbiased measurement of this biological information for clinical translation.

## 6.2. Effects of motion and shim on CEST and correction techniques

Subject motion and field inhomogeneity are the main sources of artifact in MR imaging. Due to its dependence on chemical shift and voxel-wise data analysis, CEST imaging is particularly sensitive to these effects. Motion results in a blurring of sharp contrast, geometric distortion, ghosting artifacts, signal loss or appearance of undesired strong signals in the image (Van de Walle, Lemahieu & Achten, 1997, Wood & Henkelman, 1985, Zaitsev, Maxim, Maclaren & Herbst, 2015). This causes false positive results ("dips" and "peaks" in the $MTR_{asym}$ and CEST spectrum) or induces field inhomogeneity artefacts (see Figure 4.3) misleading CEST data analysis and quantification. Field inhomogeneity affects the CEST spectrum and consequently also $MTR_{asym}$ data, which was observed to be very sensitive to slight changes in zero- and first-order shim (see Figure 4.5). Although, the pattern of artefactual increases and decrease in $MTR_{asym}$ as a function of shim variation is not deterministic, the results demonstrate that small variations in zero- and first-order shim may have a non-trivial effect on CEST quantification.

Techniques currently available for shim correction are based on retrospective post-processing of the data, either using a pre-acquired field map (Kim, Mina et al., 2009, Sun, Farrar & Sorensen,

2007) or fitting CEST spectra to a higher order polynomial (Zhou, Jinyuan et al., 2003, Zhou, J. et al., 2008). In the first method, a field map or map of the absolute water frequency is generated using a separate pulse sequence to center the shifted CEST spectrum according to the measured $B_0$ field variation. This method requires a separate pulse sequence and additional scanning time. Water saturation shift referencing (WASSR) (Dula et al., 2011, Kim, Mina et al., 2009) similarly uses a separate acquisition with low saturation power to detect the direct saturation of water and estimate the frequency shift caused by field inhomogeneities. However, this also requires additional scanning time and data post-processing. In the second method the CEST spectrum is fitted to a higher-order polynomial to find the minimum, which is assumed to be the center frequency (true water resonance frequency) and each voxel's CEST spectrum is shifted accordingly. This technique relies on sampling the minimum of the CEST spectrum in sufficient detail and the method is applicable only when the central peak in the CEST spectrum is sharp or if the CEST agents' exchangeable protons are sufficiently far from water for MT and DS effects to be negligible, so that the technique is robust to small errors in $B_0$ correction.

The effect of motion on CEST has not been thoroughly addressed in the literature. The few studies that examine motion correction in CEST MRI (Nirbhay N. Yadav, 2015, Schuenke et al., 2017) consider retrospective techniques. Retrospective motion correction methods based on volume-to-volume registration are well established for standard MRI (Atkinson et al., 1997, Cox, 1996, Friston et al., 1995, Jenkinson, M. et al., 2002, Stehling, Turner & Mansfield, 1991). However, these methods are not appropriate for CEST MRI, which involves multiple measurements with different saturation frequencies and therefore varying contrasts. Moreover, motion-induced field inhomogeneity that occurs in between offset measurements remains uncorrected using retrospective correction techniques.

## 6.3. Volumetric navigator-based motion and shim correction in CEST

The effectiveness and robustness of 3D-EPI navigators to correct for both motion and shim fluctuation in real-time has been demonstrated for other pulse sequences (Alhamud et al., 2016, Hess et al., 2011, Saleh et al., 2016). Here the CEST-DvNav sequence was shown also to accurately measure, report and correct a change in $B_0$ following manual adjustment of the scanner system frequency (zero-order shim) and linear gradients (first-order shim) (see Figure 4.6 and Figure 4.7)

The effect of adding the navigator to the CEST sequence was evaluated in Chapter 4. The main concern when interleaving two separate sequences is a possible contamination from one to the other. Since the relaxation period in CEST occupies a significant portion of the TR, the navigator could be inserted immediately before the saturation block to minimize the effect of CEST saturation on the navigator. Consequently, only minimal variation in the navigator signal was observed, limited to a slight trend that follows the CEST curve, due to the residual saturation effect from the preceding CEST (Figure 4.3). Conversely the $2^0$-flip angle RF excitation selected for the navigator was sufficiently low not to affect the CEST saturation, with a small difference (mean ± sd = 0.13 ± 0.89) between the CEST curves generated from acquisitions with and without the navigator.

*In vivo* scans acquired from the calf muscle of two volunteers demonstrate that the relatively stable zero and first-order shims were distorted directly after pose changes during acquisitions with motion but no correction. Without correction, the frequency increased for pose changes away from the origin and returned towards its initial value upon return to the initial pose (Figure 4.8). With motion and no correction applied (Mo-NoCo), false dips resembling metabolite detection occurred in addition to an artefactual shift in the CEST spectrum around the water resonance (Figure 4.9). Although pose changes were corrected when motion correction only was applied, the shim distortion remained, showing that correction for pose change alone cannot remove all the errors that occur as a result of motion. This is demonstrated in the Mo-MoCo case (Figure 4.9) where the subject's pose was corrected, but the resultant offset shift in the CEST-spectrum due to field inhomogeneity left uncorrected. During shim and motion correction, the DvNav adjusts the image FOV and shim parameters to correct for the changes immediately after they occur. Therefore, using the DvNav sequence, both pose changes and the resulting offset shift in the CEST-spectrum was corrected in the Mo-AllCo case. The results demonstrate clearly that zero- and first-order $B_0$ changes occur in the presence of subject pose change and that correcting only motion correction in CEST will be ineffective without employing $B_0$ correction. Hence, simultaneous motion and shim correction using our proposed method is desirable for accurate CEST data analysis and quantification. The motion used for testing was intended to mimic small voluntary leg movements that a subject might make to adjust to a comfortable position during scanning, rather than to account for physiological motion. However, the technique might also prove useful to correct small

bulk muscle motions that result from respiration or cardiac pulsation, as long as minimal motion occurs during navigator acquisition.

An advantage of the navigator method is that a field map can be computed dynamically, between different CEST offset measurements, unlike approaches such as WASSR that depend on field maps acquired before or after the acquisition. An alternative approach for achieving this dynamic correction is to determine $B_0$ maps from a dual echo CEST data (Auno, 2018, Wei et al., 2014, Zhou, Zhengwei, Bi & Li, 2017). Another recently proposed implementation of volumetric navigators to correct for motion in CEST at 7T (Auno, 2018) would not be effective for glycoCEST, since the navigator contrast in that work was affected by saturation which precluded acquiring motion-corrected Z-spectrum offsets close to water.

Prospective motion correction has been shown to reduce motion artifacts by adapting the data acquisition in real-time during in various MRI sequences (Alhamud et al., 2012, E. Mark Haacke et al., 1999, Hoinkiss & Porter, 2017, Lee, C. C. et al., 1998, Lee, Jongho et al., 2009, Tisdall et al., 2012). The PACE technique (Thesen et al., 2000) allows the use of motion parameters from rigid-body image registration to adapt slice positions and orientations in real-time. Prospective motion correction using navigators (Lin, W. et al., 2014, Tisdall et al., 2012, van der Kouwe, Benner & Dale, 2006, White et al., 2010) enables estimation of motion parameters in multishot imaging when it is not possible to estimate motion parameters reliably from the data acquired for individual shots. The advantage of navigator methods is that they can be modified so that magnetic field inhomogeneity can be estimated and corrected at the same time. Navigators are ideal for use in the CEST MRI pulse sequence, because of the long CEST relaxation period, the ability to simultaneously correct motion and shim changes, and the independence of the navigator from the main sequence.

## 6.4. Field inhomogeneity and CEST reproducibility

The effectiveness of CEST MRI in detecting metabolic changes in longitudinal studies, depends on the reproducibility, as well as the accuracy of CEST quantification. However, because the CEST method relies on indirect detection, it may be compromised by artifacts or contaminated by contributions from other metabolites that participate in proton chemical exchange. The dependence of CEST on physical and experimental factors makes it very sensitive to small variations in experimental variables.

In this study, the scan-rescan reproducibility of glycoCEST MRI was investigated under a dynamically changing field subsequent to a gradient-intensive diffusion scan that has previously been reported to introduce eddy current-induced magnetic field inhomogeneities (Alhamud et al., 2016, Avram et al., 2014, Bodammer et al., 2004, Truong, Chen & Song, 2008).

For shim uncorrected scans, inconsistent CEST results were observed across the session (see Figure 5.2, Figure 5.3, Table 5.1 and Table 5.2) with mean CoV of 83.07 ± 70.79 %. Before DTI the $MTR_{asym}$ integral generally decreased slightly as scans were repeated and CoV for different subjects ranged from 6 – 26 %. The measured shim parameters for post-DTI CEST scans showed that the zero-order shim (frequency) slightly increases along measurements without shim correction (Figure 5.4). After the DTI sequence, a dramatic reduction in $MTR_{asym}$ integral occurred in all subjects (Figure 5.5). However, using the navigated CEST sequence with motion and shim correction, frequency and linear gradient traces showed stable values, and consistent CEST results were obtained (CoV = 2.67 ± 1.37 %) for all scans, including those acquired post-DTI. This CoV, obtained at 3 T, is comparable to those of GagCEST in cartilage (1.9%) (Brinkhof et al., 2018), and GluCEST in mouse striatum (2.3%), and in the human brain (2%) (Nanga et al., 2018)at high field strengths (>=7 T). It is also lower than the CoV obtained for many metabolites (range 2% - 21%) (Zhang et al., 2018) using MRS at 3 T, although this region-dependent (de Matos et al., 2016). However, although DvNav CEST reduced between subject CoV compared to without the DvNav, the between subject CoV for DvNav glycoCEST (15%) is still higher than that obtained for GluCEST in human gray (2%), and white matter (6%) at 7 T (Nanga et al., 2018).

Fewer studies have investigated CEST reproducibility at clinical field strengths, however, even at 3 T repeatable measurements have been obtained for APT CEST in the breast (Dula et al., 2013)., and in the brain (Togao et al., 2015) and reasonable GagCEST reproducibility (ICC = 0.508/ 0.759) in different intervertebral disc regions (Deng et al., 2016a).

Interestingly, and more relevant to our intended application of CEST to skeletal muscle, one study at 3 T investigated reproducibility of creatine CEST in the soleus and lateral and medial gastrocnemius and found mean within-subject CoVs of 4.5%, 3.4% and 8.2% respectively (DeBrosse et al., 2016), slightly higher than what we obtain with the DvNav glycoCEST sequence.

For reproducible CEST results, experimental and physical parameters should be ideally kept constant during the course of multiple acquisitions. However, changes in field inhomogeneity between measurements are often unavoidable, resulting in inconsistency in the acquired data.

Field inhomogeneity may occur due to the slowly varying field fluctuations intrinsic to the MR hardware, heating of the iron coils, and mechanical vibrations, in combination with the susceptibility differences in different tissues and subject motion (Benner et al., 2006, Foerster, Tomasi & Caparelli, 2005, Pfeuffer et al., 2002, Ward, Heidi A., Riederer & Jack, 2002). The effect of field inhomogeneity is not only a position-dependent shift in the CEST spectrum that can be corrected using post-processing, but also irreversible attenuation of the CEST signal. Due to the hydroxyl group's close resonance frequency to that of water, glycoCEST MRI is particularly sensitive to B0 field inhomogeneity. Hence, prospective correction of field inhomogeneity is essential for reproducible glycoCEST measurement. Our results demonstrate that the navigated CEST MRI sequence provides reproducible measurements in human calf muscle when shim correction was applied.

## 6.5. Limitations and future work

One limitation of the DvNav motion and shim correction method is that motion that occurs during navigator acquisition and the short communication time gap cannot be corrected. However, this duration is very short compared to the rest of the sequence.

Secondly, as well as affecting zero- and first-order shims, subject motion can result in second order shim changes (Hess et al., 2011). Because the current Siemens hardware does not allow real-time control of higher-order shims, only zero-order and first-order shims are updated in the current work (although the navigator estimates the second-order shims). In addition, the motion estimates for the navigated CEST sequence rely on the Siemens implementation of PACE (Thesen et al., 2000), which terminates for translations in any direction greater than 20 mm and rotations greater than 8 degrees. However, the sequence will continue to run enabling offline estimation of motion parameters which can be used for retrospective correction.

The reproducibility of DvNav-CEST sequence was not evaluated on a known glycogen concentration because of the difficulty and expense of creating additional glycogen phantoms. Future studies could compare DvNav-CEST reproducibility and relative quantification to that of

the standard optimized sequence on known glycogen concentrations. We also did not investigate the effects of B1 transmit field correction which can be done via interpolation using pre-acquired flip angle maps (Windschuh et al., 2015). As head motion can also alter receiver sensitivity (Auno, 2018), this could be addressed in future work.

Finally, we would like to highlight that, the hydroxyl group CEST signal is small at lower magnetic fields (Zijl. et al., 2007), and different factors including uncorrected MT and DS effects, and saturated protons from other endogenous metabolites with overlapping resonance frequencies, such as glucose, may cause a reduction of the bulk water signal in addition to the metabolite of interest (glycogen). Although the RF irradiation parameters that maximize the glycoCEST signal can be optimized, signals detected *in vivo* should be considered glycogen-weighted, rather than pure glycogen. Jin et. al (Jin & Kim, 2014) suggest that Chemical Exchange sensitive spin-locking (CESL) provides better exchange rate selectivity and sensitivity than CEST. For molecules with fast exchange rate of glycogen and resonance frequency close to the water resonance, CESL could be as an alternative method for better sensitivity. It would be interesting in the future to implement DvNav in the CESL sequence for glycogen detection.

Moreover, absolute quantification of glycogen signal in particular; and the CEST signal in general, is not possible using the $MTR_{asym}$ method. The $MTR_{asym}$ integral is best applied to examine relative glycogen concentrations, for example to investigate glycogen level changes in well-controlled, repeated measured experiments. Advances in the reliability and practical application of CEST imaging, such as presented in this thesis, open the possibility of imaging a range of biologically important molecules that have not yet been studied in detail.

Moving to field strengths higher than 3 T will improve CEST SNR, and the longer water $T_1$ at higher fields will allow saturation transferred to water to be retained for longer. Because the chemical shift separation between metabolites is greater, CEST becomes more specific at higher field strength and glycogen detection sensitivity is increased as the exchange rate becomes slow relative to the chemical shift (Zijl. et al., 2018). It would be of interest to test the effectiveness and sensitivity of the DvNav-CEST technique at a higher field strength (e.g. 7 T), where both glycoCEST signal and field inhomogeneity is high.

# Chapter 7

# Conclusion

In this thesis, a CEST MRI pulse sequence was optimized to maximize the detection of glycogen by reducing competing factors. An optimal irradiation power of 1.5 μT and duration of 1 s were selected to maximize CEST signal for glycogen detection. These values were validated on *in vivo* on human calf muscle and different phantom glycogen concentrations were identified using the selected optimal RF irradiation parameters.

An optimized CEST sequence was presented that simultaneously performs real-time tracking and correction of pose changes, and frequency and first-order shim measurement and correction using double volumetric navigators (DvNavs). The 2D gradient echo single-shot EPI sequence was modified to acquire 3D EPI DvNavs prior to the continuous wave RF saturation pulse in each TR without any additional scanning time. Registration of successive first navigator magnitude images to the reference navigator magnitude image provides position and orientation estimation that are used to update the scanners coordinate system once in each TR of the CEST sequence. A field map is generated from the phase images of dual navigator contrasts of the same CEST TR and is used for zero-order (frequency) and first-order (linear gradient) shim correction.

In addition to introducing false ‘dips’ or ‘peaks’ that resemble the CEST effect, motion also induces field inhomogeneity that shifts the CEST spectrum. Phantom data showed that the navigator estimated and corrected the manual zero-order and first-order shim adjustments with minimal error. It was also shown that introducing the navigator does not corrupt the CEST data and the CEST has a minimal effect on the navigator contrast.

The scan-rescan reproducibility study demonstrated that shim changes lower the reproducibility of CEST data and validated the stability of DvNavs under a dynamically changing field induced by the preceding gradient-intensive diffusion scan. Without shim correction, the CEST sequence produced varying results for repeated scans, whereas consistent CEST data was acquired with shim correction. In conclusion, this work has demonstrated the effectiveness of motion and shim correction in CEST MRI and has presented and validated an optimized CEST sequence that is robust to motion and fluctuations in field inhomogeneity.

# References


A.K., K.B., Domenico, Z., Nico, P. & Jorge, J. 2016. Retrospective head motion correction approaches for diffusion tensor imaging: Effects of preprocessing choices on biases and reproducibility of scalar diffusion metrics. *Journal of Magnetic Resonance Imaging.* 43(1):99-106. DOI:doi:10.1002/jmri.24965.

Acheson, K.J., Schutz, Y., Bessard, T., Anantharaman, K., Flatt, J.P. & Jequier, E. 1988. Glycogen storage capacity and de novo lipogenesis during massive carbohydrate overfeeding in man. *Am J Clin Nutr.* 48(2):240-247.

Ackerman JL, O.M., Buxton RB, Brady TJ. . Ed. 1986. Rapid 3D tracking of small RF coils. . Montreal; : International Society of Magnetic Resonance in Medicine 1131–1132.

Alhamud, A., Taylor, P.A., van der Kouwe, A.J.W. & Meintjes, E.M. 2016. Real-Time Measurement and Correction of Both B0 Changes and Subject Motion in Diffusion Tensor Imaging Using a Double Volumetric Navigated (DvNav) Sequence. *NeuroImage.* 126:60-71. DOI:10.1016/j.neuroimage.2015.11.022.

Alhamud, A., Tisdall, M.D., Hess, A.T., Hasan, K.M., Meintjes, E.M. & van der Kouwe, A.J.W. 2012. Volumetric Navigators for Real Time Motion Correction in Diffusion Tensor Imaging. *Magnetic Resonance in Medicine.* 68(4):1097-1108. DOI:10.1002/mrm.23314.

Ali, S.H., Modic, M.E., Mahmoud, S.Y. & Jones, S.E. 2013. Reducing Clinical MRI Motion Degradation Using a Prescan Patient Information Pamphlet. *American Journal of Roentgenology.* 200(3):630-634. DOI:10.2214/AJR.12.9015.

Andrews-Shigaki, B.C., Armstrong, B.S., Zaitsev, M. & Ernst, T. 2011. Prospective motion correction for magnetic resonance spectroscopy using single camera Retro-Grate reflector optical tracking. *Journal of Magnetic Resonance Imaging.* 33(2):498-504. DOI:10.1002/jmri.22467.

Anemone, A., Consolino, L. & Longo, D.L. 2017. MRI-CEST assessment of tumour perfusion using X-ray iodinated agents: comparison with a conventional Gd-based agent. *Eur Radiol.* 27(5):2170-2179. DOI:10.1007/s00330-016-4552-7.

Atkinson, D., Hill, D.L., Stoyle, P.N., Summers, P.E. & Keevil, S.F. 1997. Automatic correction of motion artifacts in magnetic resonance images using an entropy focus criterion. *IEEE Trans Med Imaging.* 16(6):903-910. DOI:10.1109/42.650886.

Auno, S. 2018. Real-time motion and dynamic receiver sensitivity correction for CEST-MRI in the human brain at 7T.

Avram, A.V., Guidon, A., Truong, T.-K., Liu, C. & Song, A.W. 2014. Dynamic and Inherent B(0) Correction for DTI Using Stimulated Echo Spiral Imaging. *Magnetic resonance in medicine : official journal of the Society of Magnetic Resonance in Medicine / Society of Magnetic Resonance in Medicine.* 71(3):1044-1053. DOI:10.1002/mrm.24767.

Bagga, P., Pickup, S., Crescenzi, R., Martinez, D., Borthakur, A., D'Aquilla, K., Singh, A., Verma, G. et al. 2018. In vivo GluCEST MRI: Reproducibility, background contribution and source of glutamate changes in the MPTP model of Parkinson's disease. *Scientific reports.* 8(1):2883. DOI:10.1038/s41598-018-21035-3.

Baguet, E. & Roby, C. 1997. Off-Resonance Irradiation Effect in Steady-State NMR Saturation Transfer. *Journal of Magnetic Resonance.* 128(2):149-160. DOI:https://doi.org/10.1006/jmre.1997.1230.

Balteau, E., Hutton, C. & Weiskopf, N. 2010. Improved shimming for fMRI specifically optimizing the local BOLD sensitivity. *NeuroImage.* 49(1):327-336. DOI:https://doi.org/10.1016/j.neuroimage.2009.08.010.

Bammer, R., Skare, S., Newbould, R., Liu, C., Thijs, V., Ropele, S., Clayton, D.B., Krueger, G. et al. 2005. Foundations of Advanced Magnetic Resonance Imaging. *NeuroRx.* 2(2):167-196. Available: http://www.ncbi.nlm.nih.gov/pmc/articles/PMC1064985/.

Bartlett, J.W. & Frost, C. 2008. Reliability, repeatability and reproducibility: analysis of measurement errors in continuous variables. *Ultrasound Obstet Gynecol.* 31(4):466-475. DOI:10.1002/uog.5256.

Benner, T., van der Kouwe, A.J.W., Kirsch, J.E. & Sorensen, A.G. 2006. Real-time RF pulse adjustment for B0 drift correction. *Magnetic Resonance in Medicine.* 56(1):204-209. DOI:10.1002/mrm.20936.

Bergstrom, J. 1975. Percutaneous needle biopsy of skeletal muscle in physiological and clinical research. *Scand J Clin Lab Invest.* 35(7):609-616.

Bergstrom, J., Hermansen, L., Hultman, E. & Saltin, B. 1967. Diet, muscle glycogen and physical performance. *Acta Physiol Scand.* 71(2):140-150. DOI:10.1111/j.1748-1716.1967.tb03720.x.

Blamire AM, R.D., Nixon T. . 1996. Dynamic shim updating: a new approach towards optimized whole brain shimming. . *Magnetic Resonance in Medicine.* 36(1):159–165. .

Bloch, F. 1946. Nuclear Induction. *Physical Review.* 70(7-8):460-474. Available: https://link.aps.org/doi/10.1103/PhysRev.70.460.

Bodammer, N., Kaufmann, J., Kanowski, M. & Tempelmann, C. 2004. Eddy current correction in diffusion-weighted imaging using pairs of images acquired with opposite diffusion gradient polarity. *Magn Reson Med.* 51(1):188-193. DOI:10.1002/mrm.10690.

Bottomley, P.A., Hardy, C.J., Roemer, P.B. & Mueller, O.M. 1989. Proton-decoupled, Overhauser-enhanced, spatially localized carbon-13 spectroscopy in humans. *Magn Reson Med.* 12(3):348-363.

Brinkhof, S., Nizak, R., Khlebnikov, V., Prompers, J.J., Klomp, D.W.J. & Saris, D.B.F. 2018. Detection of early cartilage damage: feasibility and potential of gagCEST imaging at 7T. *Eur Radiol.* 28(7):2874-2881. DOI:10.1007/s00330-017-5277-y.

Cai, K., Haris, M., Singh, A., Kogan, F., Greenberg, J.H., Hariharan, H., Detre, J.A. & Reddy, R. 2012. Magnetic Resonance Imaging of Glutamate. *Nature medicine.* 18(2):302-306. DOI:10.1038/nm.2615.

Casadevall, A. & Fang, F.C. 2010. Reproducible Science. *Infection and Immunity.* 78(12):4972-4975. DOI:10.1128/IAI.00908-10.

Casey, A., Mann, R., Banister, K., Fox, J., Morris, P.G., Macdonald, I.A. & Greenhaff, P.L. 2000. Effect of carbohydrate ingestion on glycogen resynthesis in human liver and skeletal muscle, measured by 13C MRS. *American Journal of Physiology-Endocrinology and Metabolism.* 278(1):E65-E75. DOI:10.1152/ajpendo.2000.278.1.E65.

Chikop, S.A., Anchan, A.B.S., Koulagi, G., Honnedevasthana, A.A., Imam, S. & Geethanath, S. 2018. Automatic motion correction of Musculoskeletal MRI using DSLR camera. *Magnetic resonance imaging.* 48:74-79. DOI:https://doi.org/10.1016/j.mri.2017.12.031.

Clark, D.J., Smith, A.K., Dortch, R.D., Knopp, M.V. & Smith, S.A. 2016. Investigating hydroxyl chemical exchange using a variable saturation power chemical exchange saturation transfer (vCEST) method at 3 T. *Magnetic Resonance in Medicine.* 76(3):826-837. DOI:10.1002/mrm.25987.

Cline, G.W., Petersen, K.F., Krssak, M., Shen, J., Hundal, R.S., Trajanoski, Z., Inzucchi, S., Dresner, A. et al. 1999. Impaired glucose transport as a cause of decreased insulin-

stimulated muscle glycogen synthesis in type 2 diabetes. *N Engl J Med.* 341(4):240-246. DOI:10.1056/nejm199907223410404.

Cox, R.W. 1996. AFNI: software for analysis and visualization of functional magnetic resonance neuroimages. *Comput Biomed Res.* 29(3):162-173.

Crook, S.M., Davison, A.P. & Plesser, H.E. 2013. Learning from the Past: Approaches for Reproducibility in Computational Neuroscience. In *20 Years of Computational Neuroscience.* J.M. Bower, Ed. New York, NY: Springer New York. 73-102. DOI:10.1007/978-1-4614-1424-7_4.

Damadian & Raymond. 1971. Tumor Detection by Nuclear Magnetic Resonance. *Science.* 171(3976):1151-1153. DOI:10.1126/science.171.3976.1151.

de Graaf, R.A., Brown, P.B., McIntyre, S., Rothman, D.L. & Nixon, T.W. 2003. Dynamic shim updating (DSU) for multislice signal acquisition. *Magnetic Resonance in Medicine.* 49(3):409-416. DOI:doi:10.1002/mrm.10404.

de Matos, N.M.P., Meier, L., Wyss, M., Meier, D., Gutzeit, A., Ettlin, D.A. & Brügger, M. 2016. Reproducibility of Neurochemical Profile Quantification in Pregenual Cingulate, Anterior Midcingulate, and Bilateral Posterior Insular Subdivisions Measured at 3 Tesla. *Frontiers in Human Neuroscience.* 10(300). DOI:10.3389/fnhum.2016.00300.

DeBrosse, C., Nanga, R.P.R., Wilson, N., D'Aquilla, K., Elliott, M., Hariharan, H., Yan, F., Wade, K. et al. 2016. Muscle oxidative phosphorylation quantitation using creatine chemical exchange saturation transfer (CrCEST) MRI in mitochondrial disorders. *JCI Insight.* 1(18). DOI:10.1172/jci.insight.88207.

Deng, M., Yuan, J., Chen, W.T., Chan, Q., Griffith, J.F. & Wang, Y.X. 2016a. Evaluation of Glycosaminoglycan in the Lumbar Disc Using Chemical Exchange Saturation Transfer MR at 3.0 Tesla: Reproducibility and Correlation with Disc Degeneration. *Biomedical and Environmental Sciences.* 29(1):47-55. DOI:https://doi.org/10.3967/bes2016.005.

Deng, M., Chen, S.-Z., Yuan, J., Chan, Q., Zhou, J. & Wáng, Y.-X.J. 2016b. Chemical Exchange Saturation Transfer (CEST) MR Technique for Liver Imaging at 3.0 Tesla: an Evaluation of Different Offset Number and an After-Meal and Over-Night-Fast Comparison. *Molecular imaging and biology.* 18(2):274-282. DOI:10.1007/s11307-015-0887-8.

Desmond, K.L. & Stanisz, G.J. 2012. Understanding quantitative pulsed CEST in the presence of MT. *Magn Reson Med.* 67(4):979-990. DOI:10.1002/mrm.23074.

Dixon, W.T., Hancu, I., Ratnakar, S.J., Sherry, A.D., Lenkinski, R.E. & Alsop, D.C. 2010. A Multislice Gradient Echo Pulse Sequence for CEST Imaging. *Magnetic Resonance in Medicine.* 63(1):253-256. DOI:10.1002/mrm.22193.

Duerk, J.L. 1997. MRI: The basics. Ray H Hashemi and William G Bradley, Jr. Williams & Wilkins, Baltimore, 1997 $45.00 (softcover only), 443 illustrations, pp. 336. *Journal of Magnetic Resonance Imaging.* 7(3):614-615. DOI:doi:10.1002/jmri.1880070330.

Dula, A.N., Asche, E.M., Landman, B.A., Welch, E.B., Pawate, S., Sriram, S., Gore, J.C. & Smith, S.A. 2011. Development of chemical exchange saturation transfer at 7 T. *Magnetic Resonance in Medicine.* 66(3):831-838. DOI:10.1002/mrm.22862.

Dula, A.N., Arlinghaus, L.R., Dortch, R.D., Dewey, B.E., Whisenant, J.G., Ayers, G.D., Yankeelov, T.E. & Smith, S.A. 2013. Amide proton transfer imaging of the breast at 3 T: establishing reproducibility and possible feasibility assessing chemotherapy response. *Magn Reson Med.* 70(1):216-224. DOI:10.1002/mrm.24450.

Dumoulin, C.L., Souza, S.P. & Darrow, R.D. 1993. Real-time position monitoring of invasive devices using magnetic resonance. *Magnetic Resonance in Medicine.* 29(3):411-415. DOI:10.1002/mrm.1910290322.

E. Mark Haacke, Michael R. Thompson, Ramesh Venkatesan, Robert W. Brown & Cheng, Y.-C.N. 1999. *Magnetic resonance imaging: physical principles and sequence design.* . New York, NY: : Wiley-Liss, .

Ehman, R.L. & Felmlee, J.P. 1989. Adaptive technique for high-definition MR imaging of moving structures. *Radiology.* 173(1):255-263. DOI:10.1148/radiology.173.1.2781017.

English, P.T. & Moore, C. 1995. Image Artifacts. In *MRI for Radiographers.* P.T. English and C. Moore, Eds. London: Springer London. 51-70. DOI:10.1007/978-1-4471-3403-9_6.

Evans, W.J., Phinney, S.D. & Young, V.R. 1982. Suction applied to a muscle biopsy maximizes sample size. *Med Sci Sports Exerc.* 14(1):101-102.

Felmlee, J.P. & Ehman, R.L. 1987. Spatial presaturation: a method for suppressing flow artifacts and improving depiction of vascular anatomy in MR imaging. *Radiology.* 164(2):559-564. DOI:10.1148/radiology.164.2.3602402.

Foerster, B.U., Tomasi, D. & Caparelli, E.C. 2005. Magnetic Field Shift due to Mechanical Vibration in Functional Magnetic Resonance Imaging. *Magnetic Resonance in Medicine.* 54(5):1261-1267. DOI:10.1002/mrm.20695.

Foroosh, H., Zerubia, J.B. & Berthod, M. 2002. Extension of phase correlation to subpixel registration. *IEEE Transactions on Image Processing.* 11(3):188-200. DOI:10.1109/83.988953.

Frahm, J., Haase, A. & Matthaei, D. 1986. Rapid Three-Dimensional MR Imaging Using the FLASH Technique. *Journal of Computer Assisted Tomography.* 10(2):363-368. Available: https://journals.lww.com/jcat/Fulltext/1986/03000.

Friedman, J.I., McMahon, M.T., Stivers, J.T. & Van Zijl, P.C.M. 2010. Indirect Detection of Labile Solute Proton Spectra via the Water Signal Using Frequency-Labeled Exchange (FLEX) Transfer. *Journal of the American Chemical Society.* 132(6):1813-1815. DOI:10.1021/ja909001q.

Friston, K.J., Ashburner, J., Frith, C.D., Poline, J.-B., Heather, J.D. & Frackowiak, R.S.J. 1995. Spatial registration and normalization of images. *Hum Brain Mapp.* 3(3):165-189. DOI:doi:10.1002/hbm.460030303.

Fu, Z.W., Wang, Y., Grimm, R.C., Rossman, P.J., Felmlee, J.P., Riederer, S.J. & Ehman, R.L. 1995. Orbital navigator echoes for motion measurements in magnetic resonance imaging. *Magnetic Resonance in Medicine.* 34(5):746-753. DOI:10.1002/mrm.1910340514.

G., V., E., L.R. & E., V. 2012. Keyhole chemical exchange saturation transfer. *Magnetic Resonance in Medicine.* 68(4):1228-1233. DOI:doi:10.1002/mrm.23310.

Gizeaddis L. Simegn, A.J.W.v.d.K., Phllip Zhe Sun, Borjan Gagoski, Frances Robertson, M. Dylan Tisdall, Andrew Bosch, Ernesta Meintjes, and A. Alhamud. 2017. 3D Volume Navigator based Prospective Motion Correction in CEST MRI. *ISMRM Workshop on Motion Correction in MRI & MRS*. Cape Town, South Africa, 08-11 september 2017 2017. Available: https://www.ismrm.org/workshops/MoCor17/program.htm.

Godfrey, R. & Quinlivan, R. 2016. Skeletal muscle disorders of glycogenolysis and glycolysis. *Nature Reviews Neurology.* 12:393. DOI:10.1038/nrneurol.2016.75.

Gold, G.E., Han, E., Stainsby, J., Wright, G., Brittain, J. & Beaulieu, C. 2004. Musculoskeletal MRI at 3.0 T: Relaxation Times and Image Contrast. *American Journal of Roentgenology.* 183(2):343-351. DOI:10.2214/ajr.183.2.1830343.

Graaf, R.A.d. 01 November 2007. Basic Principles. In *In Vivo NMR Spectroscopy.* 2nd edition ed.: John Wiley & Sons,. DOI:doi:10.1002/9780470512968.ch1.

Gruetter, R. 1993. Automatic, localized in Vivo adjustment of all first-and second-order shim coils. *Magnetic Resonance in Medicine.* 29(6):804-811. DOI:doi:10.1002/mrm.1910290613.

H., E., B., S., JC., S., J., R. & ME., A. Eds. 1999. Real Time Head Motion Correction for Functional MRI. . Philadelphia, PA, USA. : ISMRM. 262.

Hahn, E.L. 1950. Spin Echoes. *Physical Review.* 80(4):580-594. Available: https://link.aps.org/doi/10.1103/PhysRev.80.580.

Hansen, B.F., Asp, S., Kiens, B. & Richter, E.A. 1999. Glycogen concentration in human skeletal muscle: effect of prolonged insulin and glucose infusion. *Scand J Med Sci Sports.* 9(4):209-213.

Haris, M., Cai, K., Singh, A., Hariharan, H. & Reddy, R. 2011. In vivo mapping of brain myo-inositol. *NeuroImage.* 54(3):2079-2085. DOI:10.1016/j.neuroimage.2010.10.017.

Haris, M., Singh, A., Cai, K., Nath, K., Crescenzi, R., Kogan, F., Hariharan, H. & Reddy, R. 2013. MICEST: a potential tool for non-invasive detection of molecular changes in Alzheimer's disease. *J Neurosci Methods.* 212(1):87-93. DOI:10.1016/j.jneumeth.2012.09.025.

Harris, R.K., Becker, E.D., Cabral de Menezes, S.M., Goodfellow, R. & Granger, P. 2002. NMR Nomenclature: Nuclear Spin Properties and Conventions for Chemical Shifts. IUPAC Recommendations 2001. *Solid State Nucl Magn Reson.* 22(4):458-483. DOI:10.1006/snmr.2002.0063.

He Zhu, C.K.J., Peter C. M. van Zijl, Peter B. Barker. 2010. Fast 3D Chemical Exchange Saturation Transfer Imaging of the human brain. *Magnetic Resonance in Medicine.* 64:638-644.

Henkelman, R.M., Huang, X., Xiang, Q.-S., Stanisz, G.J., Swanson, S.D. & Bronskill, M.J. 1993. Quantitative interpretation of magnetization transfer. *Magnetic Resonance in Medicine.* 29(6):759-766. DOI:10.1002/mrm.1910290607.

Hennig, J. 1999. K-space sampling strategies. *Eur Radiol.* 9(6):1020-1031. DOI:10.1007/s003300050788.

Herbst M, M.J., Korvink JG, Zaitsev M. A Ed. 2011. practical tracking system to avoid motion artifacts. . Montreal, Canada, 7-13. Magnetic resonance in medicine 2683.

Hermansen, L., Hultman, E. & Saltin, B. 1967. Muscle glycogen during prolonged severe exercise. *Acta Physiol Scand.* 71(2):129-139. DOI:10.1111/j.1748-1716.1967.tb03719.x.

Herrero, P., Kisrieva-Ware, Z., Dence, C.S., Patterson, B., Coggan, A.R., Han, D.H., Ishii, Y., Eisenbeis, P. et al. 2007. PET measurements of myocardial glucose metabolism with 1-11C-glucose and kinetic modeling. *J Nucl Med.* 48(6):955-964. DOI:10.2967/jnumed.106.037598.

Hess Aaron T., A.O.C., Dylan Tisdall M., Gregory Sorensen A., Kouwe André J. W., Meintjes Ernesta M. 2012. Real-time motion and B0 correction for localized adiabatic selective refocusing (LASER) MRSI using echo planar imaging volumetric navigators. *NMR in biomedicine.* 25(2):347-358. DOI:doi:10.1002/nbm.1756.

Hess, A.T., Tisdall, M.D., Andronesi, O.C., Meintjes, E.M. & van der Kouwe, A.J.W. 2011. Real-time Motion and B0 corrected single voxel spectroscopy using volumetric navigators. *Magnetic Resonance in Medicine.* 66(2):314-323. DOI:10.1002/mrm.22805.

Hoinkiss, D.C. & Porter, D.A. 2017. Prospective motion correction in 2D multishot MRI using EPI navigators and multislice-to-volume image registration. *Magnetic Resonance in Medicine.* 78(6):2127-2135. DOI:doi:10.1002/mrm.26951.

Holdsworth, S.J., Aksoy, M., Newbould, R.D., Yeom, K., Van, A.T., Ooi, M.B., Barnes, P.D., Bammer, R. et al. 2012. Diffusion tensor imaging (DTI) with retrospective motion correction for large-scale pediatric imaging. *J Magn Reson Imaging.* 36(4):961-971. DOI:10.1002/jmri.23710.

Hong, C., Lee, D.H. & Han, B.S. 2014. Characteristics of geometric distortion correction with increasing field-of-view in open-configuration MRI. *Magn Reson Imaging.* 32(6):786-790. DOI:10.1016/j.mri.2014.02.007.

Hounsfield, G.N. 1973. Computerized transverse axial scanning (tomography). 1. Description of system. *Br J Radiol.* 46(552):1016-1022. DOI:10.1259/0007-1285-46-552-1016.

Huang, S.-M., Jan, M.-L., Liang, H.-C., Chang, C.-H., Wu, Y.-C., Tsai, S.-Y. & Wang, F.-N. 2015. Investigation of Readout RF Pulse Impact on the Chemical Exchange Saturation Transfer Spectrum. *Scientific reports.* 5:15062. DOI:10.1038/srep15062.

Ivy, J.L. 2004. Regulation of Muscle Glycogen Repletion, Muscle Protein Synthesis and Repair Following Exercise. *Journal of Sports Science & Medicine.* 3(3):131-138. Available: http://www.ncbi.nlm.nih.gov/pmc/articles/PMC3905295/.

Iwase, T., Okai, C., Kamata, Y., Tajima, A. & Mizunoe, Y. 2018. A straightforward assay for measuring glycogen levels and RpoS. *Journal of Microbiological Methods.* 145:93-97. DOI:https://doi.org/10.1016/j.mimet.2017.12.008.

J., H., CK., J., J., B., SA., S., PCM., v.Z. & J., Z. 2007. Quantitative Description of the Asymmetry in Magnetization Transfer Effects around the Water Resonance in the Human Brain. *Magnetic Resonance in Medicine.* 58(4):786-793. DOI:10.1002/mrm.21387.

Jenkinson, M. 2003. Fast, automated, N-dimensional phase-unwrapping algorithm. *Magnetic Resonance in Medicine.* 49(1):193-197. DOI:10.1002/mrm.10354.

Jenkinson, M., Bannister, P., Brady, M. & Smith, S. 2002. Improved optimization for the robust and accurate linear registration and motion correction of brain images. *NeuroImage.* 17(2):825-841.

Jensen, J., Rustad, P.I., Kolnes, A.J. & Lai, Y.-C. 2011. The Role of Skeletal Muscle Glycogen Breakdown for Regulation of Insulin Sensitivity by Exercise. *Frontiers in Physiology.* 2:112. DOI:10.3389/fphys.2011.00112.

Jezzard, P. & Clare, S. 1999. Sources of distortion in functional MRI data. *Hum Brain Mapp.* 8(2-3):80-85.

Jiang, W., Zhou, I.Y., Wen, L., Zhou, X. & Sun, P.Z. 2016. A theoretical analysis of chemical exchange saturation transfer echo planar imaging (CEST-EPI) steady state solution and the CEST sensitivity efficiency-based optimization approach. *Contrast media & molecular imaging.* 11(5):415-423. DOI:10.1002/cmmi.1699.

Jin, T. & Kim, S.G. 2014. Advantages of chemical exchange-sensitive spin-lock (CESL) over chemical exchange saturation transfer (CEST) for hydroxyl– and amine–water proton exchange studies. *NMR in biomedicine.* 27(11):1313-1324. DOI:doi:10.1002/nbm.3191.

Jin, T., Mehrens, H., Hendrich, K.S. & Kim, S.-G. 2014. Mapping Brain Glucose Uptake with Chemical Exchange-Sensitive Spin-Lock Magnetic Resonance Imaging. *Journal of Cerebral Blood Flow & Metabolism.* 34(8):1402-1410. DOI:10.1038/jcbfm.2014.97.

Katz, A., Broberg, S., Sahlin, K. & Wahren, J. 1986. Leg glucose uptake during maximal dynamic exercise in humans. *Am J Physiol.* 251(1 Pt 1):E65-70. DOI:10.1152/ajpendo.1986.251.1.E65.

Keating, B. & Ernst, T. 2012. Real-time Dynamic Frequency and Shim Correction for Single-voxel MR Spectroscopy. *Magnetic Resonance in Medicine.* 68(5):1339-1345. DOI:10.1002/mrm.24129.

Khlebnikov, V., Windschuh, J., Siero, J.C.W., Zaiss, M., Luijten, P.R., Klomp, D.W.J. & Hoogduin, H. 2017. On the transmit field inhomogeneity correction of relaxation-compensated amide and NOE CEST effects at 7 T. *NMR in biomedicine.* 30(5):e3687. DOI:10.1002/nbm.3687.

Kim, J., Wu, Y., Guo, Y., Zheng, H. & Sun, P.Z. 2015. A review of optimization and quantification techniques for chemical exchange saturation transfer (CEST) MRI toward sensitive in vivo imaging. *Contrast media & molecular imaging.* 10(3):163-178. DOI:10.1002/cmmi.1628.

Kim, M., Gillen, J., Landman, B.A., Zhou, J. & van Zijl, P.C.M. 2009. WAter Saturation Shift Referencing (WASSR) for chemical exchange saturation transfer experiments. *Magnetic Resonance in Medicine.* 61(6):1441-1450. DOI:10.1002/mrm.21873.

Klomp, D.W., Dula, A.N., Arlinghaus, L.R., Italiaander, M., Dortch, R.D., Zu, Z., Williams, J.M., Gochberg, D.F. et al. 2013. Amide proton transfer imaging of the human breast at 7T: development and reproducibility. *NMR Biomed.* 26(10):1271-1277. DOI:10.1002/nbm.2947.

Kober, T., Gruetter, R. & Krueger, G. 2012. Prospective and retrospective motion correction in diffusion magnetic resonance imaging of the human brain. *NeuroImage.* 59(1):389-398. DOI:10.1016/j.neuroimage.2011.07.004.

Kogan, F., Hariharan, H. & Reddy, R. 2013. Chemical Exchange Saturation Transfer (CEST) Imaging: Description of Technique and Potential Clinical Applications. *Current Radiology Reports.* 1(2):102-114. DOI:10.1007/s40134-013-0010-3.

Kreitzman, S.N., Coxon, A.Y. & Szaz, K.F. 1992. Glycogen storage: illusions of easy weight loss, excessive weight regain, and distortions in estimates of body composition. *Am J Clin Nutr.* 56(1 Suppl):292s-293s.

Lange, T., Maclaren, J., Buechert, M. & Zaitsev, M. 2012. Spectroscopic Imaging with Prospective Motion Correction and Retrospective Phase Correction. *Magnetic Resonance in Medicine.* 67(6):1506-1514. DOI:10.1002/mrm.23136.

Lauterbur, P.C. 1973. Image Formation by Induced Local Interactions: Examples Employing Nuclear Magnetic Resonance. *Nature.* 242(5394):190-191. DOI:10.1038/242190a0.

Lee, C.C., Grimm, R.C., Manduca, A., Felmlee, J.P., Ehman, R.L., Riederer, S.J. & Jack, C.R., Jr. 1998. A prospective approach to correct for inter-image head rotation in fMRI. *Magn Reson Med.* 39(2):234-243.

Lee, J., Lustig, M., Kim, D.-h. & Pauly, J.M. 2009. Improved shim method based on the minimization of the maximum off-resonance frequency for balanced SSFP. *Magnetic Resonance in Medicine.* 61(6):1500-1506. DOI:10.1002/mrm.21800.

Lei, H., Morgenthaler, F., Yue, T. & Gruetter, R. 2007. Direct validation of in vivo localized 13C MRS measurements of brain glycogen. *Magnetic Resonance in Medicine.* 57(2):243-248. DOI:doi:10.1002/mrm.21128.

Li, A.X., Hudson, R.H.E., Barrett, J.W., Jones, C.K., Pasternak, S.H. & Bartha, R. 2008. Four-pool modeling of proton exchange processes in biological systems in the presence of MRI–paramagnetic chemical exchange saturation transfer (PARACEST) agents. *Magnetic Resonance in Medicine.* 60(5):1197-1206. DOI:doi:10.1002/mrm.21752.

Li, B., She, H., Zhang, S., Keupp, J., Dimitrov, I., Montillo, A., Madhuranthakam, A., Lenkinski, R. et al. Eds. 2017. Image registration with structuralized Mutual Information: application to CEST. *in proc. 25th ISMRM Annual meeting and exihibition*. Honolulu, USA: ISMRM.

Liepinsh, E. & Otting, G. 1996. Proton exchange rates from amino acid side chains— implications for image contrast. *Magnetic Resonance in Medicine.* 35(1):30-42. DOI:10.1002/mrm.1910350106.

Lin, C.Y., Yadav, N.N., Ratnakar, J., Sherry, A.D. & van Zijl, P.C. 2014. In vivo imaging of paraCEST agents using frequency labeled exchange transfer MRI. *Magn Reson Med.* 71(1):286-293. DOI:10.1002/mrm.24603.

Lin, C.Y., Yadav, N.N., Friedman, J.I., Ratnakar, J., Sherry, A.D. & Zijl, P.C.M.v. 2012. Using frequency-labeled exchange transfer to separate out conventional magnetization transfer effects from exchange transfer effects when detecting ParaCEST agents. *Magnetic Resonance in Medicine.* 67(4):906-911. DOI:doi:10.1002/mrm.24161.

Lin, W., Nielsen, T., Qin, Q., Mostofsky, S.H., Wei, J., Huang, F. & Duensing, G.R. 2014. Real-time motion correction in two-dimensional multislice imaging with through-plane navigator. *Magn Reson Med.* 71(6):1995-2005. DOI:10.1002/mrm.24852.

Ling, W., Regatte, R.R., Navon, G. & Jerschow, A. 2008. Assessment of glycosaminoglycan concentration in vivo by chemical exchange-dependent saturation transfer (gagCEST).

*Proceedings of the National Academy of Sciences.* 105(7):2266. Available: http://www.pnas.org/content/105/7/2266.abstract.

Liu, G., Gilad, A.A., Bulte, J.W.M., van Zijl, P.C.M. & McMahon, M.T. 2010. High-throughput screening of chemical exchange saturation transfer MR contrast agents. *Contrast media & molecular imaging.* 5(3):162-170. DOI:10.1002/cmmi.383.

Liu, G., Ali, M.M., Yoo, B., Griswold, M.A., Tkach, J.A. & Pagel, M.D. 2009. PARACEST MRI with improved temporal resolution. *Magnetic Resonance in Medicine.* 61(2):399-408. DOI:10.1002/mrm.21863.

Liu G, S.X., KWY., C. & MT., M. 2013. Nuts and Bolts of CEST MR imaging. *NMR in biomedicine.* 26(7):810-828. DOI:10.1002/nbm.2899.

Liu., G. 2008. Development of PARACEST MRI to detect cancer biomarkers. . Dissertation Case Western Reserve Univ. .

Luh, W.M., Wong, E.C., Bandettini, P.A. & Hyde, J.S. 1999. QUIPSS II with thin-slice TI1 periodic saturation: a method for improving accuracy of quantitative perfusion imaging using pulsed arterial spin labeling. *Magn Reson Med.* 41(6):1246-1254.

Maclaren, J., Herbst, M., Speck, O. & Zaitsev, M. 2013. Prospective motion correction in brain imaging: a review. *Magn Reson Med.* 69(3):621-636. DOI:10.1002/mrm.24314.

Maclaren, J., Aksoy, M., Ooi, M.B., Zahneisen, B. & Bammer, R. 2018. Prospective motion correction using coil-mounted cameras: Cross-calibration considerations. *Magn Reson Med.* 79(4):1911-1921. DOI:10.1002/mrm.26838.

Magnusson, I., Rothman, D.L., Katz, L.D., Shulman, R.G. & Shulman, G.I. 1992. Increased rate of gluconeogenesis in type II diabetes mellitus. A 13C nuclear magnetic resonance study. *J Clin Invest.* 90(4):1323-1327. DOI:10.1172/jci115997.

Mansfield, P. 1977. Multi-planar image formation using NMR spin-echos. *J. Phys. C: Solid State Physics*

10:55-58.

McConnell, H.M. 1958. Reaction Rates by Nuclear Magnetic Resonance. *The Journal of Chemical Physics.* 28(3):430-431. DOI:10.1063/1.1744152.

Michael T. McMahon, A.A.G., Jeff W. M. Bulte, and Peter C.M. van Zijl 2017. *Chemical Exchange Saturation Transfer imaging: Advances and applications* Pan Stanford Publishing Pte. Ltd., Singapore.

Muller-Lutz, A., Schleich, C., Schmitt, B., Topgoz, M., Pentang, G., Antoch, G., Wittsack, H.J. & Miese, F. 2015. Improvement of gagCEST imaging in the human lumbar intervertebral disc by motion correction. *Skeletal Radiol.* 44(4):505-511. DOI:10.1007/s00256-014-2034-z.

Murase, K. & Tanki, N. 2011. Numerical solutions to the time-dependent Bloch equations revisited. *Magnetic resonance imaging.* 29(1):126-131. DOI:https://doi.org/10.1016/j.mri.2010.07.003.

Nanga, R.P.R., DeBrosse, C., Kumar, D., Roalf, D., McGeehan, B., D'Aquilla, K., Borthakur, A., Hariharan, H. et al. 2018. Reproducibility of 2D GluCEST in healthy human volunteers at 7 T. *Magnetic Resonance in Medicine.* 80(5):2033-2039. DOI:doi:10.1002/mrm.27362.

Nasrallah, F.A., Pages, G., Kuchel, P.W., Golay, X. & Chuang, K.H. 2013. Imaging brain deoxyglucose uptake and metabolism by glucoCEST MRI. *J Cereb Blood Flow Metab.* 33(8):1270-1278. DOI:10.1038/jcbfm.2013.79.

Nieman, D.C., Shanely, R.A., Zwetsloot, K.A., Meaney, M.P. & Farris, G.E. 2015. Ultrasonic assessment of exercise-induced change in skeletal muscle glycogen content. *BMC Sports Sci Med Rehabil.* 7:9. DOI:10.1186/s13102-015-0003-z.

Nirbhay N. Yadav, K.W.Y.C., Monica Pearl, Piotr Walczak, Miroslaw Janowski, Peter C. M. van Zijl, and Michael T. McMahon, . Ed. 2015. Retrospective motion correction in CEST MRI data using time domain analysis,. Ontario, Canada, 30 May- 05 June. International society of magnetic resonance in medicine 1752.

Oz, G., Henry, P.G., Seaquist, E.R. & Gruetter, R. 2003. Direct, noninvasive measurement of brain glycogen metabolism in humans. *Neurochem Int.* 43(4-5):323-329.

Paschal, C.B. & Morris, H.D. 2004. K-space in the clinic. *J Magn Reson Imaging.* 19(2):145-159. DOI:10.1002/jmri.10451.

Pekar, J., Jezzard, P., Roberts, D.A., Leigh, J.S., Jr., Frank, J.A. & McLaughlin, A.C. 1996. Perfusion imaging with compensation for asymmetric magnetization transfer effects. *Magn Reson Med.* 35(1):70-79.

Pfeuffer, J., Van de Moortele, P.-F., Ugurbil, K., Hu, X. & Glover, G.H. 2002. Correction of physiologically induced global off-resonance effects in dynamic echo-planar and spiral functional imaging. *Magnetic Resonance in Medicine.* 47(2):344-353. DOI:10.1002/mrm.10065.

Poole, M. & Bowtell, R. 2008. Volume parcellation for improved dynamic shimming. *Magnetic Resonance Materials in Physics, Biology and Medicine.* 21(1):31. DOI:10.1007/s10334-007-0102-2.

Proctor, W.G. & Yu, F.C. 1950. The Dependence of a Nuclear Magnetic Resonance Frequency upon Chemical Compound. *Physical Review.* 77(5):717-717. Available: https://link.aps.org/doi/10.1103/PhysRev.77.717.

Reber, P.J., Wong, E.C., Buxton, R.B. & Frank, L.R. 1998. Correction of off resonance-related distortion in echo-planar imaging using EPI-based field maps. *Magn Reson Med.* 39(2):328-330.

Reese, T.G., Davis, T.L. & Weisskoff, R.M. 1995. Automated shimming at 1.5 t using echo-planar image frequency maps. *Journal of Magnetic Resonance Imaging.* 5(6):739-745. DOI:doi:10.1002/jmri.1880050621.

Reichenbach, J.R., Venkatesan, R., Yablonskiy, D.A., Thompson, M.R., Lai, S. & Haacke, E.M. 1997. Theory and application of static field inhomogeneity effects in gradient-echo imaging. *Journal of Magnetic Resonance Imaging.* 7(2):266-279. DOI:doi:10.1002/jmri.1880070203.

Ren, J., Trokowski, R., Zhang, S., Malloy, C.R. & Sherry, A.D. 2008. Imaging the tissue distribution of glucose in livers using a PARACEST sensor. *Magn Reson Med.* 60(5):1047-1055. DOI:10.1002/mrm.21722.

Riek, J.K., Totterman, S.M., Tekalp, A.M., Smith, W.E. & Kwok, E. 1993. Flow compensation in MRI using a phase-corrected real reconstruction. *Magnetic Resonance in Medicine.* 30(6):724-731. DOI:doi:10.1002/mrm.1910300610.

Roach, P.J., Depaoli-Roach, A.A., Hurley, T.D. & Tagliabracci, V.S. 2012. Glycogen and its metabolism: some new developments and old themes. *Biochem J.* 441(3):763-787. DOI:10.1042/bj20111416.

Rzedzian, R., Chapman, B., Mansfield, P., Coupland, R.E., Doyle, M., Chrispin, A., Guilfoyle, D. & Small, P. 1983. Real-time nuclear magnetic resonance clinical imaging in paediatrics. *Lancet.* 2(8362):1281-1282.

S., M.P., W., B.R., J.O., M.D. & S., W.B. 2004. Correction of spatial distortion in EPI due to inhomogeneous static magnetic fields using the reversed gradient method. *Journal of Magnetic Resonance Imaging.* 19(4):499-507. DOI:doi:10.1002/jmri.20032.

Sagiyama K, Zhang S & Dimitrov I, e.a. Eds. 2014. In Vivo Monitoring of Liver Glycogen by Chemical Exchange Saturation Transfer Imaging (GlycoCEST) in Live Mice. ISMRM.

Saitoh, S., Tasaki, Y., Tagami, K. & Suzuki, M. 1994. Muscle glycogen repletion and pre-exercise glycogen content: effect of carbohydrate loading in rats previously fed a high fat diet. *Eur J Appl Physiol Occup Physiol.* 68(6):483-488.

Saleh, M.G., Alhamud, A., Near, J., van der Kouwe, A.J. & Meintjes, E.M. 2016. Volumetric navigated MEGA-SPECIAL for real-time motion and shim corrected GABA editing. *NMR Biomedicine* 29(3):248-255. DOI:10.1002/nbm.3454.

Scheidegger, R., Vinogradov, E. & Alsop, D.C. 2011. Amide proton transfer imaging with improved robustness to magnetic field inhomogeneity and magnetization transfer asymmetry using saturation with frequency alternating RF irradiation. *Magn Reson Med.* 66(5):1275-1285. DOI:10.1002/mrm.22912.

Schmitt, B., Zaiß, M., Zhou, J. & Bachert, P. 2011. Optimization of pulse train presaturation for CEST imaging in clinical scanners. *Magnetic Resonance in Medicine.* 65(6):1620-1629. DOI:doi:10.1002/mrm.22750.

Schneider, E., Prost, R.W. & Glover, G.H. 1993. Pulsed magnetization transfer versus continuous wave irradiation for tissue contrast enhancement. *Journal of Magnetic Resonance Imaging.* 3(2):417-423. DOI:doi:10.1002/jmri.1880030218.

Schuenke, P., Paech, D., Koehler, C., Windschuh, J., Bachert, P., Ladd, M.E., Schlemmer, H.-P., Radbruch, A. et al. 2017. Fast and Quantitative T1ρ-weighted Dynamic Glucose Enhanced MRI. *Scientific reports.* 7:42093. Available: http://europepmc.org/abstract/MED/28169369 [2017/02//].

Shah, T., Lu, L., Dell, K.M., Pagel, M.D., Griswold, M.A. & Flask, C.A. 2011. CEST-FISP: A Novel Technique for Rapid Chemical Exchange Saturation Transfer (CEST) MRI at 7T. *Magnetic Resonance in Medicine.* 65(2):432-437. DOI:10.1002/mrm.22637.

Shanely, R.A., Zwetsloot, K.A., Triplett, N.T., Meaney, M.P., Farris, G.E. & Nieman, D.C. 2014. Human skeletal muscle biopsy procedures using the modified Bergstrom technique. *J Vis Exp.* 10.3791/51812(91):51812. DOI:10.3791/51812.

Sikdar, S., Wei, Q. & Cortes, N. 2014. Dynamic ultrasound imaging applications to quantify musculoskeletal function. *Exerc Sport Sci Rev.* 42(3):126-135. DOI:10.1249/jes.0000000000000015.

Simegn, G.L., Van der Kouwe, A.J.W., Robertson, F.C., Meintjes, E.M. & Alhamud, A. 2018. Real-time simultaneous shim and motion measurement and correction in glycoCEST MRI using double volumetric navigators (DvNavs). *Magnetic Resonance in Medicine.* 0(0):1-14. DOI:doi:10.1002/mrm.27597.

Stanisz, G.J., Odrobina, E.E., Pun, J., Escaravage, M., Graham, S.J., Bronskill, M.J. & Henkelman, R.M. 2005. T1, T2 relaxation and magnetization transfer in tissue at 3T. *Magnetic Resonance in Medicine.* 54(3):507-512. DOI:10.1002/mrm.20605.

Stehling, M.K., Turner, R. & Mansfield, P. 1991. Echo-planar imaging: magnetic resonance imaging in a fraction of a second. *Science.* 254(5028):43-50.

Sukumar, S. 1999. Echo planar imaging on high field microimaging systems. *Current Science.* 76(6):808-812. Available: http://www.jstor.org/stable/24101067.

Sun, P.Z. 2010a. Simultaneous determination of labile proton concentration and exchange rate utilizing optimal RF power: radio frequency power (RFP) dependence of chemical exchange saturation transfer (CEST) MRI. *Journal of Magnetic Resonance.* 202(2):155. DOI:10.1016/j.jmr.2009.10.012.

Sun, P.Z. 2010b. Simplified and scalable numerical solution for describing multi-pool chemical exchange saturation transfer (CEST) MRI contrast. *Journal of Magnetic Resonance.* 205(2):235-241. DOI:https://doi.org/10.1016/j.jmr.2010.05.004.

Sun, P.Z. & Sorensen, A.G. 2008. Imaging pH using the chemical exchange saturation transfer (CEST) MRI: Correction of concomitant RF irradiation effects to quantify CEST MRI for chemical exchange rate and pH. *Magn Reson Med.* 60(2):390-397. DOI:10.1002/mrm.21653.

Sun, P.Z., van Zijl, P.C.M. & Zhou, J. 2005. Optimization of the irradiation power in chemical exchange dependent saturation transfer experiments. *Journal of Magnetic Resonance.* 175(2):193-200. DOI:https://doi.org/10.1016/j.jmr.2005.04.005.

Sun, P.Z., Farrar, C.T. & Sorensen, A.G. 2007. Correction for artifacts induced by B0 and B1 field inhomogeneities in pH-sensitive chemical exchange saturation transfer (CEST) imaging. *Magnetic Resonance in Medicine.* 58(6):1207-1215. DOI:10.1002/mrm.21398.

Sun, P.Z., Zhou, J., Huang, J. & van Zijl, P. 2007. Simplified quantitative description of amide proton transfer (APT) imaging during acute ischemia. *Magn Reson Med.* 57(2):405-410. DOI:10.1002/mrm.21151.

Sun, P.Z., Lu, J., Wu, Y., Xiao, G. & Wu, R. 2013. Evaluation of the dependence of CEST-EPI measurement on repetition time, RF irradiation duty cycle and imaging flip angle for enhanced pH sensitivity. *Physics in medicine and biology.* 58(17):10.1088/0031-9155/1058/1017/N1229. DOI:10.1088/0031-9155/58/17/N229.

Sun, P.Z., Wang, E., Cheung, J.S., Zhang, X., Benner, T. & Sorensen, A.G. 2011. Simulation and optimization of pulsed radio frequency irradiation scheme for chemical exchange saturation transfer (CEST) MRI—demonstration of pH-weighted pulsed-amide proton CEST MRI in an animal model of acute cerebral ischemia. *Magnetic Resonance in Medicine.* 66(4):1042-1048. DOI:doi:10.1002/mrm.22894.

T-K. Truong, Chakeres, D.W. & Schmalbrock., P. Eds. 2004. Effects of B0 and B1 inhomogeneity in ultra-high field MRI. In Proc. I. 2170.

Tamhane, A.A. & Arfanakis, K. 2009. Motion Correction in PROPELLER and Turboprop-MRI. *Magnetic Resonance in Medicine.* 62(1):174-182. DOI:10.1002/mrm.22004.

Terreno, E., Castelli, D.D. & Aime, S. 2010. Encoding the frequency dependence in MRI contrast media: the emerging class of CEST agents. *Contrast Media Mol Imaging.* 5(2):78-98. DOI:10.1002/cmmi.369.

Thesen, S., Heid, O., Mueller, E. & Schad, L.R. 2000. Prospective acquisition correction for head motion with image-based tracking for real-time fMRI. *Magnetic Resonance in Medicine.* 44:457–465. DOI:10.1002/1522-2594(200009)44:3<457::AID-MRM17>3.0.CO;2-R.

Tisdall, M.D., Hess, A.T., Reuter, M., Meintjes, E.M., Fischl, B. & van der Kouwe, A.J.W. 2012. Volumetric Navigators (vNavs) for Prospective Motion Correction and Selective Reacquisition in Neuroanatomical MRI. *Magnetic Resonance in Medicine.* 68(2):389-399. DOI:10.1002/mrm.23228.

Todd, N., Josephs, O., Callaghan, M.F., Lutti, A. & Weiskopf, N. 2015. Prospective motion correction of 3D echo-planar imaging data for functional MRI using optical tracking. *NeuroImage.* 113:1-12. DOI:10.1016/j.neuroimage.2015.03.013.

Togao, O., Hiwatashi, A., Keupp, J., Yamashita, K., Kikuchi, K., Yoshiura, T., Suzuki, Y., Kruiskamp, M.J. et al. 2015. Scan-rescan reproducibility of parallel transmission based amide proton transfer imaging of brain tumors. *J Magn Reson Imaging.* 42(5):1346-1353. DOI:10.1002/jmri.24895.

Tomiyasu, M., Obata, T., Nishi, Y., Nakamoto, H., Nonaka, H., Takayama, Y., Autio, J., Ikehira, H. et al. 2010. Monitoring of liver glycogen synthesis in diabetic patients using carbon-13 MR spectroscopy. *European Journal of Radiology.* 73(2):300-304. DOI:https://doi.org/10.1016/j.ejrad.2008.10.019.

Tong, R. & Cox, R.W. 1999. Rotation of NMR images using the 2D chirp-z transform. *Magn Reson Med.* 41(2):253-256.

Truong, T.-K., Chen, B. & Song, A.W. 2008. Integrated SENSE DTI with Correction of Susceptibility- and Eddy Current-Induced Geometric Distortions. *NeuroImage.* 40(1):53-58. DOI:10.1016/j.neuroimage.2007.12.001.

Vaillant, G., Prieto, C., Kolbitsch, C., Penney, G. & Schaeffter, T. 2014. Retrospective Rigid Motion Correction in k-Space for Segmented Radial MRI. *IEEE Transactions on Medical Imaging.* 33(1):1-10. DOI:10.1109/TMI.2013.2268898.

Van de Walle, R., Lemahieu, I. & Achten, E. 1997. Magnetic resonance imaging and the reduction of motion artifacts: review of the principles. *Technol Health Care.* 5(6):419-435.

van der Kouwe, A.J.W., Benner, T. & Dale, A.M. 2006. Real-time rigid body motion correction and shimming using cloverleaf navigators. *Magnetic Resonance in Medicine.* 56(5):1019-1032. DOI:10.1002/mrm.21038.

Vinogradov, E., Sherry, A.D. & Lenkinski, R.E. 2013. CEST: from basic principles to applications, challenges and opportunities. *Journal of magnetic resonance (San Diego, Calif. : 1997).* 229:155-172. DOI:10.1016/j.jmr.2012.11.024.

Wachowicz, K., Tadic, T. & Fallone, B.G. 2012. Geometric distortion and shimming considerations in a rotating MR-linac design due to the influence of low-level external magnetic fields. *Med Phys.* 39(5):2659-2668. DOI:10.1118/1.3702591.

Wang, Z., Aguirre, G.K., Rao, H., Wang, J., Fernández-Seara, M.A., Childress, A.R. & Detre, J.A. 2008. Empirical optimization of ASL data analysis using an ASL data processing toolbox: ASLtbx. *Magnetic resonance imaging.* 26(2):261-269. DOI:10.1016/j.mri.2007.07.003.

Ward, H.A., Riederer, S.J. & Jack, C.R. 2002. Real-time autoshimming for echo planar timecourse imaging. *Magnetic Resonance in Medicine.* 48(5):771-780. DOI:10.1002/mrm.10259.

Ward, K.M., Aletras, A.H. & Balaban, R.S. 2000. A New Class of Contrast Agents for MRI Based on Proton Chemical Exchange Dependent Saturation Transfer (CEST). *Journal of Magnetic Resonance.* 143(1):79-87. DOI:https://doi.org/10.1006/jmre.1999.1956.

Webb P, M.A. 1991. Rapid, fully automatic, arbitrary-volume in vivo shimming. . *Magnetic Resonance in Medicine.* 20(1):113–122.

Wech, T. & Kostler, H. 2018. Robust motion correction in CEST imaging exploiting low-rank approximation of the z-spectrum. *Magnetic Resonance in Medicine.* 80(5):1979-1988. DOI:10.1002/mrm.27206.

Wei, W., Jia, G., Flanigan, D., Zhou, J. & Knopp, M.V. 2014. Chemical exchange saturation transfer MR imaging of articular cartilage glycosaminoglycans at 3 T: Accuracy of B0 Field Inhomogeneity corrections with gradient echo method. *Magnetic resonance imaging.* 32(1):41-47. DOI:10.1016/j.mri.2013.07.009.

Weis, J., Kullberg, J. & Ahlström, H. 2018. Multiple breath-hold proton spectroscopy of human liver at 3T: Relaxation times and concentrations of glycogen, choline, and lipids. *Journal of Magnetic Resonance Imaging.* 47(2):410-417. DOI:10.1002/jmri.25734.

Welch, E.B., Manduca, A., Grimm, R.C., Ward, H.A. & Jack Jr, C.R. 2002. Spherical navigator echoes for full 3D rigid body motion measurement in MRI. *Magnetic Resonance in Medicine.* 47(1):32-41. DOI:10.1002/mrm.10012.

Westbrook, C. 2016. *MRI at a glance.* 3rd edition. Oxford, England: Wiley-Blackwell.

Westbrook, C., Roth, C.K. & Talbot, J. 2011. *MRI in practice.* 4th edition. Oxford, England: Blackwell Science.

White, N., Roddey, C., Shankaranarayanan, A., Han, E., Rettmann, D., Santos, J., Kuperman, J. & Dale, A. 2010. PROMO – Real-time Prospective Motion Correction in MRI using Image-based Tracking. *Magnetic Resonance in Medicine.* 63(1):91-105. DOI:10.1002/mrm.22176.

Wilson JL, J.M., Jezzard P. . 2002. Optimization of static field homogeneity in human brain using diamagnetic passive shims. . *Magnetic Resonance in Medicine.* 48(5):906–914.

Windschuh, J., Zaiss, M., Ehses, P., Lee, J.S., Jerschow, A. & Regatte, R.R. 2018. Assessment of frequency drift on CEST MRI and dynamic correction: application to gagCEST at 7 T. *Magnetic Resonance in Medicine.* 00:1–10. DOI:10.1002/mrm.27367.

Windschuh, J., Zaiss, M., Meissner, J.E., Paech, D., Radbruch, A., Ladd, M.E. & Bachert, P. 2015. Correction of B1-inhomogeneities for relaxation-compensated CEST imaging at 7 T. *NMR Biomed.* 28(5):529-537. DOI:10.1002/nbm.3283.

Witney, T.H., Carroll, L., Alam, I.S., Chandrashekran, A., Nguyen, Q.-D., Sala, R., Harris, R., DeBerardinis, R.J. et al. 2014. A novel radiotracer to image glycogen metabolism in tumors by positron emission tomography. *Cancer research.* 74(5):1319-1328. DOI:10.1158/0008-5472.CAN-13-2768.

Woessner, D.E., Zhang, S., Merritt, M.E. & Sherry, A.D. 2005. Numerical solution of the Bloch equations provides insights into the optimum design of PARACEST agents for MRI. *Magnetic Resonance in Medicine.* 53(4):790-799. DOI:10.1002/mrm.20408.

Wolfsdorf, J.I. & Weinstein, D.A. 2003. Glycogen storage diseases. *Rev Endocr Metab Disord.* 4(1):95-102.

Wood, M.L. & Henkelman, R.M. 1985. MR image artifacts from periodic motion. *Med Phys.* 12(2):143-151. DOI:10.1118/1.595782.

Wu, B., Warnock, G., Zaiss, M., Lin, C., Chen, M., Zhou, Z., Mu, L., Nanz, D. et al. 2016. An overview of CEST MRI for non-MR physicists. *EJNMMI Physics.* 3(1):19. DOI:10.1186/s40658-016-0155-2.

Wu, W.C., Edlow, B.L., Elliot, M.A., Wang, J. & Detre, J.A. 2009. Physiological modulations in arterial spin labeling perfusion magnetic resonance imaging. *IEEE Trans Med Imaging.* 28(5):703-709. DOI:10.1109/tmi.2008.2012020.

Xu, J., Zaiss, M., Zu, Z., Li, H., Xie, J., Gochberg, D.F., Bachert, P. & Gore, J.C. 2014. On the origins of chemical exchange saturation transfer (CEST) contrast in tumors at 9.4T. *NMR in biomedicine.* 27(4):406-416. DOI:10.1002/nbm.3075.

Yeung, H.N. & Aisen, A.M. 1992. Magnetization transfer contrast with periodic pulsed saturation. *Radiology.* 183(1):209-214. DOI:10.1148/radiology.183.1.1549673.

Yuan, J., Zhou, J., Ahuja, A.T. & Wang, Y.X. 2012. MR chemical exchange imaging with spin-lock technique (CESL): a theoretical analysis of the Z-spectrum using a two-pool R(1rho) relaxation model beyond the fast-exchange limit. *Phys Med Biol.* 57(24):8185-8200. DOI:10.1088/0031-9155/57/24/8185.

Zaiss, M. & Bachert, P. 2013. Exchange-dependent relaxation in the rotating frame for slow and intermediate exchange – modeling off-resonant spin-lock and chemical exchange saturation transfer. *NMR in biomedicine.* 26(5):507-518. DOI:10.1002/nbm.2887.

Zaiss, M. & Bachert, P. 2013. Chemical exchange saturation transfer (CEST) and MR Z-spectroscopy in vivo: a review of theoretical approaches and methods. *Phys Med Biol.* 58(22):R221-269. DOI:10.1088/0031-9155/58/22/r221.

Zaiss, M., Schmitt, B. & Bachert, P. 2011. Quantitative separation of CEST effect from magnetization transfer and spillover effects by Lorentzian-line-fit analysis of z-spectra. *J Magn Reson.* 211(2):149-155. DOI:10.1016/j.jmr.2011.05.001.

Zaiss, M., Ehses, P. & Scheffler, K. 2018. Snapshot-CEST: Optimizing spiral-centric-reordered gradient echo acquisition for fast and robust 3D CEST MRI at 9.4 T. *NMR Biomed.* 31(4):e3879. DOI:10.1002/nbm.3879.

Zaiss, M., Xu, J., Goerke, S., Khan, I.S., Singer, R.J., Gore, J.C., Gochberg, D.F. & Bachert, P. 2014. Inverse Z-spectrum analysis for spillover-, MT-, and T1-corrected steady-state pulsed CEST-MRI – application to pH-weighted MRI of acute stroke. *NMR in biomedicine.* 27(3):240-252. DOI:doi:10.1002/nbm.3054.

Zaiss, M., Zu, Z., Xu, J., Schuenke, P., Gochberg, D.F., Gore, J.C., Ladd, M.E. & Bachert, P. 2015. A combined analytical solution for chemical exchange saturation transfer and semi-solid magnetization transfer. *NMR in biomedicine.* 28(2):217-230. DOI:10.1002/nbm.3237.

Zaitsev, M., Maclaren, J. & Herbst, M. 2015. Motion artifacts in MRI: A complex problem with many partial solutions. *Journal of Magnetic Resonance Imaging.* 42(4):887-901. DOI:doi:10.1002/jmri.24850.

Zaitsev, M., Dold, C., Sakas, G., Hennig, J. & Speck, O. 2006. Magnetic resonance imaging of freely moving objects: prospective real-time motion correction using an external optical motion tracking system. *NeuroImage.* 31(3):1038-1050. DOI:10.1016/j.neuroimage.2006.01.039.

Zhang, Y., Heo, H.Y., Lee, D.H., Jiang, S., Zhao, X., Bottomley, P.A. & Zhou, J. 2017. Chemical exchange saturation transfer (CEST) imaging with fast variably-accelerated sensitivity encoding (vSENSE). *Magn Reson Med.* 77(6):2225-2238. DOI:10.1002/mrm.26307.

Zhang, Y., Taub, E., Salibi, N., Uswatte, G., Maudsley, A.A., Sheriff, S., Womble, B., Mark, V.W. et al. 2018. Comparison of reproducibility of single voxel spectroscopy and whole-brain magnetic resonance spectroscopy imaging at 3T. *NMR Biomed.* 31(4):e3898. DOI:10.1002/nbm.3898.

Zhe Sun, P., Benner, T., Kumar, A. & Sorensen, A.G. 2008. An Investigation of Optimizing and Translating pH-Sensitive Pulsed-Chemical Exchange Saturation Transfer (CEST) Imaging to a 3 T Clinical Scanner. *Magnetic Resonance in Medicine.* 60(4):834-841. DOI:10.1002/mrm.21714.

Zhou, I.Y., Wang, E., Cheung, J.S., Zhang, X., Fulci, G. & Sun, P.Z. 2017. Quantitative chemical exchange saturation transfer (CEST) MRI of glioma using Image Downsampling Expedited Adaptive Least-squares (IDEAL) fitting. *Scientific reports.* 7(1):84. DOI:10.1038/s41598-017-00167-y.

Zhou, J. & Zijl, P.C.M.v. 2006. Chemical exchange saturation transfer imaging and spectroscopy. *Progress in Nuclear Magnetic Resonance Spectroscopy.* 48(2):109-136. DOI:https://doi.org/10.1016/j.pnmrs.2006.01.001.

Zhou, J., Lal, B., Wilson, D.A., Laterra, J. & van Zijl, P.C.M. 2003. Amide proton transfer (APT) contrast for imaging of brain tumors. *Magnetic Resonance in Medicine.* 50(6):1120-1126. DOI:10.1002/mrm.10651.

Zhou, J., Payen, J.F., Wilson, D.A., Traystman, R.J. & van Zijl, P.C. 2003. Using the amide proton signals of intracellular proteins and peptides to detect pH effects in MRI. *Nature medicine.* 9(8):1085-1090. DOI:10.1038/nm907.

Zhou, J., Wilson, D.A., Sun, P.Z., Klaus, J.A. & van Zijl, P.C.M. 2004. Quantitative description of proton exchange processes between water and endogenous and exogenous agents for WEX, CEST, and APT experiments. *Magnetic Resonance in Medicine.* 51(5):945-952. DOI:10.1002/mrm.20048.

Zhou, J., Blakeley, J.O., Hua, J., Kim, M., Laterra, J., Pomper, M.G. & van Zijl, P.C. 2008. Practical data acquisition method for human brain tumor amide proton transfer (APT) imaging. *Magnetic Resonance in Medicine.* 60(4):842-849. DOI:10.1002/mrm.21712.

Zhou, Z., Bi, X. & Li, D. Eds. 2017. Cardiac CEST MRI with Dual-Echo Readout for B0 Correction: A Preliminary Reproducibility Study for Assessment of Metabolic Activity in the Heart. Honolulu, HI, USA: ISMRM.

Zijl, P.C.M.v., Zhou, J., Mori, N., Payen, J.F., Wilson, D. & Mori, S. 2003. Mechanism of magnetization transfer during on-resonance water saturation. A new approach to detect mobile proteins, peptides, and lipids. *Magnetic Resonance in Medicine.* 49(3):440-449. DOI:doi:10.1002/mrm.10398.

Zijl., v. & Yadav, N.N. 2011. Chemical Exchange Saturation Transfer (CEST): what is in a name and what isn't? *Magnetic Resonance in Medicine.* 65(4):927-948. DOI:10.1002/mrm.22761.

Zijl., v., Jones, C.K., Ren, J., Malloy, C.R. & Sherry, A.D. 2007. MRI detection of glycogen in vivo by using chemical exchange saturation transfer imaging (glycoCEST). *Proceedings of the National Academy of Sciences of the United States of America.* 104(11):4359-4364. DOI:10.1073/pnas.0700281104.

Zijl., v., Lam, W.W., Xu, J., Knutsson, L. & Stanisz, G.J. 2018. Magnetization Transfer Contrast and Chemical Exchange Saturation Transfer MRI. Features and analysis of the field-dependent saturation spectrum. *NeuroImage.* 168:222-241. DOI:10.1016/j.neuroimage.2017.04.045.

Zioga, M., Mikeli, M., Rapsomanikis, A.N. & Stiliaris, E. Eds. 2012. A real time motion correction technique for a small-field gamma-camera system. November 2012. IEEE Nuclear Science Symposium and Medical Imaging Conference Record (NSS/MIC). 2526-2528.

Zu, Z., Li, K., Janve, V.A., Does, M.D. & Gochberg, D.F. 2011. Optimizing Pulsed-Chemical Exchange Saturation Transfer (CEST) Imaging Sequences. *Magnetic Resonance in Medicine.* 66(4):1100-1108. DOI:10.1002/mrm.22884.